Performance analysis of future communications systems under residual hardware impairments

Leila Tlebaldiyeva

A thesis outline submitted in partial fulfillment of the requirement of Nazarbayev University for the degree of Doctor of Philosophy

April, 2020

Signed:

Dated:

Abstract

Cognitive radio (CR) and millimeter wave (mmWave) communication are two potential technologies for future wireless communication systems to meet ever-increasing consumer data demand. The significant advantage of CR is its ability to improve spectrum utilization by introducing spectrum management paradigms between primary and cognitive users. An even more significant enabling technology for future communications is mmWave communication that offers enormous bandwidth at mmWave frequency bands.

Low-grade transceiver hardware is often utilized in modern communication systems to lower the cost of potential networks. The residual hardware distortion noise originating from high rate and low-grade transceiver hardware is a vital parameter to consider while designing reliable systems. This dissertation work pursues to model residual transceiver hardware impairments by using the statistical additive Gaussian model, which is mathematically tractable and can be embedded in complex system configurations.

In this thesis, we first develop a system model for a dual-hop decode-and-forward underlay CR relay network operating under residual hardware impairments and derive a closed-form expression for the outage probability performance. Moreover, this work provides useful discussions on the design aspects of wireless communication systems in terms of the outage probability given residual transceiver noise level and fading parameters of channel.

Secondly, we study the spectrum sensing technique by employing an improved energy detector (ED) under residual hardware constraints. We present a novel test statistic for improved ED that accounts for residual distortion noise when the fading statistics of the received signal follows the $\alpha - \mu$ distribution. Moreover, we derive closed-form expressions for the *probabilities of detection and false alarm* and the *area under the receiver operating characteristic curve (AUC)* for additive white Gaussian and Nakagami-m fading channels. Our work proposes a new diversity concept of p*-order-law combining* and p*-order-law selecting* schemes to combat the adverse effect of residual hardware impairments.

Thirdly, our study develops an analytical framework for analog beamforming device-to-device mmWave communication constrained by residual hardware impairments and other random impairments such as multi-user interference, inter-beam radio frequency (RF) power leakage, and imperfect channel state information (CSI). We perform in-depth outage probability and ergodic capacity analysis for the proposed system model.

Finally, we propose to implement a maximum sub-array transmission (MST) scheme built on a hybrid beamforming structure that enables multi-user communication and high outage probability and ergodic capacity performance. The MST diversity suffers from RF power leakage and transceiver distortion noise that are addressed in this work.

The hardware impaired communication systems transmit at considerably lower rates than the ideal ones, and, therefore, our research emphasizes the importance of residual distortion modeling.

Acknowledgments

During my Ph.D. program, I had this rare opportunity working with three well-established researchers in the field of wireless communications. I feel enormously fortunate and proud for being supervised by Professor Corbett ROWELL, Professor Theodoros A. TSIFTSIS, and Professor Behrouz MAHAM. During the first year of the Ph.D. program, Professor Corbett ROWELL taught us the most interesting courses in advanced communications that enlightened me and increased my knowledge in the area of wireless communications. I want to thank Professor Corbett ROWELL for sharing his unique experience working in the telecom industry and designing RF circuits.

Starting from March 2016 I began working with Professor Theodoros A. TSIFTSIS. He proposed the main title of the dissertation work and helped me to acquire important research skills and methods. Besides, I was closely working with Professor Theodoros A. TSIFTSIS until completion of my Ph.D. program through videoconferencing and email communication. Beginning from March 2018, I started working with Professor Behrouz MAHAM, who has broadened and enriched my research area to the millimeter wave communications, which is a popular research direction today. Additionally, I still communicate with I want to express my greatest gratitude to Professor Theodoros A. TSIFTSIS and Professor Behrouz MAHAM for dedicating their mentorship, delightful collegiality, and sharing valuable knowledge and time during my Ph.D. studies.

Besides, I would like to thank my co-supervisor, Professor Refik Caglar KIZILIRMAK for his valuable comments and professional advice.

Besides my supervisors, I would like to distinguish and thank Professor Luis R. Rojas-SOLÓRZANO for his positive attitude, trust, and genius support during my Ph.D. journey.

My highest appreciation goes to my family members for their patience, love, and prayers. Mainly, I would like to thank our grandmother - Bakhyt, for her sincere dedication to taking care of her two young grandchildren (my children) Alimzhan and Rayana.

Finally, my thanks go to all my friends and colleagues who have supported me to complete this research work.

Leila TLEBALDIYEVA

Preface

Leila TLEBALDIYEVA received the B.Sc. (with Distinction) degree in Communications Engineering from Carleton University, Ottawa, Canada, in June 2010. She got M.Sc. (with Merit) degree in Wireless and Optical Communications Engineering from University College London in September 2012. From August 2010 to March 2011, she worked as a broadcast liaison manager in IT and TV broadcast department of Organizing Committee for the 7th Winter Asian Games in Astana-Almaty, and then as a laboratory assistant at Nazarbayev University from April 2011 to September 2011. Then after pursuing an MSc degree, she continued working as a laboratory assistant from October 2012 to Jan 2015. Then, from May 2012 till January 2017, she worked as a teacher assistant at Nazarbayev University. Since January 2015, she started a Ph.D. degree in Science, Engineering, and Technology with the research topic on Performance analysis of future communications systems under residual hardware impairments at the School of Engineering and Digital Sciences, Nazarbayev University.

Contents

List of Figures

List of Tables

List of Abbreviations

1G	first generation
2G	second generation
3G	third generation
3GPP	third generation partnership project
4G	fourth generation
5G	fifth generation
ACI	adjacent channel interference
ADC	analog-to-digital converter
AUC	area under the receiver operating characteristic curve
AWGN	additive white Gaussian noise
BPSK	binary phase shift keying
CDF	cumulative distribution function
CR	cognitive radio
CSI	channel state information
CU	cognitive user
DAC	digital-to-analog converter
DARPA	Defence Advanced Research Projects Agency
dB	decibel
DF	decode-and-forward
D2D	device-to-device
ED	energy detector
EVM	error vector magnitude
I/Q	in-phase (I) and quadrature (Q)

I.I.D. (i.i.d.)	independent and identically distributed
I.N.I.D. (i.n.i.d.)	independent and not identically distributed
LOS	line-of-sight
LTE	long term evolution
MST	maximum sub-array transmission
MIMO	multiple-input multiple-output
MmWave	millimeter wave
NLOS	non line-of-sight
OFDM	orthogonal frequency-division multiplexing
OSA	opportunistic spectrum access
PDF	probability density function
PU	primary user
QAM	quadrature amplitude modulation
QPSK	quadrature phase-shift keying
RF	radio frequency
ROC	receiver operating characteristic
RV	random variable
SNDR	signal-to-noise-distortion ratio
SNDIR	signal-to-noise-distortion-interference ratio
SRDNR	signal-to-RF leakage-distortion-noise ratio
SNR	signal-to-noise ratio
SU	secondary user
UE	user equipment
UHF	ultra-high frequency

List of Symbols

$\mathcal{CN}(a, b)$	complex normal distribution with a mean and b variance
$f_X(x)$	probability density function of random variable X
$F_X(x)$	cumulative distribution function of random variable X
$\Gamma(\cdot)$	Gamma function
$\Gamma(a, b)$	upper incomplete Gamma function
$\gamma(a, b)$	lower incomplete Gamma function
$\mathbb{E}(\cdot)$	statistical expectation operator
κ	EVM level
λ	wavelength
N_0	noise power at the receive node
γ_{th}	predefined SNR threshold
$\mathbf{x}$	lower bold case denotes vector
$\|x\|$	absolute value of x
$\|\mathbf{x}\|$	Euclidean norm of $\mathbf{x}$
γ	nominal transmit SNR
D	secondary destination
$\Pr(A)$	probability of the event A
$P_{out}(\cdot)$	outage probability
P	average signal power
PR	primary receiver
S	secondary source
R	secondary relay

Chapter 1

Introduction

"Wireless is coming to mankind... Some day there will be, say, six great wireless telephone stations in a world system connecting all the inhabitants on this earth to one another, not only by voice but by sight" said Nicola Tesla [1] back in 1905 by predicting mainstream wireless communication that empowers both voice and video communication. Tesla's prediction came true in the twenty first century and Fig. 1.1 from [2] and Fig. 1.2 from [3] demonstrate the scale of modern communication. In Fig. 1.1, the forecast of active mobile users between 2017 to 2022 is presented by Cisco Systems. The number of global mobile users has enormously emerged over the last decade. Based on Fig. 1.2, we see that global mobile data traffic annually increases by around average to 50% from 2017 to 2022. Alternatively, monthly data demand will increment 6.73 times over 5 years [4]. A high market demand for wide bandwidth as well as competition for a high revenue among mobile vendors and technological development of semiconductor technology accelerated development of wireless communication networks from 1G with 2 kb/s data rate in 1980 to 5G with 1 Gb/s data rate in 2020. In this work, we investigate the practical future wireless communications systems that aim to meet consumer requirements.

1.1 Problem statement

Ever-increasing data demand and bandwidth limitation in the ultra-high frequency (UHF) range create a performance bottleneck in modern communication systems. Spectrum

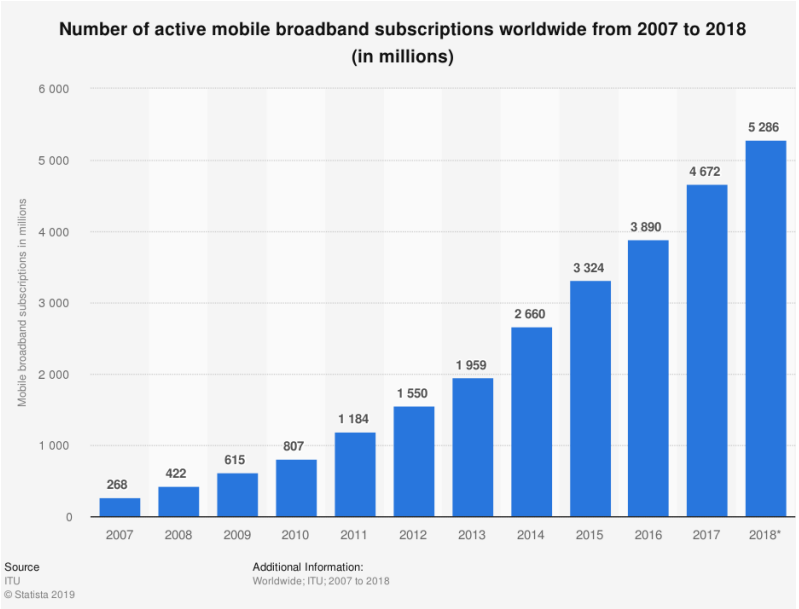

Figure 1.1. Worldwide mobile subscribers (in millions) in 2007 – 2018 years.

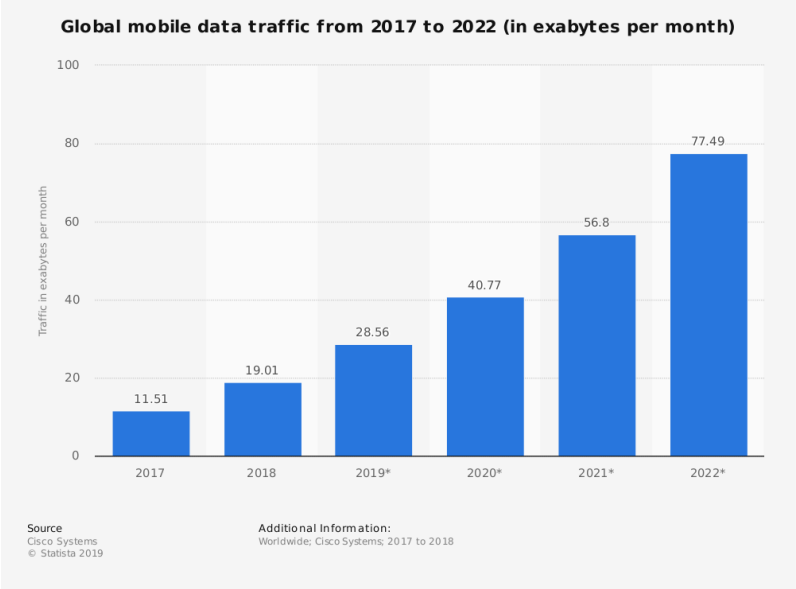

Figure 1.2. Global mobile data traffic (exabytes per month) in 2017 – 2022 years.

sensing/sharing techniques and millimeter wave (mmWave) communication with massive multiple-input multiple-out (MIMO) antennas are two popular, promising technologies to meet high bandwidth demand. On the one hand, cognitive radio (CR) technology [5], [6] solves the spectrum scarcity problem by managing spectrum sharing between primary and

secondary users. On the other hand, mmWave frequencies along with massive MIMO antenna systems [7], [8] began a new era in wireless communications, called 5G and beyond, that aims to resolve the technological limitation of the UHF range and explore enormous bandwidth between $3 - 300$ GHz. Practical transceivers used in high rate systems are not ideal and add residual distortion noise to the system [9]. The impact of distortion noise is even more profound in mmWave systems due to complications in high frequencies [10]. Other performance degradation factors in wireless communication are interference and RF power leakage [11], [12] from neighboring user equipment (UE) nodes.

1.2 Motivation

Residual transceiver distortion noise always exists in wireless communications systems; however, it is often ignored in the analysis of modern communication systems. In this work, we aim to fill this gap by studying recently introduced technologies for 5G, such as cognitive spectrum sensing/sharing networks and mmWave communication technologies under transceiver distortion noise constraints. The advantage of residual distortion noise modelling is the ability to design more reliable modern communication systems. This work suggests using comprehensive transceiver distortion noise modelling that also facilitates analysis of other system constraints such as interference, RF power leakage, and imperfect CSI.

1.2.1 Key contributions

This section demonstrates the key findings of dissertation work:

- Decode-and-forward (DF) dual-hop cognitive relay system under the presence of transceiver hardware impairments and interference temperature constraint is presented in this chapter, and the performance of the system is evaluated by deriving a closed-form expression for an outage probability. Nakagami-m fading channels are considered for all primary and cognitive links. Besides, this chapter discusses the design aspects of achieving a certain outage probability based on fading parameters

of the channel and hardware impairment level, which is inversely proportional to the transmission rate. Calculation results reveal that by measuring fading parameters of the channel, one could choose the proper threshold to meet the desired outage probability.

- Moreover, we investigate a non-blind spectrum sensing by utilizing an improved ED under the presence of transceiver distortion noise over Nakagami-m fading channel. We propose a novel method of evaluating the improved ED statistics for N signal samples with $\alpha - \mu$ distribution. We present closed-form analytical formulas to find probabilities of detection and false alarm of the improved ED over additive white Gaussian noise (AWGN) channel. We extend our analysis to evaluate closed-form formulas for the average detection probability over fading channels. Also, the asymptotic analysis of the improved ED is studied over the fading channel when the average Signal-to-Noise Ratio (SNR) approaches to zero. The AUC analysis evaluates the quality of the detector over AWGN channel. Our numerical results show the detrimental effect of distortion noise. Therefore, we propose to apply diversity techniques such as p-order law combining and p-order law selecting to enhance the improved ED accuracy.

- Furthermore, we study device-to-device (D2D) communication for a finite number of D2D users overlaying the mmWave network by considering residual transceiver distortion noise and interference from N device nodes. Simultaneous spectrum and time sharing among D2D pairs create interference that degrades the performance of a wireless system. We formulate signal-to-distortion-interference-noise-ratio and evaluate its probability density function (PDF) and cumulative density function (CDF). Besides, closed-form expressions are derived for the outage probability and ergodic capacity performance metrics, including lower/upper ergodic capacity bounds for the mmWave network co-existed by D2D nodes.

- A hybrid beamforming based mmWave network is developed where a base station simultaneously communicates with multiple UEs. We consider that the proposed

system model is impaired by RF power leakage from neighboring UEs as well as hardware residual distortion noise. To mitigate RF power leakage and distortion noise a MST diversity technique is implemented based on hybrid beamforming structure. Multiple and independent beams from the base station are combined by using MST diversity technique at a receiver UE. The performance of the mmWave system is evaluated through outage probability and ergodic capacity analysis.

1.2.2 List of Publications

The results of this dissertation work have yielded the following journal and conference publications.

Published journal papers

- L. Tlebaldiyeva, T. A. Tsiftsis and B. Maham, "Performance Analysis of Improved Energy Detector With Hardware Impairments for Accurate Spectrum Sensing," in IEEE Access, vol. 7, pp. 13927-13938, 2019.
- L. Tlebaldiyeva, B. Maham, and T. A. Tsiftsis, "Device-to-Device mmWave Communication in the Presence of Interference and Hardware Distortion Noises" in IEEE Communications Letters, 17 June 2019.
- L. Tlebaldiyeva, B. Maham and T. A. Tsiftsis, "Capacity Analysis of Device-to-Device mmWave Networks under Transceiver Distortion Noise and Imperfect CSI," in IEEE Transactions on Vehicular Technology.

Published conference papers

- L. Tlebaldiyeva and T.A. Tsiftsis, "Underlay Cognitive Radio with Imperfect Transceiver Electronics under Nakagami-m Fading," 2018 International Conference on Computing and Network Communications (CoCoNet), Astana, 2018, pp. 58-63. IEEE best paper award.

- L. Tlebaldiyeva, T. A. Tsiftsis and B. Maham, "Spectrum Sensing using Improved Energy Detector under Transceiver Hardware Impairments," 2018 IEEE International Symposium on Dynamic Spectrum Access Networks (DySPAN), Seoul, 2018, pp. 1-5.

- L. Tlebaldiyeva, B. Maham, O. Tirkkonen, "Maximum Sub-array Transmission Diversity for mmWave Network under RF Power Leakage and Distortion Noises", 2020 IEEE WCNC, Seoul. Accepted.

1.2.3 Thesis Outline

This dissertation work is sub-categorized into three parts. The first part consists of Chapter 1, 2. Chapter 1 introduces the subject of the dissertation work, including a problem statement, the motivation of the research, and presents key contributions with the list of publications. Chapter 2 discusses background information about CR technology, massive MIMO mmWave communication as well as the major sources of transceiver hardware impairments. Moreover, this chapter introduces a residual transceiver distortion noise model studied in this work.

The second part of the thesis consists of Chapters 3 and 4, where research findings on the cognitive relay network and improved ED for spectrum sensing are studied under the presence of transceiver distortion noise.

The third part of the thesis is comprised of Chapter 5 and Chapter 6 that focuses on issues in D2D assisted mmWave communication and multi-user mmWave communication considering interference modelling, imperfect CSI, and inter-beam RF power leakage from nearby nodes as well as transceiver distortion noise. A maximum sub-array transmission diversity technique is proposed to mitigate the imperfections mentioned above.

Chapter 2

Literature Review

2.1 Future Communication Systems

2.1.1 Cognitive Radio Technology

The RF spectrum is a scarce resource owned and arbitrated by government agencies of each state, e.g., Federal Communications Commission in the US and the Committee of Communications, Informatization, and Information in Kazakhstan. Voracious demand on the RF spectrum leads to a looming scarcity of RF spectrum in cm wave range around the globe. For instance, the number of active mobile subscribers has increased from 268 million in 2007 year to 5286 million in 2018 year [3], which means that mobile subscriptions have incremented nearly 20 times in 11 years. Besides, 1 trillion wireless devices are expected by 2020 [13] from cell phones to wearable devices in the civilian sector and underwater sensors to satellites in the military sector. Traditionally, the RF spectrum is sub-divided between licensed users over a large geographical region. Although exclusive spectrum usage guarantees interference-free communication, the spectrum below 3 GHz is not fully utilized between $15 - 85$ % of the time in practice [13]. The US Defence Advanced Research Projects Agency (DARPA) perceived the significance of CR systems in military and personnel applications and organized the DARPA Spectrum Collaboration Challenge that was held in October 2019 to bring new ideas and experiments on stage from academia and industry.

CR is an intelligent system that facilitates the detection of primary and secondary

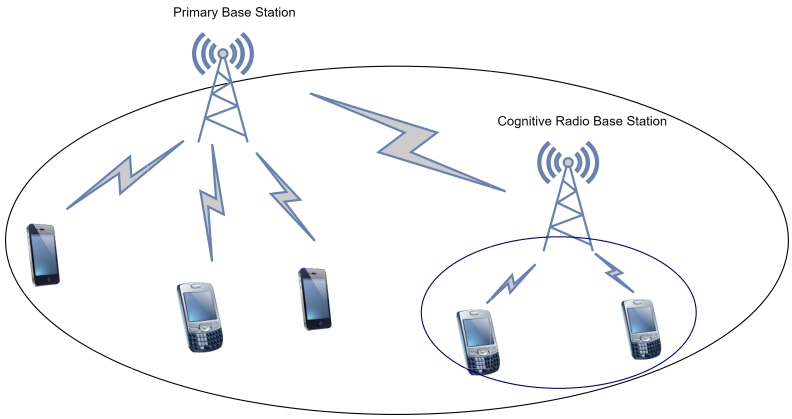

Figure 2.1. Cognitive radio network scheme.

users and arbitrates unused bandwidth between them by adjusting bandwidth, modulation type, as well as frequency based on transmission and reception. Fig. 2.1 illustrates the basic concept of a CR system: a primary base station network owns the frequency, and a secondary user (SU) is granted access based on the chosen CR paradigm that will be further discussed in this section. CR spectrum management concepts work despite the type of network generation (e.g., 2G, 3G, 4G, and 5G and beyond). CR spectrum management is either called Dynamic Spectrum Access, Flexible Spectrum Use, or Opportunistic Spectrum Access (OSA). Spectrum awareness, analysis and decision, and spectrum exploitation are three main cycles in spectrum sensing [14]. Spectrum sensing uses time, frequency, space, and polarization domains to check the bandwidth occupancy. The OSA poses some challenges to the transceiver since it must sense the spectrum over the wide range and give a quick decision response [15]. According to [13], each cognitive user (CU) possesses the following functionalities: spectrum sensing, spectrum decision, spectrum sharing, and spectrum mobility.

2.1.2 Cognitive Radio Paradigms

Three major spectrum sharing paradigms that describe the interaction between primary and secondary users such as underlay, overlay, and interweave are shown in Fig. 2.3 and summarized as well.

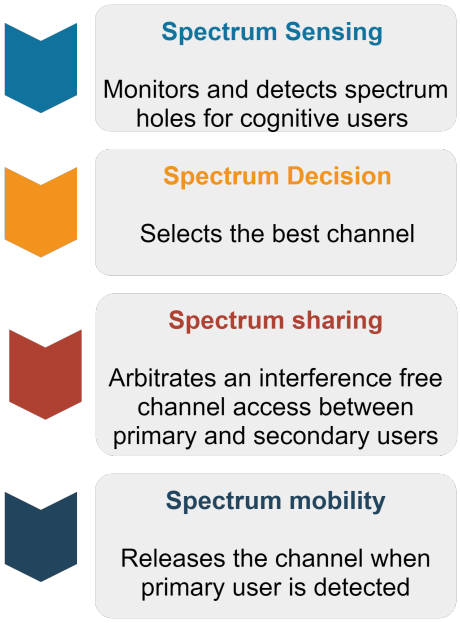

Figure 2.2. Major cognitive user functionalities.

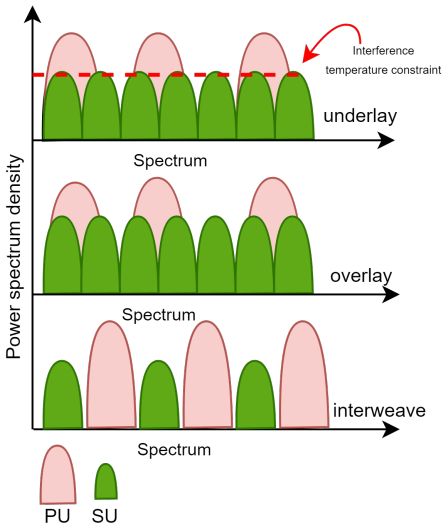

Figure 2.3. Overview of CR paradigms: underlay, overlay, and interweave.

- Underlay paradigm

  Cognitive transmitter is aware about its interference to the PU. Cognitive transmitters can concurrently transmit data along with PUs as long as the interference level from CUs is under a certain threshold. Therefore, the power of the cognitive transmitter is limited to interference temperature constraint (harmful interference), which is approximated by the channel sounding or cooperative sensing.

- Overlay paradigm

  CUs are aware of PUs essential information such as channel gain and encoding information. This paradigm allows transmission to both cognitive and primary users simultaneously. However, CU's power is relayed to the PU's data to offset the interference. Therefore, CUs do not have a limit on transmit power level. The disadvantage of this paradigm is that encoding and decoding processes are more complex in comparison to the other two paradigms.

- Interweave paradigm

  CUs sense the environment on the absence of PUs in space, time, and frequency. Simultaneous data transmission occurs only during the misdetection of a PU. The CU transmit power is limited to the radius of PU activity.

2.2 MmWave Communication with Massive MIMO Antennas

MmWave wavelength massive MIMO antennas are promising technologies for high spectrum utilization and energy efficiency for future mobile networks [7], [8]. Commercial 5G networks operating on mmWave frequency and employing massive MIMO antennas are already being implemented in the World. Fig. 2.4 presents 5G coverage map with commercial, limited, and pre-release 5G networks. China demonstrated the first remote robotic surgery on an animal in January 2019, where Huawei's 5G network technology was used for control and video links at both ends [16].

Accommodation of a large number of antennas and RF blocks is a challenge for base stations and handsets in the conventional RF range. Inter element antenna spacing should be at least $\lambda/2$ apart from each other, where λ is antenna wavelength. MmWave antennas have small physical size, therefore, it is possible to decrease the spacing between antenna elements and install up to 64 to 512 antennas at a base station [17] and up to 32 MIMO antennas at UE nodes. A large number of antennas create more degree of

freedom, which results in increased data rate and reduced outage probability. Another advantage of massive MIMO technology is spectrum reuse due to high free space loss and high attenuation [18]. The authors in [19] summarized the challenges of massive MIMO as hardware impairments of low-cost components, performance measurement, the physical size of massive MIMO antennas, pilot contamination, internal power consumption, channel characterization, fast digital signal processing hardware, propagation models and deployment of the mmWave standard. Multi-user massive MIMO network deployment targets low cost and power-efficient hardware implementation at base station [20]; both of these factors are a significant concern for network providers. Large scale antennas for multi-user communication require fast digital processing hardware operating in real-time. Signal processing algorithms should be linear or nearly linear. According to [19], massive MIMO antennas could be modeled by the law of large numbers, meaning that noise, interference, and fading is averaged out. Array antennas of an order of 100s require inexpensive components such as direct conversion radio receivers. Bjornson et al. suggested that transceiver distortion noise limits the channel estimation accuracy and channel capacity of massive MIMO systems [21].

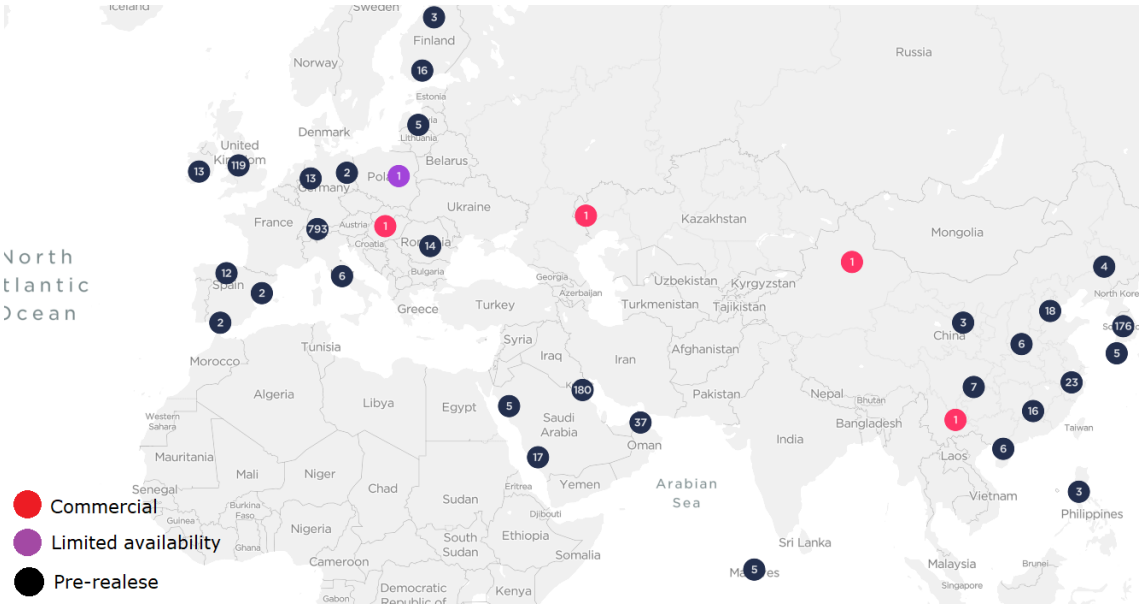

Figure 2.4. 5G deployment map in the World.

2.3 Transceiver Hardware Impairments

2.3.1 Sources of transceiver hardware impairments

Modern communication systems require low power, inexpensive, and high data rate transceivers. As was discussed in the previous subsection, low-grade transceiver equipment is often used for massive MIMO systems. For instance, direct-conversion radio receivers are frequently considered in the technical literature for spectrum sensing/sharing [22–24] due to low power consumption and ease of circuit integration. A typical direct conversion radio receiver architecture is shown in Fig. 2.5 presented in [9]. At the transmitter side, a modulated digital signal from the digital baseband part passes through digital-to-analog-converter (DAC), then it up-converts to RF and gets amplified. External intermediate frequency filters and image rejection filters are not required for direct conversion radio receivers as it is required for superheterodyne receivers. Although most of the digital processing is performed at the digital side, RF front-end requires careful consideration [9]. Analog front-end contains power amplifiers, converters, filters, mixers, oscillators, and each of those components adds imperfections to the system.

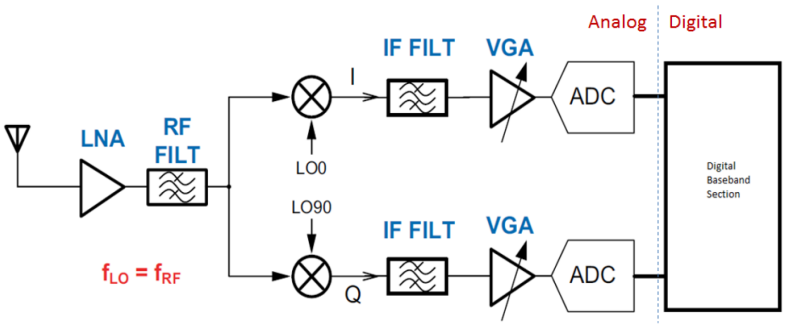

Figure 2.5. A typical direct conversion radio receiver architecture.

2.3.1.1 Power Amplifier Non-Linearity

A power amplifier is a main component of the transceiver that accounts for most of the power consumption and cost of the entire RF circuit. For example, power amplifiers at

base station terminals use around $50 - 80\%$ of total power [25]. When power amplifier operates at a saturation region, nonlinear effects of power amplifier increases and creates nonlinear interference, these nonlinear distortions vary based on bandwidth and operating frequency [26]. Adjacent channel interference (ACI) is a result of spectral regrowth of power amplifier output at nonlinear operation region [27]. Power allocation in CR networks in the presence of nonlinear effects of a power amplifier is investigated in [14]. Secondary receiver average SNR is studied under the peak, and average ACI, closed-form equations for the power allocation are derived under peak and average ACI constraints. The theoretical and simulation results of this work show that the average ACI demonstrates better performance rather than peak ACI. The authors in [14] presents a sub-optimal power allocation method. This method uses a bisection search method for nonlinear power amplifiers based on the orthogonal frequency-division multiplexing (OFDM) CR network. Linear and nonlinear power amplifiers are simulated and compared in [14]. As a result, it was proven that energy efficiency is severely degraded while using a nonlinear power amplifier. Contemporary linearization methods including digital post/pre-distortion, feed-forward, and feedback are used now to mitigate the effect of nonlinearity. Digital pre-distortion technique fixes the nonlinear signal before transmission. Feedback path that contains analog-to-digital converters (ADCs) and mixers is required after power amplifier. The feedback path delivers an analysis of the signal image to eliminate non-linearities. The disadvantage of this method is the consumption of additional power [25]. The digital post-distortion method compensates amplifier non-linearities at the baseband side of the receiver. This way, no feedback path is required at the transmitter, which reduces digital signal processing calculations at the cognitive transmitter side.

2.3.1.2 I/Q imbalance

Direct conversion radio receivers do not require image rejection filters and external intermediate frequency. Alternatively, image rejection is done in by in-phase (I) and quadrature (Q) arms [9]. I/Q imbalance of direct conversion radio receivers degrade the spectrum sensing capability. Single-channel and multi-channel direct-conversion receivers with I/Q

imbalance are studied in [25]. Closed-form expressions for the probability of detection and false alarm are evaluated, and following conclusions are drawn: 1) Single channel receivers are tolerant to I/Q imbalance, however, multiple-channel receivers are susceptible to I/Q imbalance; 2) false alarm probability significantly increases when non-ideal receivers with I/Q imbalance are used. The authors in [25] proposed a waveform level interference cancellation method for compensation of I/Q imbalance effect. It was done by clearing the primary channel signal from the image channel signal.

2.3.1.3 ADC/DAC Quantization Noise

The ADC/DACs transform the analog RF signal into the digital domain by quantizing continuous analog signal into its discrete domain. Quantization error and clipping errors are the two main sources of quantization noise [14]. For OFDM waveform clipping error is more problematic, since it may pose a difficulty in detecting low SNR PU signal. Practical next generation networks apply low-grade components, including low cost ADCs/DACs with a low resolution level. Simulation results from [28] claimed that the system works correctly with a quantization level of 2 and 3 bits at 1 decibel (dB) SNR loss. According to [14], glitch energy is a major source of non-linearity for high-performance ADC/DAC.

2.3.1.4 Phase Noise

Phase noise is the frequency deviation in a local oscillator that brings sudden changes in local oscillator frequency and timing. Therefore, phase noise is considered as a major limitation in communication systems. More about phase noise measurement and estimation are given in [29–31]. Oscillator phase noise in direct-conversion radio receivers creates crosstalk while multi-channel energy detection [23].

2.3.2 Gaussian Model for Aggregate Residual Transceiver Impairments

Practical transceivers are not ideal and add inevitable distortion noise to the system, as was described in Section 2.3.1. Calibration and pre-distortion techniques are applied at the transmitter side, and complex algorithms are used at the receiver side to mitigate hardware impairment noise [9]. However, in practice, it is not possible to filter out all transceiver imperfections, and residual distortion noise remains in the system. The main reasons for distortion noise are a deviation in parameter estimation, a mismatch between a practical transceiver and compensated model, as well as complex implementation of compensation algorithm [32].

The sources of aggregate residual distortion noise that we consider in this dissertation work originate from I/Q imbalance, phase noise, and non-linear amplifier discussed in Section 2.3.2. The aggregate residual distortion noise is distributed as a circular symmetric complex Gaussian variate, which is proportional to average signal power multiplied to an error vector magnitude (EVM) parameter that is discussed in Section 2.3.2.1. According to theoretical and measurement results, [32–36] statistical Gaussian model provides an accurate approximation of aggregate residual impairments. Besides, the Gaussian model is mathematically tractable while incorporating residual distortion noise into more complex system analysis. According to [21], hardware impairments at UE mainly limit capacity as the number of antennas increases at UE, whereas impairments diminish asymptotically at massive MIMO base stations. Also, it was analytically proved that hardware impairment creates uplink and downlink capacity ceiling regardless of SNR and the number of antennas.

Let us consider a simple point-to-point system that is constrained by a transmitter and receiver residual distortion noise. A complex signal s with an average signal power $P = \mathbb{E}\{|s|^2\}$ is transmitted through complex fading channel h and additive white Gaussian noise n is added to the signal. The received signal y with residual transmit Tx/Rx

impairments could be expressed as

$$y = h(s + \nu_t) + \nu_r + n, \tag{2.1}$$

where ν_t and ν_r are corresponding transmit and receive residual impairments modeled as $\nu_t \sim \mathcal{CN}(0, \kappa_t^2 P)$ and $\nu_r \sim \mathcal{CN}(0, \kappa_r^2 Ph)$. The EVM parameters $\kappa_t > 0$ and $\kappa_r > 0$ determines the level of distortion noise, alternatively $\kappa_t = 0$ and $\kappa_r = 0$ is for ideal system model. Similar to [21], we could express the general expression for the joint Tx/Rx residual impairments as

$$\mathbb{E}_{\nu_t,\nu_r}\{|h\nu_t + \nu_r|^2\} = P|h|^2(\kappa_t^2 + \kappa_r^2) = P|h|^2(\kappa_t^2 + \kappa_r^2) = P|h|^2\kappa^2, \tag{2.2}$$

where $\kappa = \sqrt{\kappa_t^2 + \kappa_r^2}$. Numerical value of κ is a protocol specific number.

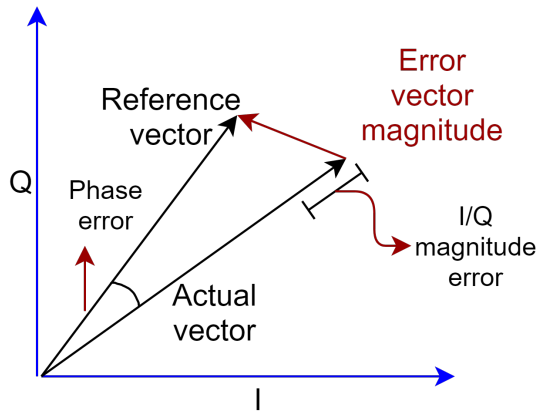

Figure 2.6. Representation of the EVM vector.

2.3.2.1 Error Vector Magnitude

The EVM is a Figure of Merit that measures the physical transceiver quality and modulation performance. The general schematic that represents the EVM is shown in Fig. 2.6. An error vector represents a difference between an actual vector and a reference vector. Hence, it is evaluated as logarithmic function with ratio of amplitude of error signal, P_{error}, to amplitude of reference signal, P_{ref}, as EVM (dB)$= 10\log_{10}\left(\frac{P_{error}}{P_{ref}}\right)$ or EVM$(\%) = 10\log_{10}\left(\frac{P_{error}}{P_{ref}}\right) * 100\%$. The EVM describes the combination of all

impairments that influence signal constellation in an additive way [37]. A low EVM value indicates less distortion noise presence. Hence, low EVM values are desired for a high rate and reliable communication. There are specifications on the EVM level for a given modulation type. For instance, for wideband code division multiple access that uses quadrature phase-shit keying (QPSK) EVM level should be no more than 17.5%, 3GPP LTE requirement for EVM is $8\%, 17.5\%$. The authors in [38] discusses the individual impact of each source of transceiver impairments on EVM including I/Q imbalance, non-linear power amplifier, local oscillator phase noise, as wellas local oscillator leakage. The overall EVM is expressed as a summation of all sub-EVMs from each source of circuit nonideality.

2.3.2.2 Transceiver Distortion Noise in MmWave Communication

The primary sources of transceiver hardware impairments in mmWave communication were listed as ADC/DAC resolution, I/Q imbalance in quadrature modulators, phase noise in phase-locked loops, and non-linearity in power amplifiers in [39]. The achievable rate of massive MIMO antennas considering hardware impairment noise over Rician fading channel was studied in [10]. The multipair massive MIMO system assisted by relay network evaluated spectral efficiency of the system by taking into account residual transceiver distortion noise. Transceiver distortion noise was deeply investigated in CR systems [40–42]. A cell-free massive MIMO network with transceiver distortion noise was analyzed in [43] where spectral and energy efficiencies of the system were extensively studied.

Chapter 3

Cognitive Relay Networks

In this chapter, the performance analysis of the dual-hop DF underlay CR network under residual transceiver distortion noise and interference power constraints is presented. Closed-form analytical calculations for the outage probability over independent and non-identical distributed (i.i.d.) Nakagami-m fading channels. Moreover, closed-form expressions for the outage probability asymptotic analysis are derived as well. We found a relation between hardware impairment level and possible transmission rate through numerical simulations. We have investigated different fading severity parameters of the fading channel given the fixed source node power and desired outage probability level. This chapter was written based on the author's work published in [44].

3.1 Introduction

CR networks contain many secondary nodes that could be used as relay nodes to facilitate cooperative communication between source-destination nodes to increase the throughput and coverage of the network by minimizing the factor of path loss between source-destination link. The relay assisted networks have been popular among researchers and industry due to increased coverage, high reliability, and improved quality of service. The secondary relay system contains the source (S), relay (R), and destination nodes (D). The secondary relay system operates at the same frequency as a primary one. The source node sends its signal to the relay node at the first time-slot. Depending on the relaying protocol, it could be either amplified and forwarded to the destination node, decoded

and forwarded or compressed, and forwarded. Hence, the major relaying protocols are amplify-and-forward (AF), DF, and compress-and-forward (CF).

3.1.1 Related work

One of the practical applications of the dual-hop network is an ad-hoc wireless network. The work in [45] integrated 3G Wireless Wide Area Network and 802.11 Wireless Local Area Network. A typical dual-hop relay network have an S, R, and D nodes that are assembled by non-ideal RF chains and communication blocks. Authors investigated dual-hop relay networks with non-ideal hardware in [46–49]. Moreover, the works in [40] and [50] studied the multiple relay CR networks under transceiver distortion noises over Rayleigh fading channels. Initially, a generalized system and signal model for a dual-hop relay network with aggregate distortion noises were introduced in [46]; this study models aggregate distortion noises as additive Gaussian noise as in [9]. The work in [40]- [47] applied the generalized non-ideal hardware impairment signal described in [46]. The authors in [47] evaluated closed-form formulas for the outage performance of a DF CR network non-ideal transceiver electronics by using practical 3GPP LTE EVM parameters for Rayleigh fading channel. According to this study, the system with a high data rate is more affected by distortion noises. The work in [48] analyzed the outage probability and throughput of a dual-hop relay network with distortion noises under Rayleigh fading channel. This study also demonstrated that the DF protocol is less susceptible to distortion noises in comparison to AF protocol. Multiple relay CR network with transceiver hardware impairments was analyzed in [50] over Rayleigh fading channel. Moreover, a partial relay selection and opportunistic techniques were studied in [40], and closed-form expressions for the outage probability were derived over Rayleigh fading channels. The authors in [51] studied the combined effect of distortion noise and channel estimation error for dual-hop CR network given ideal hardware over Nakagami-m fading channel. According to these studies, the outage probability saturates at high interference temperature values.

Based on the literature survey analysis, majority of the researchers analyzed dual-hop CR networks for non-ideal hardware under Rayleigh fading channel for analytical tractability purposes.

3.1.2 Contributions

The principal contributions of this chapter are listed as:

- Presentation of a system and signal model for the underlay dual-hop DF cognitive relay system with transceiver imperfections and interference constraints under Nakagami-m fading channel;
- Derivation of the analytical expression for the outage probability given dual-hop DF network under aggregate transceiver imperfections and interference constraints;
- Verification of the analytical outage probability expressions with Monte-Carlo simulations for $N = 10^6$ iterations at various interference temperature constraints, fading parameters, and hardware impairments levels;
- Delivering design aspects on the maximum hardware impairments level to meet the desired outage probability threshold for varying fading parameters.

3.1.3 Organization

3.2 System and Signal Model

We present a dual-hop CR relay network in Fig. 3.1 where a cognitive network consists of a S node that communicates to D node through relay R node. We consider the absence of the direct link between S and D nodes caused by a far distance. Cognitive relay system operates in a half-duplex mode: at the first time-slot the message is sent from S to R and at the second time-slot the signal gets forwarded from R to D nodes. Cross-channel information is required for underlay paradigm to enable coexistence of PU and SUs. Secondary/cognitive network imposes interference to the primary receiver (PR).

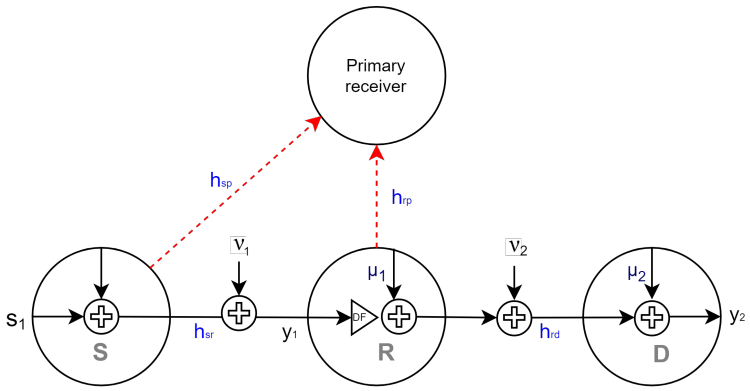

Figure 3.1. System and signal model for underlay dual-hop DF relay network under hardware impairments.

Power control of underlay paradigm assists to handle this interference. We consider i.i.d. Nakagami-m fading channel coefficients between primary and interference links, denoted as h_{sr}, h_{rd}, h_{sp} and h_{rp} with corresponding channel gain amplitudes $|h_{sr}|^2$, $|h_{rd}|^2$, $|h_{sr}|^2$, and $|h_{rp}|^2$ that follow Gamma distribution. Due to power control in a secondary network, a transmit power of S and R nodes are selected as a minimum value between interference temperature constraint, I, as well as a maximum available power at the S and R nodes P_1 and P_2, respectively, to eliminate the interference with primary network as in [51].

$$P_1 \leq \min\left\{\frac{I}{|h_{sp}|^2}, P\right\}, \tag{3.1}$$

$$P_2 \leq \min\left\{\frac{I}{|h_{rp}|^2}, P\right\}. \tag{3.2}$$

In Fig. 3.1, we present signal path from the S to D nodes. The original signals s_1 and s_2 originating from the S and R nodes are deteriorated by aggregate distortion noises $\mu_j \sim \mathcal{CN}\left(0, \kappa_j^2 P\right)$, where $P = \mathbb{E}\{|s_j|^2\}$ is an average power of the signal. In addition, $\kappa_j \geq 0, j = 1, 2$ represents an aggregate transceiver distortion noise level measured by the EVM. Moreover, μ_j represents circularly-symmetric complex Gaussian distributed variable that describes aggregate distortion noise from the transmitter and receiver nodes. A residual transceiver distortion noise model from a transmitter side is given as $\mu_t \sim \mathcal{CN}(0, \kappa_r^2 P|h|^2)$. Similarly, $\mu_r \sim \mathcal{CN}(0, \kappa_r^2 P|h|^2)$ stands for the aggregate distortion

noise from the receiver node. The summation of aggregate distortion noises from the transmitter and receiver nodes could be represented as $\mathbb{E}_{\mu}\{|h\mu_t + \mu_r|^2\} = P|h|^2(\kappa_t^2 + \kappa_r^2) = P|h|^2\kappa^2$. Authors in [46] stated that the hardware impairment level parameter, κ is inverse proportional to the outage probability threshold as, $\kappa \leq \frac{1}{x}$, where x is a predefined threshold on signal-to-noise-distortion ratio (SNDR). We denote κ_1 parameter between S and R nodes and κ_2 parameter between R and D nodes, respectively. In addition to distortion noises circularly-symmetric complex Gaussian distributed receiver noise ν_i is also added to the signal s_i, $\nu_i \sim \mathcal{CN}(0, N_i)$. Next, the generalized received signal for non-ideal system is formulated as

$$y_i = \sqrt{P_i}h_i(s_i + \mu_i) + \nu_i \quad i = 1, 2. \tag{3.3}$$

3.3 Outage Probability

This section presents closed-form expressions for the outage probability under the presence of transceiver distortion noises. The outage probability finds the probability of faded end-to-end SNDR to fall below a defined threshold, x as

$$P_{out}(x) = \Pr(\gamma \leq x), \tag{3.4}$$

where γ is the SNDR.

3.3.1 Signal-to-Noise-Distortion Ratio for underlay dual-hop DF network

The end-to-end SNDR for underlay dual-hop DF secondary relay network is evaluated as

$$\gamma = \min\left\{\frac{P_1|h_{sr}|^2}{P_1|h_{sr}|^2\kappa_1^2 + N_1}, \frac{P_2|h_{rd}|^2}{P_2|h_{rd}|^2\kappa_2^2 + N_2}\right\}. \tag{3.5}$$

We represent end-to-end SNDR per each hop as T_1 and T_2 for hop 1 and 2, respectively.

$$T_1 = \frac{\min(\frac{I}{|h_{sp}|^2}, P)|h_{sr}|^2}{\min(\frac{I}{|h_{sp}|^2}, P)|h_{sr}|^2\kappa_1^2 + N_1}, \quad \text{and} \quad T_2 = \frac{\min(\frac{I}{|h_{rp}|^2}, P)|h_{rd}|^2}{\min(\frac{I}{|h_{rp}|^2}, P)|h_{rd}|^2\kappa_2^2 + N_2}, \tag{3.6}$$

respectively.

3.3.2 Outage Probability

The outage probability for the underlay dual-hop DF secondary network is calculated by making use of (3.4) and independence of SNDRs for the hops 1 and 2 as follows

$$\begin{aligned} P_{out}(x) = \Pr(\min(T_1, T_2) < x) =& 1 - \Pr(T_1 > x)\Pr(T_2 > x) \\ &= 1 - (1 - F_{T_1}(x))(1 - F_{T_2}(x)), \end{aligned} \tag{3.7}$$

where F_{T_1} and F_{T_2} are CDFs of the SNDR for the hop 1 and 2, respectively. The derivation of CDFs for T_1 and T_2 random variables (RVs) are presented in Lemma 1.

Lemma 1 *Let us consider $|h_{xy}|^2$ is a non-negative RV and β_i, $i \in 1, 2$ with m_i, $i \in 1, 2$ are positive constants. The CDF of RV T is expressed as*

$$\begin{aligned} F_{T_j}(x) =& \frac{\gamma\left(m_1, \frac{\beta_1 x N_j}{P_j - xP_j\kappa_j^2}\right)}{\Gamma(m_1)} \frac{\gamma\left(m_2, \frac{\beta_2 I}{P_j}\right)}{\Gamma(m_2)} + \frac{\Gamma\left(m_2, \frac{I\beta_2}{P_j}\right)}{\Gamma(m_2)} - \frac{\beta_2^{m_2}}{\Gamma(m_2)} \sum_{t=0}^{m_1-1} \frac{\left(\frac{x\beta_1 {N_j}^2}{I(1-x\kappa_j^2)}\right)^t}{t!} \\ &\times \Gamma\left(m_2 + t, \left(\beta_2 + \frac{x\beta_1 {N_j}^2}{I(1-x\kappa_j^2)}\right)\frac{I}{P_j}\right)\left(\beta_2 + \frac{x\beta_1 {N_j}^2}{I(1-x\kappa_j^2)}\right)^{-m_2-t}, \end{aligned} \tag{3.8}$$

where $i = 1$ stands for channel parameters between S-R and R-D nodes, whereas, $i = 2$ indicates channel parametes between S-PR and $R - PR$ nodes. Moreover, m_i, $i \in 1, 2$ and β_i, $i \in 1, 2$ represent fading and scale parameters of the corresponding channels.

Proof: The proof is given in Appendix A. ■

By using Lemma 1, we formulate the outage probability for the dual-hop relay network with transceiver hardware impairment noise and interference constraints.

Lemma 2 *Let suppose that T_i is an independent non-negative RV with CDF $F_T(\cdot)$ for $i = 1, 2$. The outage probability for dual-hop DF cognitive relay network under distortion noise and interference temperature constraints is*

$$P_{out}(x) = \begin{cases} 1- & \left(1 - F_{T_1}\left(\frac{N_1 x}{P_1(1-\kappa_1^2 x)}\right)\right)\left(1 - F_{T_2}\left(\frac{N_2 x}{P_2(1-\kappa_2^2 x)}\right)\right), \ x < \frac{1}{\delta}, \\ 1, & x \geq \frac{1}{\delta}, \end{cases} \tag{3.9}$$

where $\frac{1}{\sigma} = \max(\kappa_1^2, \kappa_2^2)$ By substituting (3.8) to (3.9), we obtain the analytical formula for the outage probability over Nakagami-m fading channel.

3.3.3 Asymptotic Analysis for the Outage Probability

We analyze the asymptotic outage probability given two extreme conditions: 1) a source power approaches infinity and 2) interference temperature constraint approaches to zero.

3.3.3.1 Outage probability when $P \to \infty$

We evaluate the outage probability given an infinite source power

$$P_{out}(x) = 1 - (1 - \lim_{P\to\infty} F_{T_1}(x))(1 - \lim_{P\to\infty} F_{T_2}(x))), \tag{3.10}$$

$$\begin{aligned} \lim_{P\to\infty} F_{T_j}(x) = 2 + \frac{\beta_{j2}^{m_{j2}}}{\Gamma(m_{j2})} \sum_{i=0}^{m_{j1}-1} \frac{\left(\frac{x\beta_{j1}N_j^2}{I(1-x\kappa_i^2)}\right)^i}{i!} \\ \times \Gamma(m_{j2}+i)\left(\beta_{j2} + \frac{x\beta_{j1}N_j^2}{I(1-x\kappa^2)}\right)^{-m_{j2}-i}. \end{aligned} \tag{3.11}$$

From (3.10) one could notice interference temperature constraint limits the secondary network operation despite infinite power available at the transmitter. Hence, the outage probability of the secondary network is dependent on I.

3.3.3.2 Outage Probability when $I \to 0$

Let us consider that interference temperature constraint value approaches to zero, then the CDF of SNDR approximates to one shown as

$$\lim_{I \to 0} F_T(x) \approx 1, \tag{3.12}$$

Therefore, the outage probability at $I \to 0$ is evaluated as

$$P_{out}(x) = 1 - (1 - \lim_{I \to 0} F_{T_1}(x))(1 - \lim_{I \to 0} F_{T_2}(x))), \tag{3.13}$$

$$P_{out}(x) \approx 1. \tag{3.14}$$

The outage probability approximates to one when I approaches to zero and primary network does not allow any communication in secondary network.

3.4 Simulation Results

In this section, the theoretical closed-form expression for the outage probability is validated through MATLAB Monte-Carlo simulations. We emphasize on the influence of interference temperature constraints, fading parameter values, and aggregate distortion noise level on the performance of the outage probability. We plot the outage probability versus P/N_0 in Fig. 3.2 given a set of interference temperature constraints I/N_0=0; 10; 15; 20 dB for $\kappa = 0.1$. In addition, we analyze the outage probability at interference temperature constraint at zero; as expected, the secondary network is at idle state and the outage probability is equal to one. Notice that the outage probability performance enhances as I value increases.

In Fig. 3.3, the outage probability is displayed as an element of P/N_0 for I/N_0=15 dB and $x = 3$ dB. Note that, dotted plots represent the outage probability at $\kappa = 0.4$ and the solid plots denote outage probability at $\kappa = 0.1$. Moreover, we simultaneously differ two major parameters: 1) hardware impairment level, κ, at low and high values

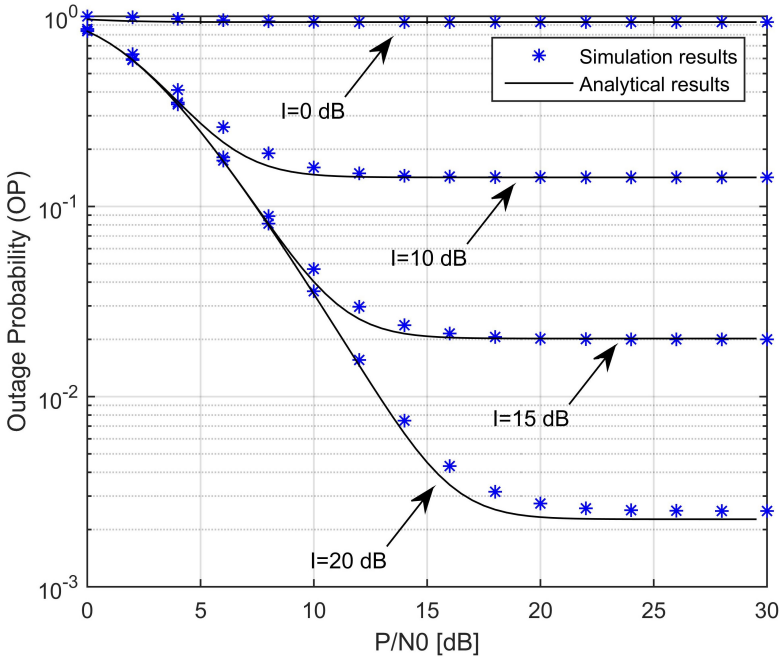

Figure 3.2. Outage probability versus P/N_0 at different $I/N_0 = 0$, 10, 15, 20 (dB).

Table 3.1. The fading parameter values for Fig. 3.3

Case	m_{sr}	m_{sp}	m_{rd}	m_{rp}	κ_2	κ_2
a)	2	2	2	2	0.1	0.4
b)	2	10	2	10	0.1	0.4
c)	5	5	5	5	0.1	0.4

and 2)Nakagami-m fading parameters m_{sr} $(S-R)$, m_{rd} $(R-D)$, m_{sp} $(S-PR)$, m_{rp} $(R-PR)$ at a) identical low fading parameters of both cognitive and interference links; b) at low cognitive fading parameters and high interference fading parameters; c) at identical medium fading parameters of cognitive and interference links. Table 3.1 above summarizes fading parameters of three cases that are used to plot Fig. 3. The plot (c) with medium m_{xy} fading parameters of both cognitive and interference links demonstrated the best outage probability performance. The plot (a) with identically low m_{xy} parameters shows the second high outage probability performance. The plot (b) shows the worst outage probability performance. This figure justifies that residual transceiver distortion noise level plays a crucial role in evaluating the outage probability. Moreover, fading parameter values of both primary and secondary links substantially affect the outage probability performance.

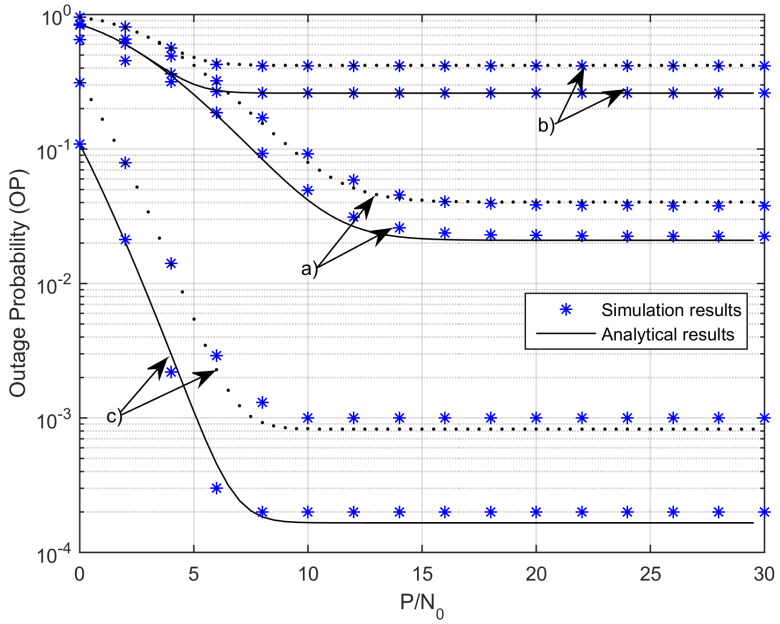

Figure 3.3. Outage Probability at different fading parameters simulated for $\kappa = 0.1$ and $\kappa = 0.4$.

In Fig. 3.4, we analyze the relationship between SNDR threshold, x and hardware imapirment level κ. According to [46], $\kappa^2 < 1/x$. Alternatively, we could express the threshold by using the rate as $\kappa < 1/2^{2\Delta-1}$, where Δ is a transmission rate [bits/s]. Moreover, rate could be written as $\Delta = aR_s$, where a represents a number of bits per each modulated symbol and R_s indicates symbol rate [symbol/s]. Since high rate systems require

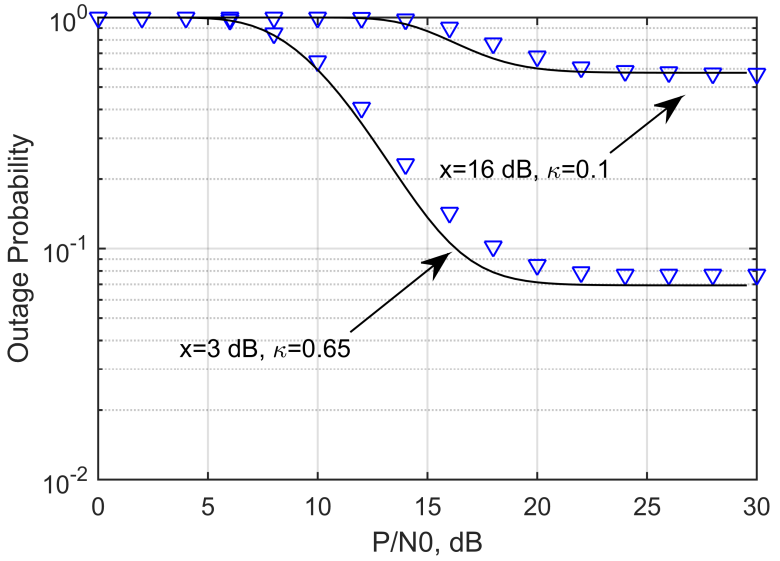

Figure 3.4. The outage probability plots for $x = 3; 16$ dB and $\kappa = 0.1; 0.65$.

a higher order of modulation, κ values are inversely proportional to the modulation type and transmission symbol rate. The level of tolerated hardware impairment level is written in standards. For example, in 3GPP LTE standard, $\kappa_{BPSK} = \kappa_{QPSK} = 0.175$ [52], and for IEEE $802.11n$ standard, $\kappa_{BPSK} = 0.3162$, $\kappa_{QPSK} = 0.1$ and $\kappa_{16QAM} = 0.025$ [53]. In Fig. 4 we study a dual-hop system with thresholds $x = 3; 16$ dB. By using $\kappa_i < 1/x_i$ inequality we approximate the maximum tolerated hardware impairment level as $\kappa_1(x = 3 \text{ dB}) < 0.7$ and $\kappa_2(x = 16 \text{ dB}) < 0.15$. We use those values for simulation purposes and set $\kappa_1 = 0.65$ given $x = 3$ dB and $\kappa_2 = 0.1$ for $x = 16$ dB and analyze the performance of outage probability. At high κ_1 value system saturates if $P/N_0 < 6$ dB, whereas at low κ_2 value system goes to outage state while $P/N_0 < 14$ dB. From Fig. 4, we highlight that low rate systems tolerate higher distortion levels than the high rate systems and result in higher outage probability performance.

3.5 Design Aspects

By applying the outage probability formula and MATLAB's built-in function **fsolve**, one could determine the range of κ values for corresponding m_{xy} fading parameters to satisfy the specific outage probability value. By using the inverse proportionality between residual transceiver distortion level and transmission rate, one could obtain design guidelines for the modulation type and transmission rate. For simulation purposes, we propose to use $P_{out} = 0.01$, $x = 3$ dB, $P_1/N_0 = P_2/N_0 = 20$ dB, $m_{sp} = m_{rp} = 3$, m_{sr} and m_{rd} are within 1 to 6 and we evaluate for κ_1, κ_2. The outage probability formula given in (3.9) is a function of four fading parameters that is necessary for κ evalutation by **fsolve**. Hence, distortion level κ is a four dimensional matrix as well. In Fig. 3.5 and 3.6, we plot κ_1^2 and κ_2^2 for varying m_{sr} and m_{rd}, while m_{sp} =$m_{rp} = 3$. The simulation results for κ_2^2 are presented in Table 3.2 that resembles multiplication table. The top numbers represents the range of m_{rd} values, left side numbers stands for m_{sr} values, and inner values are corresponding κ_2^2 values.

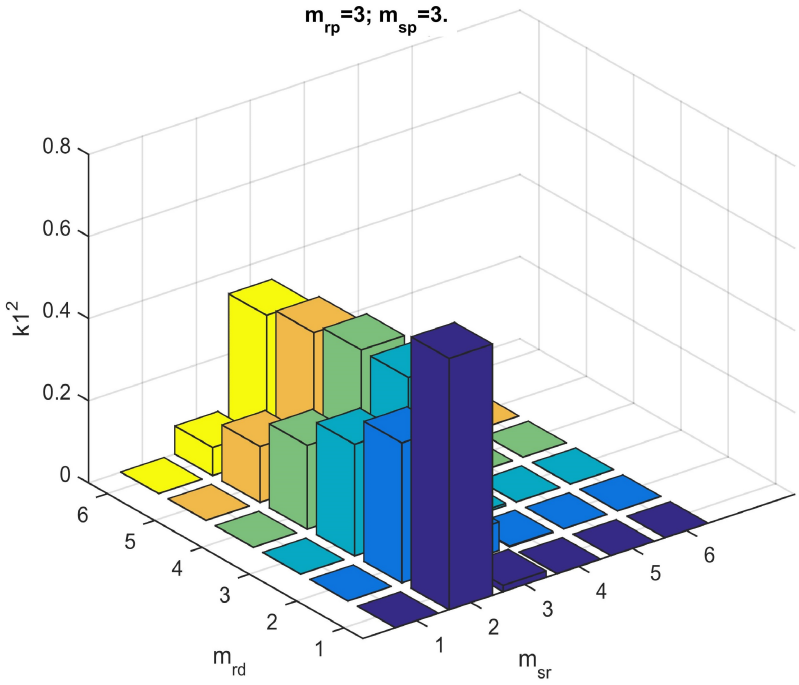

Figure 3.5. Evaluated κ_1 values at $m_{sp} = m_{rp} = 3$, $m_{sr} = m_{rd}$=1:6.

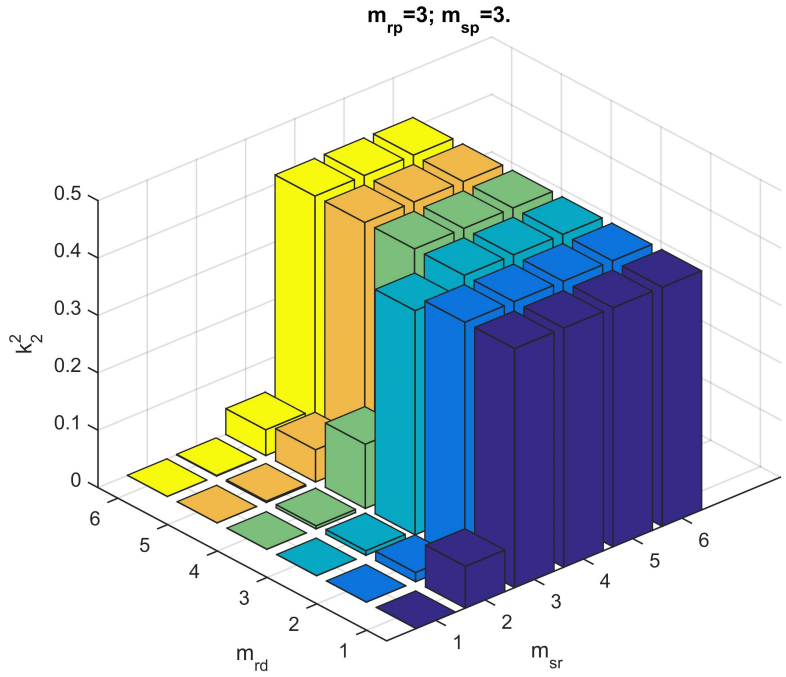

Figure 3.6. Calculated results for κ_2, when $m_{sp} = m_{rp} = 3$, $m_{sr} = m_{rd}$=1 : 6.

Table 3.2. Calculated κ_2 values for $m_{sp} = m_{rp} = 3$, $m_{sr} = m_{rd} = 1:6$

${\kappa_2}^2$				m_{rd}		
m_{sr}	1	2	3	4	5	6
1	0	0	0	0	0	0
2	0.0727	0.01	0	0.005	0.023	0
3	0.4165	0.4165	0.39	0.118	0.056	0.044
4	0.4165	0.4165	0.42	0.4165	0.4165	0.41
5	0.4165	0.4165	0.42	0.4165	0.4165	0.41
6	0.4165	0.4165	0.42	0.4165	0.4165	0.41

3.6 Chapter Summary

In this Chapter, underlay cognitive DF relay network under residual transceiver hardware impairments and interference temperature constraints is studied. Physical transceivers distort the original signal and deteriorate the system performance. It was noted that transmission rate is inversely proportional to level of hardware impairments. We evaluated closed-form expression of the outage probability for the underlay dual-hop DF cognitive relay system. In addition, the asymptotic analysis for the high power system and nearly zero interference temperature constraint was performed. Based on simulation results we confirm that low fading parameters at interference links improve the system performance and high fading parameters of cognitive links degenerate the outage probability performance. Therefore, fading parameters of interference/cognitive links have an important impact on the outage probability. Moreover, we presented design aspects of estimating a maximum allowable hardware impairment level given the threshold on SNDR.

Chapter 4

Spectrum Sensing using Improved ED under Residual Hardware Impairments

The accuracy of spectrum sensing is affected by transceiver hardware in a low-cost and high rate CR systems. Ideal hardware is a common assumption in spectrum sensing technical literature. This chapter presents a novel method that calculates statistics of improved ED for non-ideal transceiver hardware by using α-μ distribution over AWGN and Nakagami-m fading channels. The AUC performance for improved ED constrained by hardware impairment was studied for the AWGN channel. Moreover, we study asymptotic analysis for detection probability at a low SNR over Nakagami-m fading channel. The improved ED performance was enhanced by using p-order law combining and p-order law selecting diversity techniques that increase the accuracy of the detector. Simulation results validate that the proposed diversity techniques substantially boost the detector's performance. The author's publication in [54] inspired this chapter.

4.1 Introduction

An improved energy detector is a type of non-coherent energy detector that detects the presence of a PU in CR networks. The conventional ED is a square-law device that measures the power of the signal over a certain period and decides whether the PU signal is present or not in [55]. The improved ED raises the signal amplitude to the arbitrary power p over a period of time [56]. The major advantage of non-coherent EDs as conventional

ED, improved ED, and matched filter, is that they do not require CSI and provide a fast decision response.

4.2 Related work

Authors in [55–58] demonstrated that the improved ED outperforms the conventional ED. Distribution of the improved ED test statistics was evaluated by using Gamma function approximations that match the mean and variance of H_0 and H_1 hypotheses over AWGN. The improved ED was used in a cooperative spectrum sensing CR network by using multiple antenna elements, where numerical results have demonstrated a substantial detection accuracy of the improved ED in comparison to the conventional ED. The improved ED was also utilized in a cooperative cognitive network over the generalized Nakagami-q, Nakagami-m, $\kappa-\mu$, $\nu-\mu$ channels by authors in [58], where the performance of the detector was evaluated by using the receiver operating characteristic (ROC) and AUC analysis. A censoring-based cooperative spectrum sensing CR network [59] over Rayleigh, Rician, and Hoyt fading channels stated that the censoring threshold of a secondary user has a major effect on the average miss detection probability. Moreover, reporting and sensing channels shown a better performance at a higher number of SUs, antenna elements, and SNR. The authors in [14] states that a major disadvantage of cooperative spectrum sensing is the necessity of a large number of SUs that result in latency while decision-making. The authors in [60] added selection combining diversity for cooperative CR with improved ED spectrum sensing given cognitive user mobility and imperfect CSI. This work evaluated the probability of miss detection, probability of false alarm, and error performance over a Rayleigh fading channel, the limitation of this work is that detector statistics were evaluated based on one signal sample. Similarly, the authors in [61] used antenna selection diversity for a cooperative spectrum sensing network over AWGN and Rayleigh fading channels, where PU detection was determined according to one sample of improved ED statistics. The main finding of [61] was providing optimization analysis for an optimum number of normalized SUs and threshold values. Adverse effects of hardware impairment

noises were mitigated in blind and robust spectrum sensing in [62]. Non-linearity of RF frequency components was removed with the aid of mitigation algorithms. Hardware implementation of the two-stage mitigation algorithms that measure real data includes two software-defined radio blocks, $N210$, and $USRP$s. Furthermore, theoretical results were validated by experimental data. Improvement in the performance of false alarm probability by using a mitigation algorithm was theoretically and practically verified by the authors in [62]. Moreover, Boulogeorgos $et\ al.$ in [42] provided an in-depth analytical analysis of spectrum sensing for the conventional energy detector under RF hardware impairments. Authors modelled hardware impairment noises from direct conversion radio receivers such as IQ imbalance, phase noise, and low noise amplifier non-linearity for the multichannel environment. This work verified that hardware impairment noises degraded the accuracy of spectrum sensing. Four level hypotheses test for conventional energy detector with IQ imbalance was presented in [24], and outage probability performance was investigated for the CR network based on the OFDM system. A novel spectrum sensing mechanism called robust swept-multi-band spectrum sensing (RS-MSS) was proposed by [22] that studied aliasing and IQ imbalance in multi-band spectrum sensing. The accuracy of spectrum sensing was improved with the proposed RS-MSS technique that removes aliasing and distortion noise from IQ imbalance. This study models the receiver by using a channelized spectrum representation and verify the RS-MSS technique by hardware experiments. Eigenvalue-based detectors, namely Wald and Rao's detectors, were used in SIMO CR systems, where the IQ imbalance of the transmitter distorts a receiver. The Wald detector outperformed the Rao detector and was prone to the receiver IQ imbalance. There have been numerous studies to investigate direct conversion radio receivers for low cost CR systems. The authors in [23, 63] studied IQ imbalance and oscillator phase noise in multichannel direct conversion radio receivers. An enhanced energy technique was offered in this work to eliminate IQ imbalance and oscillator phase noise to increase detection accuracy. Similarly, the authors in [64] studied IQ imbalance in single and multichannel spectrum sensing in full-duplex CR by using the conventional ED. The seminal contribution of this work is studying the effect of transceiver hardware

impairment effect on the performance of wireless systems.

It is vital to consider practical transceiver electronics while designing accurate spectrum sensing detectors. As far as we know, no previous research investigated hardware distortion noise for the improved ED, which is an important tool in developing reliable detectors. Hence, in this work, we study the aggregate effect of residual distortion noise on the detection performance of the improved ED. Moreover, we propose p-order law selection and p-order law combining diversity techniques to improve the detection accuracy of the improved EDs.

4.3 Contributions

- A novel method of calculating test statistics for the improved ED by using $\alpha - \mu$ distribution for a signal with N samples given ideal and non-ideal transceiver hardware.
- The AUC analysis of the proposed improved ED was performed both for ideal and non-ideal transceiver hardware for AWGN channel.
- Average detection probability was analytically and evaluated over Nakagami-m fading channels both for ideal and non-ideal transceiver hardware. Closed-form expressions are presented probability of detection over AWGN channels for p-order law selection and p-order law combining diversity techniques given ideal and non-ideal transceiver hardware. Similarly, closed-form expressions are derived for average detection probability over Rayleigh/Nakagami-m fading channels for ideal/non-ideal system configurations.
- Average detection probability at asymptotically low SNR has been derived.
- According to numerical results, detection probability degrades as a level of hardware distortion noise increases. On the other hand, diversity techniques maintain the spectrum sensing performance of the CR system.

- Total error rate analysis has been performed to compare the detection performance of a single, and diversity improved ED's performance for ideal and non-ideal improved ED configurations.

The rest of this chapter is organized as follows. Section 4.4 introduces a spectrum sensing CR system with improved ED under residual distortion noise constraints. Section 4.5 presents a novel formulation of the improved ED by using $\alpha - \mu$ distribution. Detection and false alarm probabilities of the practical improved ED over AWGN channel are given in Section 4.6. Moreover, the average detection probability that is subjected to Nakagami-m fading channel is derived in Section 4.7. Diversity techniques for the improved ED are applied, and closed-form expressions for the detection and false alarm probabilities over AWGN and Nakagami-m fading channels are described in Section 4.8.

4.4 System Model

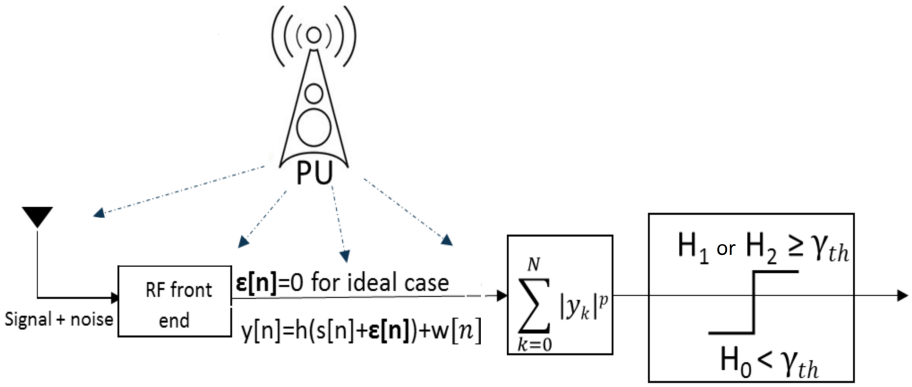

Figure 4.1. System model for the improved ED for non-diversity SU receiver.

In Fig.4.1, we present a system model for the CR system, where a PU with a single antenna coexists with a SU. Meanwhile, the SU deploys improved ED to detect the activity of the PU. Based on the detected SU's power, a two-level hypotheses test is applied for both ideal and non-ideal system hardware to determine spectrum holes. We denote H_0 as a hypothesis test that the signal is absent, oppositely, H_1 denotes the presence of the PU signal in Gaussian noise channel. Further, we denote H_2 hypothesis test to detect a

non-ideal transceiver signal in Gaussian noise.

$$\begin{aligned} H_0 &: y[n] = w[n] \\ H_1 &: y[n] = hs[n] + w[n] \\ H_2 &: y[n] = h(\varepsilon[n] + s[n]) + w[n], \end{aligned} \tag{4.1}$$

where $s[n]$ is a complex PU signal with average signal power, $P = \mathbb{E}\{|s[n]|^2\}$. We assume that h is Nakagami-m fading channel. Moreover, $w[n]$ is circularly symmetric complex Gaussian noise variable with zero mean and σ_w^2 variance $w[n] \sim \mathcal{CN}(0, \sigma_w^2)$. Aggregate residual hardware distortion noise from Tx and Rx hardware is modelled as additive Gaussian noise with zero mean and $\kappa^2 P$ variance, where $\varepsilon[n] \sim \mathcal{CN}(0, \kappa^2 P)$. Note that κ indicate hardware impairment level both from the Tx and Rx is measured by EVM. Hence, the instantaneous signal-to-noise-distortion ratio (SNDR) of the system with hardware distortion noise is formulated as

$$\gamma_{\text{hi}} = \frac{|h|^2 P}{|h|^2 \kappa^2 P + \sigma_w^2} = \frac{\gamma}{\kappa^2 \gamma + 1}, \tag{4.2}$$

where γ is the instantaneous SNR that is evaluated as $\gamma = \frac{P|h|^2}{\sigma_w^2}$.

4.5 Improved Energy Detector with Transceiver Distortion Noise

A novel derivation for the improved ED test statistics is presented in this section. A single sample of the improved ED is Weibull distributed RV. Since the improved ED test statistics is based on N signal samples, we apply summation of N independent and not identically distributed (i.n.i.d.) Weibull RVs, which is approximated as α-μ distribution. The hypothesis test for improved ED is formulated as follows

$$\Lambda = \sum_{i=1}^{N} Y_i \underset{H_0}{\overset{H_1, H_2}{\gtrless}} \gamma_{th}, \tag{4.3}$$

and

$$Y_i = \left(\frac{|y_i|}{\sigma_w}\right)^p, \tag{4.4}$$

where Λ is the test statistics for the hypothesis test that determines the presence of PU signal, Y_i is a single sample of the improved ED normalized the noise power, γ_{th} is a predefined threshold, N is the number of signal samples, and p is a positive detector order. The conditional PDFs for the H_0 and H_1 hypotheses tests are formulated as follow $f_{Y_i|H_0}(x)$ and $f_{Y_i|H_1}(x)$, respectively, and given as

$$f_{Y_i|H_0}(x) = \frac{2x^{\frac{2-p}{p}} \exp(-x^{\frac{2}{p}})}{p}, \tag{4.5}$$

$$f_{Y_i|H_1}(x) = \frac{2x^{\frac{2-p}{p}} \exp(-\frac{x^{\frac{2}{p}}}{1+\gamma})}{p(1+\gamma)}. \tag{4.6}$$

Similarly, we formulate the PDF of H_2 hypothesis as following

$$f_{Y_i|H_2}(x) = \frac{2x^{\frac{2-p}{p}} \exp(-\frac{x^{\frac{2}{p}}}{1+\gamma_{\text{hi}}})}{p(1+\gamma_{\text{hi}})}. \tag{4.7}$$

By analyzing the PDFs of $H_0 - H_2$ hypotheses in 4.5-4.7, we notice that they follow Weibull distribution given as [65]

$$f(x|a,b,c) = \frac{c}{b}\Big(\frac{x-a}{b}\Big)^{(c-1)} \exp\Big\{-\Big(\frac{x-a}{b}\Big)^c\Big\}, \tag{4.8}$$

where $x \geq a; a \in \mathbb{R}; b, c \in \mathbb{R}^+$ and $\mathbb{R}$ denotes real numbers. According to [66], a simple and precise approximation for the sum of N i.n.i.d. Weibull RVs is given as $\alpha - \mu$ distribution. Corresponding PDF and CDF of α-μ distribution are given in [67] as

$$f_\Lambda(x) = \frac{\alpha\mu x^{\alpha\mu-1}}{\Omega^\mu \Gamma(\mu)} \exp(-\frac{\mu x^\alpha}{\Omega}), \tag{4.9}$$

$$F_\Lambda(x) = 1 - \frac{\Gamma(\mu, \frac{\mu x^\alpha}{\Omega})}{\Gamma(\mu)}, \tag{4.10}$$

respectively, where $\alpha > 0$ is a shape parameter, $\mu = \mathbb{E}^2[\Lambda^\alpha]/\sigma_{\Lambda^\alpha}$ is an inverse of the normalized variance, $\Omega = \mathbb{E}[\Lambda^\lambda]$ is a scale parameter. To find the parameters of α-μ distribution such as α, μ, and Ω, it is necessary to evaluate moment based estimators of these parameters and exact moment based estimators of Λ. Next, the system of equations given below is numerically solved to find α and μ parameters as

$$\frac{\Gamma^2(\mu+\frac{1}{\alpha})}{\Gamma(\mu)\Gamma(\mu+\frac{2}{\alpha})-\Gamma^2(\mu+\frac{1}{\alpha})} = \frac{\mathbb{E}^2[\Lambda]}{\mathbb{E}[\Lambda^2]-\mathbb{E}^2[\Lambda]}, \tag{4.11}$$

$$\frac{\Gamma^2(\mu+\frac{2}{\alpha})}{\Gamma(\mu)\Gamma(\mu+\frac{4}{\alpha})-\Gamma^2(\mu+\frac{1}{\alpha})} = \frac{\mathbb{E}^2[\Lambda^2]}{\mathbb{E}[\Lambda^4]-\mathbb{E}^2[\Lambda^2]}, \tag{4.12}$$

where the first, second, and fourth order moments of the improved ED test statistics such as $\mathbb{E}[\Lambda]$, $\mathbb{E}[\Lambda^2]$, and $\mathbb{E}[\Lambda^4]$ are evaluated by

$$\begin{aligned}\mathbb{E}[\Lambda^n] = \sum_{n_1=0}^{n}\sum_{n_2=0}^{n_1}\cdots\sum_{n_{N-1}=0}^{n_{N-2}}\binom{n}{n_1}\binom{n_1}{n_2}\cdots\binom{n_{N-2}}{n_{N-1}} \\ \times \mathbb{E}[\Lambda_1^{n-n_1}]\mathbb{E}[\Lambda_2^{n_1-n_2}]\cdots\mathbb{E}[\Lambda_N^{n_{N-1}}],\end{aligned} \tag{4.13}$$

where n is the order of the moment and expectation of Λ_i^n is found as

$$\mathbb{E}[\Lambda_i^n] = \Phi^{\frac{n}{\beta}}\Gamma\left(1+\frac{n}{\beta}\right), \tag{4.14}$$

where we make following assumptions: $\beta = 2/p$ and $\Phi = 1$ for H_0 hypothesis, as well as $\Phi = 1+\gamma$ for H_1 hypothesis, and finally, $\Phi = 1+\gamma_{\text{hi}}$ for H_2 hypothesis. A full derivation of the Λ moments are given in Appendix B.1. Here, we summarize the closed-form expressions for the first, second, and fourth order moments of Λ as

$$\mathbb{E}[\Lambda] = N\Phi^{\frac{1}{\beta}}\Gamma\left(\frac{1}{\beta}+1\right), \tag{4.15}$$

$$\mathbb{E}[\Lambda^2] = (N-1)N\Phi^{\frac{2}{\beta}}\left(\Gamma(\frac{1}{\beta}+1)\right)^2 + N\Phi^{\frac{2}{\beta}}\Gamma\left(\frac{2}{\beta}+1\right), \tag{4.16}$$

$$\begin{aligned}\mathbb{E}[\Lambda^4] = N\Phi^{\frac{4}{\beta}}\Bigg(&\Gamma(\frac{4}{\beta}+1) + (N-3)(N-2)(N-1)N \\ &\times\left(\Gamma(\frac{1}{\beta}+1)\right)^4 + 6(N-2)(N-1)\Gamma(\frac{2}{\beta}+1) \\ &\times\left(\Gamma(\frac{1}{\beta}+1)\right)^2 + 4(N-1)\Gamma(\frac{3}{\beta}+1)\Gamma(\frac{1}{\beta}+1) + 3(N-1) \\ &\times\left(\Gamma(\frac{2}{\beta}+1)\right)^2\Bigg).\end{aligned} \tag{4.17}$$

Next, the calculate Ω parameter used in (4.10). Inspired by [66], we evaluate Ω as a function of α and μ parameters as

$$\Omega = \left(\frac{\mu^{\frac{1}{\alpha}}\Gamma\left(\mu\right)\Phi^{\frac{1}{\beta}}N\Gamma\left(\frac{1}{\beta}+1\right)}{\Gamma\left(\mu+\frac{1}{\alpha}\right)}\right)^{\alpha}, \tag{4.18}$$

where α and μ parameters numerically solved from the set of two equations given by (4.11)-(4.14).

4.6 Detection and False Alarm Probabilities over AWGN Channels

In this section, closed-form formulas are evaluated for the probability of detection and false alarm given ideal and hardware impaired transceiver over AWGN channel. We analyze the performance of the improved ED by doing AUC performance analysis.

4.6.1 Probability of False Alarm over AWGN Channel

By using the CDF of α-μ distribution given in (4.12) and applying the Ω parameter definition given in (4.18), we formulate the false alarm probability of the improved ED over

AWGN channel as

$$P_F = \Pr(\Lambda > \gamma_{th}|H_0) = \frac{1}{\Gamma(\mu_0)}\Gamma\left(\mu_0, \frac{\gamma_{th}^{\alpha_0}}{\left(\frac{\Gamma(\mu_0)N\Gamma(1+\frac{1}{\beta})}{\Gamma(\mu_0+\frac{1}{\alpha_0})}\right)^{\alpha_0}}\right) = \frac{1}{\Gamma(\mu_0)}\Gamma(\mu_0, \psi_0), \tag{4.19}$$

where α_0 and μ_0 parameters are calculated by equations (4.11)-(4.12) with $\Phi = 1$ and for notation simplicity we define $\psi_0 = \left(\frac{\gamma_{th}\Gamma\left(\mu_0+\frac{1}{\alpha_0}\right)}{N\Gamma\left(1+\frac{1}{\beta}\right)\Gamma(\mu_0)}\right)^{\alpha_0}$.

4.6.2 P_D^{id} for Ideal System Model

Probability of detection for the improved ED over AWGN channel is evaluated by using the CDF of α-μ distribution given in (4.12) and applying the Ω in (4.18) with $\Phi = \gamma + 1$ given as

$$\begin{aligned} P_D^{\text{id}} = \Pr(\Lambda > \gamma_{th}|H_1) &= \frac{\Gamma\left(\mu_1, \frac{\mu_1\gamma_{th}^{\alpha_1}}{\Omega}\right)}{\Gamma(\mu_1)} \\ &= \frac{1}{\Gamma(\mu_1)}\Gamma\left(\mu_1, \frac{\gamma_{th}^{\alpha_1}}{(\gamma+1)^{\frac{\alpha_1}{\beta}}\left(\frac{\Gamma(\mu_1)N\Gamma(1+\frac{1}{\beta})}{\Gamma(\mu_1+\frac{1}{\alpha_1})}\right)^{\alpha_1}}\right) \\ &= \frac{1}{\Gamma(\mu_1)}\Gamma\left(\mu_1, \frac{\psi_1}{(1+\gamma)^{\frac{\alpha_1}{\beta}}}\right), \end{aligned} \tag{4.20}$$

where α_1 and μ_1 parameters are calculated using (4.11) and (4.12). In addition, $\psi_1 = \left(\frac{\gamma_{th}\Gamma\left(\mu_1+\frac{1}{\alpha_1}\right)}{N\Gamma\left(1+\frac{1}{\beta}\right)\Gamma(\mu_1)}\right)^{\alpha_1}$.

4.6.3 P_D^{hi} for Hardware-impaired System Model

To evaluate probability of detection for the improved ED over AWGN channel under non-ideal transceiver electronics, we formulate a new Weibull moment, Λ_i^n, of order n to

incorporate transceiver distortion noise as

$$\mathbb{E}[\Lambda_i^n] = \left(\frac{\gamma}{\gamma\kappa^2+1}+1\right)^{\frac{n}{\beta}} \Gamma\left(1+\frac{n}{\beta}\right). \tag{4.21}$$

Next, by using (4.10) and (4.21), we calculate detection probability, P_D^{hi}, for the improved ED under transceiver impairments as follows

$$\begin{aligned} P_D^{\text{hi}} &= \Pr(\Lambda > \gamma_{th}|H_2) = \frac{\Gamma\left(\mu_1, \frac{\mu_1\gamma_{th}^{\alpha_1}}{\Omega}\right)}{\Gamma(\mu_1)} \\ &= \frac{1}{\Gamma(\mu_1)}\Gamma\left(\mu_1, \frac{\gamma_{th}^{\alpha_1}}{(\frac{\gamma}{\gamma\kappa^2+1}+1)^{\frac{\alpha_1}{\beta}}\left(\frac{\Gamma(\mu_1)N\Gamma(1+\frac{1}{\beta})}{\Gamma(\mu_1+\frac{1}{\alpha_1})}\right)^{\alpha_1}}\right) \\ &= \frac{1}{\Gamma(\mu_1)}\Gamma\left(\mu_1, \frac{\psi_1}{(\frac{\gamma}{\gamma\kappa^2+1}+1)^{\frac{\alpha_1}{\beta}}}\right), \end{aligned} \tag{4.22}$$

where α_1, μ_1, and ψ_1 definitions are presented in the previous sub-section.

4.6.4 AUC analysis for AWGN Channel

According to [69], the AUC is a figure of merit that evaluates the detection efficiency of an energy detector. The AUC value ranges from 0.5 to 1 with a higher value representing a better detector. Besides, the AUC changes with instantaneous SNR values. The general expression for the AUC over Gaussian channel is given in [69] as

$$A(\gamma) = \int_0^1 P_D(\gamma, \gamma_{th}) dP_F(\gamma_{th}). \tag{4.23}$$

By utilizing P_D in (4.20) and P_F in (4.19) we obtain a general expression for the AUC as

$$A(\gamma) = \frac{\Gamma(\mu_1+\mu_0)}{\Gamma(\mu_1)\Gamma(\mu_0)} \frac{\psi_0^{\mu_0}\left(\frac{\eta}{(\gamma+1)^{\frac{\alpha_1}{\beta}}}\right)^{\mu_1}}{\mu_0\left(\frac{\eta}{(\gamma+1)^{\frac{\alpha_1}{\beta}}}+\psi_0\right)^{\mu_1+\mu_0}} {}_2F_1\left(1;\mu_0+\mu_1;\mu_0+1;\frac{\psi_0}{\psi_0+\frac{\eta}{(\gamma+1)^{\frac{\alpha_1}{\beta}}}}\right), \tag{4.24}$$

where ${}_2F_1(;;;)$ is the Gauss hypergeometric function [68], $\eta = \left(\frac{\Gamma(\mu_1+1)}{\Gamma(\mu_1 N\Gamma(\frac{1}{\beta}+1)}\right)^{\alpha_1}$, $\mu_0 > 0$, and $(\mu_0+\mu_1) > 0$. Similarly, the AUC expression for non-ideal transceiver hardware is found by substituting γ in (4.24) with γ_{hi} in (4.2) as $A(\gamma_{\text{hi}})$. Hence, the average AUC for the Gaussian channel is evaluated by calculating the AUC as a function of average SNDR, $\bar{\gamma}$. A detailed derivation of the AUC over AWGN channel is provided in Appendix B.2.

4.7 Average Detection Probabilities over Nakagami-m Fading Channels

In this section, we study average detection probability of the improved ED over Nakagami-m fading channels for ideal and non-ideal transceiver hardware denoted as $\bar{P}^{\text{id}}_{D\text{Nak}}$ and $\bar{P}^{\text{hi}}_{D\text{Nak}}$, respectively.

4.7.1 $\bar{P}^{\text{id}}_{D\text{Nak}}$ for Ideal Transceiver Hardware

When channel magnitude follows Nakagami-m distribution the PDF of SNR is Gamma distributed RV given as

$$f_{\text{Nak}}(\gamma) = \frac{1}{\Gamma(m)}\left(\frac{m}{\bar{\gamma}}\right)^m \gamma^{m-1}\exp\left(-\frac{m}{\bar{\gamma}}\gamma\right), \gamma > 0, \tag{4.25}$$

where $m \geq 1$ is a shape parameter that represents fading coefficient of the channel. We could obtain the average detection probability for ideal improved ED over Nakagami-m fading channel by averaging detection probability, P_D^{id} in (4.20), over the PDF of Nakagami-m fading channel in (4.25). Hence, we calculate average detection probability over fading channel $\bar{P}_{D\text{Nak}}^{\text{id}}$ as

$$\begin{aligned}\bar{P}_{D\text{Nak}}^{\text{id}} &= \int_0^{\infty} P_D^{\text{id}} f_{Nak}(\gamma) d\gamma \\ &= \int_0^{\infty} \frac{1}{\Gamma(m)} \frac{1}{\Gamma(\mu_1)} (\frac{m}{\bar{\gamma}})^m \gamma^{m-1} e^{-\frac{\gamma m}{\bar{\gamma}}} \Gamma\left(\mu_1, \frac{\psi_1}{(\gamma+1)^{\frac{\alpha_1}{\beta}}}\right) d\gamma. \end{aligned} \tag{4.26}$$

We apply series representation of the incomplete Gamma function in [68, eq. (8.354.2)] and solve the integral in (4.26) as

$$\bar{P}_{D\text{Nak}}^{\text{id}} = \tag{4.27}$$
$$1 - \epsilon \sum_{n=0}^{\infty} \sum_{j=0}^{\infty} \frac{(-1)^n (-1)^j}{n!(\mu_1+n)} \psi_1^{\mu_1+n} \binom{s}{j} \sum_{k=0}^{m+j-1} \binom{m+j-1}{k} (-1)^k \Gamma\left(m-k, \frac{m}{\bar{\gamma}}\right),$$

where ϵ is given as

$$\epsilon = \frac{\left(\frac{m}{\bar{\gamma}}\right)^m}{\Gamma(\mu_1)\Gamma(m)}. \tag{4.28}$$

A step-by-step derivation of the $\bar{P}_{D\text{Nak}}^{\text{id}}$ is presented in Appendix B.3.

4.7.2 P_D^{hi} for Hardware-impaired System Model

The average detection probability for non-ideal transceiver electronics over Nakagami-m fading channel is calculated in this subsection. We apply the same strategy to evaluate the average detection probability for non-ideal transceiver electronics as in the previous

subsection for $\bar{P}_{D\text{Nak}}^{\text{id}}$. Hence, $\bar{P}_{D\text{Nak}}^{\text{hi}}$ is integrated as

$$\begin{aligned}\bar{P}_{D\text{Nak}}^{\text{hi}} &= \int_0^{\infty} P_D^{\text{hi}} f_{Nak}(\gamma) d\gamma \\ &= 1 - \epsilon \sum_{n=0}^{\infty} \sum_{j=0}^{\infty} \frac{(-1)^n (-1)^j \psi_1^{\mu_1+n}}{n!\,(\mu_1+n)} \left(\frac{2}{\beta}(\mu_1+n)\, j\right) \\ &\quad \times \frac{\exp\left(\frac{m}{\bar{\gamma}(1+\kappa^2)}\right)}{(1+\kappa^2)^{m+j}} \sum_{t=0}^{j+m-1} \binom{j+m-1}{t} (-1)^t \\ &\quad \times \Gamma\left(m-t, \frac{m}{(1+\kappa^2)\bar{\gamma}}\right) \left(\frac{m}{(1+\kappa^2)\bar{\gamma}}\right)^{t-m}. \end{aligned} \tag{4.29}$$

A full derivation of the $\bar{P}_{D\text{Nak}}^{\text{hi}}$ is shown in Appendix B.4.

To obtain some insights on the performance of improved ED during low average SNR regime, we perform asymptotic analysis on detection probability when average SNR approaches to 0.

4.7.3 Asymptotic Analysis at Low $\bar{\gamma}$ Values

Asymptotic analysis at low SNR values provides an important information on detector's performance that represents the worst case scenario. We take a limit of the $\bar{P}_{D\text{Nak}}^{\text{id}}$ given in (4.27) when that approaches to 0. When we expand j terms in (4.27) at $\bar{\gamma} \to 0$, all terms approaches to zero except for $j = 0$ term. Hence, the asymptotic detection probability over Nakagami-m fading channel for ideal transceiver hardware is given as

$$\lim_{\bar{\gamma}\to 0} \bar{P}_{D\text{Nak}}^{\text{id}} = 1 - \frac{m^m}{\Gamma(\mu_1)} \sum_{n=0}^{\infty} \frac{(-1)^n}{n!(\mu_1+n)} \psi_1^{\mu_1+n}. \tag{4.30}$$

We could not present asymptotic analysis for detection probability for non-ideal transceiver electronics due to the mathematical complexity of the expression in (4.29) at low $\bar{\gamma}$.

4.8 Diversity Reception for Improved ED in Spectrum Sensing

Diversity reception for the conventional ED enhances spectrum sensing performance to combat shadowing and fading effects in wireless communication [70]. A square-law combining device performs square and integrate function to obtain test statistics for the conventional ED [55]. Similarly, a square-law selection device selects the highest powered antenna branch signal to apply hypotheses tests. Inspired by diversity reception in conventional ED, we propose p order law combining (pLC) and p order law selection (pLS) diversity techniques given M antenna branches as shown in Fig. 4.2. This section inves-

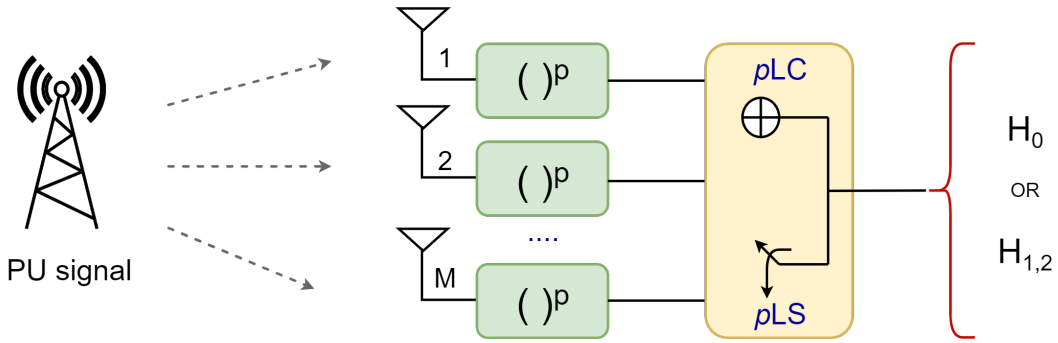

Figure 4.2. The pLC and pLS diversity reception schemes for the improved ED.

tigates false alarm and detection probabilities performance analysis for the pLC and the pLS diversity reception devices over non-fading and fading channels.

4.8.1 Diversity Receivers over AWGN Channels

4.8.1.1 False Alarm and Detection Probabilities for the pLC technique

We consider that M antenna branches with improved EDs are combined to yield D_{pLC} test statistics. As it was previously mentioned, each sample of Y_i is a Weibull distributed RV. Therefore, additional summation of M branches is $\alpha - \mu$ distributed RV defined as

$$D_{pLC} = \sum_{j=1}^{N} \sum_{i=1}^{M} Y_{ji}. \tag{4.31}$$

For the pLC diversity technique, one need to perform M times more summations of Weibull RVs. The probability of false alarm given the pLC diversity technique over i.i.d. AWGN channels are evaluated similarly to (4.19). The only difference would be in changing N to $M \times N$. Therefore, P_{F_c} is evaluated by

$$P_{F_c} = \frac{1}{\Gamma(\mu_0)} \Gamma\left(\mu_0, \left(\frac{\gamma_{th}\Gamma(\mu_0 + \frac{1}{\alpha_0})}{\Gamma(\mu_0) M N \Gamma(1+\frac{1}{\beta})}\right)^{\alpha_0}\right). \tag{4.32}$$

By applying the identical strategy as for evaluating P_{F_c}, detection probability for the pLC diversity technique over i.i.d. AWGN channels are calculated both for ideal/non-ideal transceiver hardware as

$$P_{D_c}^{\text{id/hi}} = \frac{1}{\Gamma(\mu_1)} \Gamma\left(\mu_1, \left(\frac{\gamma_{th}\Gamma(\mu_1 + \frac{1}{\alpha_1})}{(\frac{\gamma}{\kappa^2\gamma+1})^{\frac{\alpha_1}{\beta}} \Gamma(\mu_1) M N \Gamma(1+\frac{1}{\beta})}\right)^{\alpha_1}\right), \tag{4.33}$$

where $\kappa = 0$ is chosen for the ideal system model.

4.8.1.2 False Alarm and Detection Probabilities for the pLS technique

Inspired by [55], test statistics for the pLS diversity technique is calculated by choosing the highest antenna branch power as

$$D_{pLS} = \max(\Lambda_1, \Lambda_2, \cdots, \Lambda_M), \tag{4.34}$$

where Λ_i stands for the improved ED test statistics given for each antenna branch i.

Diversity receiver's false alarm and detection probabilities over AWGN channels are denoted as P_{F_s} and P_{D_s}, respectively. By employing P_F in (4.19), we evaluate P_{F_s} as

$$P_{F_s} = 1 - (1 - P_F)^M = 1 - \left(1 - \frac{\Gamma(\mu_0, \psi_0)}{\Gamma(\mu_0)}\right)^M. \tag{4.35}$$

Next, we formualte the detection probability for the pLS diversity receiver $P_s^{\text{id/hi}}$ over AWGN channel for either ideal or non-ideal trasceiver hardware by using (4.20)

and (4.22) as

$$\begin{aligned} P_{D_s}^{\text{id/hi}} &= 1 - \prod_{i=1}^{M} (1 - P_{D_i}^{\text{id/hi}}) \\ &= 1 - \prod_{i=1}^{M} \left(1 - \frac{1}{\Gamma(\mu_1)} \Gamma \left(\mu_1, \frac{\psi_1}{(\frac{\gamma}{\gamma\kappa^2+1} + 1)^{\frac{\alpha_1}{\beta}}} \right) \right), \end{aligned} \tag{4.36}$$

where $\kappa = 0$ for the ideal system model.

4.8.2 Improved ED with Diversity Reception over Fading Channels

4.8.2.1 Average Detection Probability for the pLC Technique

The average detection probability for the pLC diversity technique for M antenna branches over i.i.d. Rayleigh fading channels is equivalent to the average detection probability of non-diversity improved ED over Nakagami-m fading channel given in (4.27) and (4.29). The only difference is that m parameter is substituted with M and $\bar{\gamma}$ is substituted with $M\bar{\gamma}$ and corresponding average detection equations are provided below for both ideal and non-ideal transceiver electronics. The average detection probability for the pLC diversity technique considering ideal transceiver electronics is given as

$$\begin{aligned} &\bar{P}_{D_{c,Ray}}^{\text{id}} = \\ &1 - \epsilon \sum_{n=0}^{\infty} \sum_{j=0}^{\infty} \frac{(-1)^n (-1)^j}{n!(\mu_1 + n)} \psi_1^{\mu_1 + n} \binom{s}{j} \sum_{k=0}^{M+j-1} \binom{M+j-1}{k} (-1)^k \Gamma \left(M - k, \frac{1}{\bar{\gamma}} \right). \end{aligned} \tag{4.37}$$

Similarly, the average detection probability for the pLC diversity technique by taking into account non-ideal transceiver electronics is given as

$$\begin{aligned}\bar{P}^{\text{hi}}_{D_{c,Ray}} = 1 - \epsilon \sum_{n=0}^{\infty}\sum_{j=0}^{\infty} \frac{(-1)^n (-1)^j \psi_1^{\mu_1+n}}{n!\,(\mu_1+n)} \left(\frac{2}{\beta}(\mu_1+n)\,j\right) \\ \times \frac{\exp\left(\frac{1}{\bar{\gamma}(1+\kappa^2)}\right)}{(1+\kappa^2)^{M+j}} \sum_{t=0}^{j+m-1} \binom{j+m-1}{t} (-1)^t \\ \times \Gamma\left(M-t, \frac{1}{(1+\kappa^2)\bar{\gamma}}\right) \left(\frac{1}{(1+\kappa^2)\bar{\gamma}}\right)^{t-M}.\end{aligned} \tag{4.38}$$

4.8.2.2 Average Detection Probability for the pLS Technique

The general formula for the average detection probability over Nakagami-m fading channel by using the pLS diversity technique with M antennas branches is given as

$$\bar{P}^{\text{id/hi}}_{D_{s,Nak}} = 1 - \prod_{i=1}^{M} (1 - \bar{P}^{\text{id/hi}}_{D_i}), \tag{4.39}$$

where average detection probabilities for ideal/non-ideal system models over Nakagami-m fading channel are given in (4.27) and (4.29), respectively. More precisely, the average detection probability for the ideal system model by using (4.27) is presented as

$$\begin{aligned}&\bar{P}^{\text{id}}_{D_{s,Nak}} = \\ &1 - \prod_{i=1}^{M} \left(\epsilon \sum_{n=0}^{\infty}\sum_{j=0}^{\infty} \frac{(-1)^n(-1)^j}{n!(\mu_1+n)} \psi_1^{\mu_1+n} \binom{s}{j} \sum_{k=0}^{M+j-1} \binom{M+j-1}{k} (-1)^k \Gamma(M-k, \frac{1}{\bar{\gamma}})\right).\end{aligned} \tag{4.40}$$

Similarly, the average detection probability for non-ideal transceiver electronics could be represented by using (4.29) as

$$\bar{P}^{\text{hi}}_{D_{s,Nak}} = 1 - \prod_{i=1}^{M} \epsilon \sum_{n=0}^{\infty} \sum_{j=0}^{\infty} \frac{(-1)^n (-1)^j \psi_1^{\mu_1+n}}{n!\,(\mu_1+n)} \left(\frac{2}{\beta}(\mu_1+n)\, j\right) \frac{\exp\left(\frac{1}{\bar{\gamma}(1+\kappa^2)}\right)}{(1+\kappa^2)^{M+j}} \times \sum_{t=0}^{j+M-1} \binom{j+M-1}{t} (-1)^t \Gamma\left(M-t, \frac{1}{(1+\kappa^2)\bar{\gamma}}\right) \left(\frac{1}{(1+\kappa^2)\bar{\gamma}}\right)^{t-M}. \tag{4.41}$$

4.9 Numerical Evaluation

This section verifies the analytical expressions provided in Sections 4.6, 4.7, and 4.8 through Monte-Carlo simulations. We emphasize on the effect of transceiver distortion noise on the detection accuracy of the improved ED by making the AUC, ROC, and total error rate performance analysis for both non-fading and fading channel environment. Moreover, we verify performance gains while implementing the pLS and pLC diversity receptions for the improved ED. The closed-form expression of the average detection probability for ideal transceiver hardware over Nakagami-m fading channel is shown in (4.27). This expression is represented as a double semi-infinite summation terms. We verify the conversion rate of the (4.27) by introducing $\bar{P}^{\text{id,appr}}_{DNak}$ that ranges between $j = [0:a]$ and $n = [0:b)$ where $a > 0$ and $b > 0$. In Fig. 4.3, we plot logarithmic error comparison plot between exact detection probability in (4.27) and approximated detection probability, $\bar{P}^{\text{id,appr}}_{DNak}$ with $a = 40$ and $b = 50$. In Fig. 4.3, we denote x-axis to represent the internal summation size of $\bar{P}^{\text{id,appr}}_{DNak}$ that ranges between $j = [0:40]$. In addition, y-axis is used for external summation size that ranges between 0 and 50. An average detection error plot is calculated by taking absolute logarithm of the absolute difference between exact and approximated detection probabilities as $\Delta = \log_{10}|\bar{P}^{\text{id,appr}}_{DNak} - \bar{P}^{\text{id,ex}}_{DNak}|$. In Fig. 4.3, $z-axis$ represents logarithmic error plot of the detection probability. Based on this figure, we notice that $\bar{P}^{\text{id,appr}}_{DNak}$ converges relatively quickly even at $j = 30$. Internal loop with j index has more influence on the convergence sum rather than external loop with

index n. For example, at $n = 41$ and $j = 19$ average detection error, Δ, is as low as $\Delta = 2.29 \times 10^{-4}$. Thus, we conclude that average detection probability is the fast converging function. Another performance analysis metric is total error rate analysis. It is evaluated as a sum of false alarm and miss detection probabilities [71, eq. (4.1)]. In Fig. 4.4, we plot a total error rate versus SNR over AWGN channel for a single and diversity reception improved EDs, when diversity order is $p = 6$, number of signal samples is $N = 5$, and number of diversity branches is $M = 20$, detection threshold is $\gamma_{th} = 5; 16$ dB and $P_F = 0.1$. In Table 4.1, we present total error rate curves for diversity and non-diversity improved EDs at $\gamma = -2$ dB, $\gamma_{th} = 5$ dB. Total error rate is 4 times less for pLS and 6 times less for pLC diversity detector. When increasing the threshold to 15 dB, the pLS and pLC outperform the non-diversity receivers in terms of the total error rate to 2 and 10 times, correspondingly. Based on the total error rate analysis pLS diversity scheme shows better performance than pLC one.

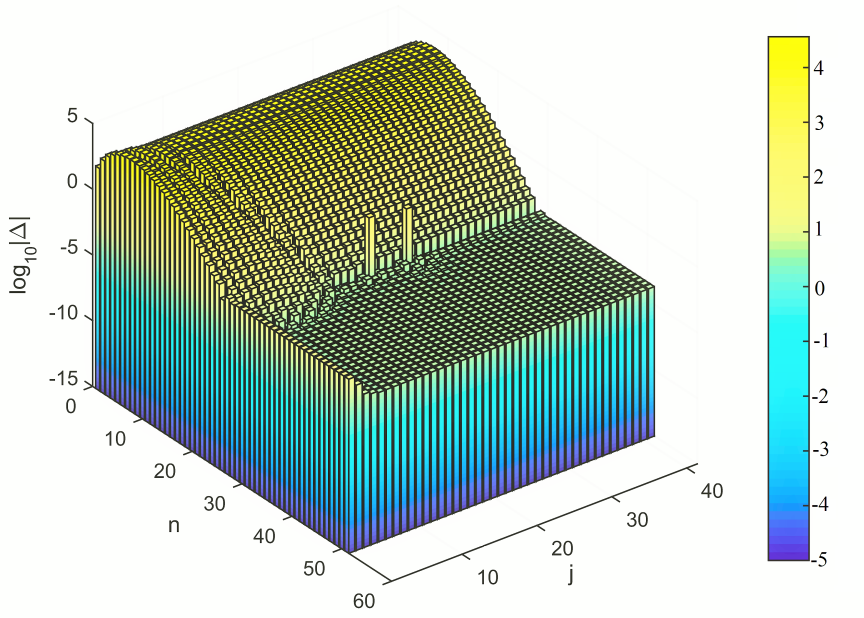

Figure 4.3. Error plot for $\bar{P}_{DNak}^{\text{id,appr}}$ when $j = [0:40]$ and $n = [0:50]$, $m = 2, p = 10, \bar{\gamma} = 0.1$.

The ROC analysis given AWGN channel for the improved ED of the order $p = 10$, $\kappa = 0.5$, and $N = 10$ is given in Fig. 4.5. We plot the ROC curves for both ideal and non-ideal improved EDs by changing SNR as $\gamma = -20; -5; 5; 10$ dB. There is a

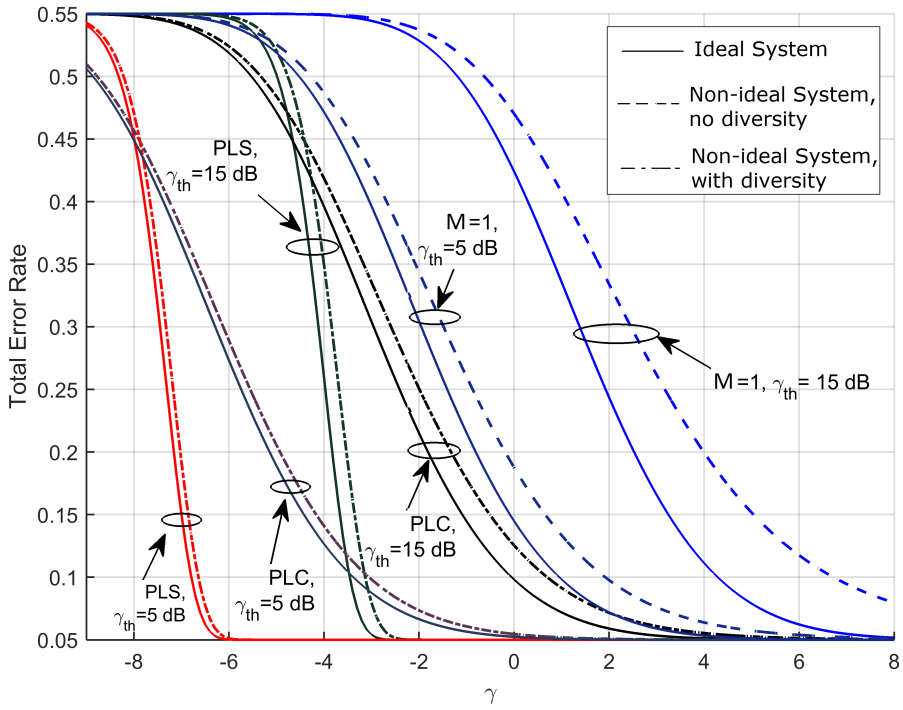

Figure 4.4. Total error rate for diversity receivers and non-diversity receiver versus SNR over AWGN channels.

Table 4.1. Total error rate for non-diversity and diversity receivers at $\gamma = -2$ dB.

Total error rate	$\gamma_{th} = 5$ **dB**	γ_{th}**=15 dB**
No diversity, $\kappa = 0$	0.3	0.5350
No diversity, $\kappa = 0.4$	0.35	0.5411
pLS, $\kappa = 0$	0.05	0.05
pLS, $\kappa = 0.4$	0.0501	0.0502
pLC, $\kappa = 0$	0.0713	0.2405
pLC, $\kappa = 0.4$	0.0794	0.2755

higher influence of distortion noise at high SNR value on the ROC performance due to proportionality of distortion noise and transmit power. It was noted that at low SNR values AWGN noise dominates over residual distortion noise.

In Fig. 4.6, we analyze diversity reception in the improved EDs with $\bar{\gamma} = 5$ dB, $N = 10$, $p = 10$, $\kappa = 0.4$, channel fading parameter $m = 1$, and number of diversity branches $M = 5$. Based on this figure, the pLC scheme performs better than the pLS one. Although, the pLC suffers more from distortion noise than the pLS diversity technique.

In Fig. 4.7, we analyze the detection accuracy of the improved ED by performing the

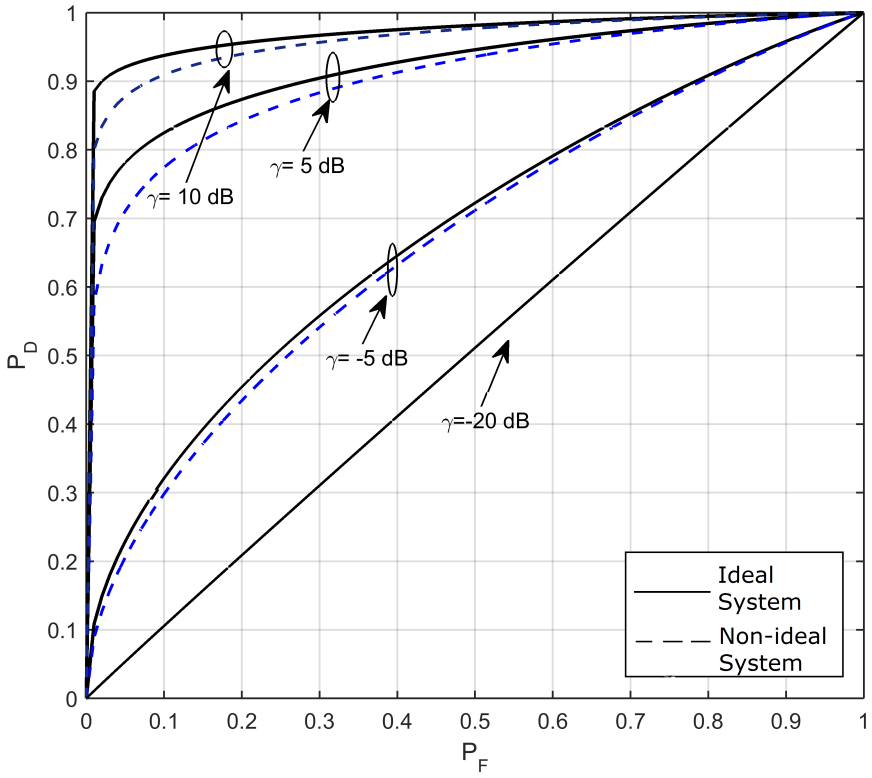

Figure 4.5. The ROC curves at varying γ values over AWGN channel.

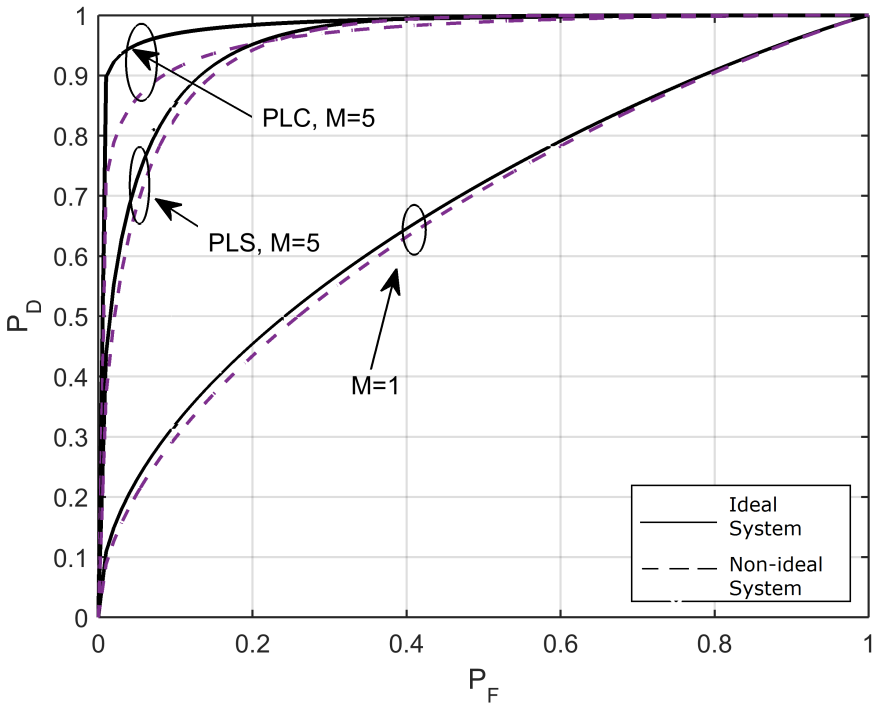

Figure 4.6. The ROC curves for diversity and non-diversity receivers over Rayleigh fading channels.

AUC analysis. The average AUC versus average SNR for $p = 4$, $p = 6$, and $p = 10$ given two sets of signal samples, $N = 5; 10$, at ideal transceiver hardware ($\kappa = 0$) and non-ideal transceiver hardware ($\kappa = 0.3$) over AWGN channel are analyzed in Fig. 4.7. According to this figure, it was clear that the detector with a higher p order results in higher AUC performance. For instance, the best AUC performance is demonstrated at $p = 10$, and the worst AUC performance is shown at $p = 4$. A PU signal accuracy has been improved not only by order of the improved ED but also with the higher number of signal samples.

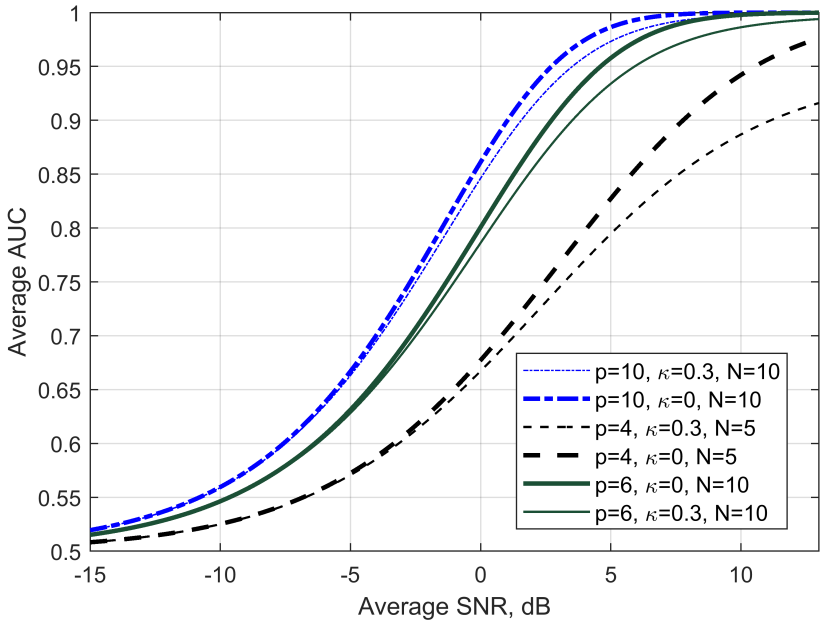

Figure 4.7. The average AUC versus average SNR for improved ED with $p = 4; 6; 10$ over AWGN channel.

4.10 Chapter Summary

In this chapter, we have investigated the influence of transceiver distortion noise on the detection accuracy of a PU signal. To the best knowledge of authors, a non-ideal improved ED with N signal samples was first studied in the technical literature by our work. Diversity reception for the improved ED was proposed to mitigate the negative impact

of distortion noise. We presented a novel method of calculating improved ED by using $\alpha - \mu$ distribution. Moreover, we have presented closed-form expressions for the detection and false alarm probabilities of improved ED over AWGN and Nakagami-m fading channels given ideal and non-ideal transceiver hardware. The AUC analysis over AWGN and fading channel have been analyzed as well. Based on numerical simulation results, we discover that the pLC and the pLS diversity techniques considerably improves the detection accuracy of the improved ED. A single reception detector was the most influenced by the distortion noise, and the pLS reception detector was the least affected. Moreover, total error rate performance is improved, and the detrimental effect of distortion noise is reduced when diversity reception was applied.

Chapter 5

Device-to-Device Assisted Millimeter Wave Network with Residual Hardware Impairments, imperfect CSI, and Interference Constraints

A D2D communication, mmWave frequency range, and massive MIMO antennas are considered as potential technologies for 5G networks. A high transmission rate, security, privacy, and low latency are leading advantages of the D2D assisted mmWave network that enables to free the resources of the base station. In this chapter, we develop a tractable analytical framework that studies overlay D2D assisted 5G mmWave network under practical transceiver constraints such as aggregate transceiver distortion noise, interference noise from neighboring transmissions, and imperfect CSI. The performance of the proposed system model is analyzed for the outage probability and ergodic capacity with it's upper and lower bounds, and corresponding closed-form expressions are derived as well. Monte Carlo simulations verify all the analytical expressions. This chapter was written based on the author's publications in [72] and [73].

5.1 Introduction

MmWave communication empowers high rate smart devices to communicate with each other at a short distance range. It is expected that by 2022 smart devices share connected to a mobile network will be three-quarters of all devices [74]. D2D network operating overlay/underlay to mmWave network, save the power consumption of the base station, and reduce the operational cost. Due to the mmWave size of antennas in mmWave frequency range, it is possible to install massive MIMO antennas at the base station and MIMO antennas even at handheld devices.

5.2 Related Work

The authors in [75] summarize contemporary techniques, trends, and limitations of the 5G assisted D2D network. The work in [76] analyzed interference management techniques and optimal power allocation for the underlay D2D network given a macro-micro cell network. The authors considered imperfect CSI and claimed a crucial impact of channel estimation error on the coverage probability performance at high SNR values. Interference alignment scheme for multi-cell and X-channel networks were studied by authors in [77] and [78]. The authors in [79] studied transmission capacity analysis of the D2D network operating underlay/overlay to mmWave network by using relay nodes, where D2D, cellular, and relay nodes that are modelled as Poisson point process over Rayleigh fading channel. All the work, as mentioned above, does not consider transceiver distortion noise in their system models, which is far from realistic settings. The major motivation of this work is that practical transceivers are not ideal, and compensation algorithms presented in [9] do not mitigate residual distortion noise. In practice, CSI estimation faces mismatch in estimation that adds CSI estimation error to the system. We apply the additive Gaussian distortion noise model described in Section 2.3.2 for mmWave communication. Interference cancellation in the D2D underlaying mmWave network was studied in [80]. The authors performed an ergodic achievable sum rate analysis for the proposed system

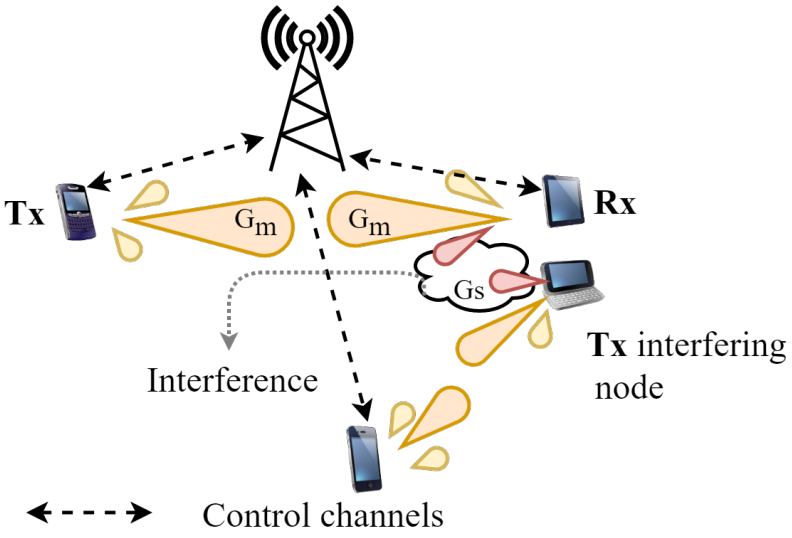

Figure 5.1. System model for the analog beamformed D2D assisted communication network with interfering nodes.

model and observed a logarithmic increase in the ergodic achievable rate as a number of antennas in base station increase.

5.3 Contributions

- We present an analytical framework for overlay D2D assisted mmWave systems that investigate compound system constraints such as residual distortion noise, imperfect CSI, and i.n.i.d. interference noise on the system performance;
- We evaluate closed-form expressions for the outage probability, ergodic capacity, and lower/upper bounds for ergodic capacity considering system constraints. These equations empower careful investigation of every constraint separately from each other;
- Monte Carlo simulation results enable verification of analytical equations and analysis of system constraints.

5.4 System and Network Model

Let us consider a D2D network with N smart devices overlaid upon mmWave network. Network resources are managed between cellular and device nodes via base station control channels. In this figure, we present only a couple of paired D2D nodes that are depicted for notation simplicity. We consider N paired device nodes in our analytical framework. As it could be be seen from Fig. 5.1, a Tx D2D node communicates to a Rx D2D node. However, concurrently transmiting neighbouring node's side/back lobes create interference to the reference Rx node. We assume that all nodes operate on steerable directional antennas. The sectored antenna array pattern is assumed between device nodes for mathematical tractability as in [7, 81, 82]. That is, antenna gain is a constant value between chosen mainlobe or side/back lobe sector, such as G_{m} denotes main lobe antenna gain and G_{s} represents side/back lobe antenna gain as

$$G(\theta) = \begin{cases} G_{\mathrm{m}}, & |\theta| \leq \theta_b, \\ G_{\mathrm{s}}, & \text{otherwise}, \end{cases} \tag{5.1}$$

where θ is a boresight angle and θ_b is an antenna beamwidth. We consider that the D2D network operates overlay to the primary network, which assumes orthogonal frequency/time resource sharing between primary and secondary networks. An overlay paradigm ensures interference-free communication with cellular user nodes, as discussed in [79, 83, 84]. MmWave base station arbitrates coordination between D2D nodes and other cellular user nodes, such that D2D users are aligned to the main lobe gain to eliminate the interference from neighboring nodes. Inspired by authors in [81], [82], and [85], we propose to apply Nakagami-m fading channel to model small-scale fading in mmWave communication. A major advantage of Nakagami-m fading channel is its ability to model both line-of-sight (LOS) and non-line-of sight (NLOS) component of mmWave communication, which is a vital assumption. Moreover, Nakagami-m distribution closely approximates Rician (Nakagami-n) distribution with the following mapping of the fading

parameter m, $m = \frac{(1+K)^2}{1+2K}$, where $K \geq 1$ for a given K factor. Rician K factor indicates the ratio of the LOS component to the average power scattered components [86, pp. 23-24]. We avoid using purely NLOS channel modelling like Rayleigh fading channel. Besides, Nakagami-m distribution is analytically tractable that simplifies the derivation of complex formulas. We propose that independent interfering node channels may have fixed LOS or NLOS fading parameters as $m \in \{m_L, m_N\}$, where m_L stands for LOS fading parameter and m_N for NLOS fading parameter, respectively. Similarly, we denote a path loss exponent value to LOS or NLOS scenario by setting $\alpha_0 \in \{\alpha_L, \alpha_N\}$. Since interfering nodes are located at different distances and transmit with various powers from the reference Rx device node, we assume i.n.i.d. channel gains for interfering nodes. For mathematical tractability, we assume a fixed geometry for all nodes. Furthermore, we consider the imperfect CSI estimation in the proposed system model. According to [87], minimum mean square error criteria is utilized for estimation of actual channel $h = \sqrt{1-\lambda}\hat{h} + \sqrt{\lambda}\tilde{h}$, where $\hat{h}$ is estimated channel, $\tilde{h}$ is channel estimation error, which is modelled as $\tilde{h} \sim \mathcal{CN}(0, \sigma_e^2)$ with estimation error variance $0 < \lambda < 1$, where $\lambda = 0$ stands for an ideal CSI estimation. Hence, the received signal of the reference Rx device node under residual distortion noise, imperfect CSI, and N interference noise is formulated as

$$y = \sqrt{\zeta}(\sqrt{1-\lambda}\hat{h} + \sqrt{\lambda}\tilde{h})(s+\mu) + \sum_{i=1}^{N} \sqrt{\zeta_i^I} g_i(t_i + \mu_i) + w, \tag{5.2}$$

where $\hat{h}$ and g_i are Nakagami-m fading channels with β and β_i are scale parameters, m and m_i are fading parameters of the mmWave channel. We denote s as a transmit signal with average power $P = \mathbb{E}\{|s|^2\}$. Similarly, t_i is interference node's signal power with average power $I_i = \mathbb{E}\{|t_i|^2\}$. We assign $\zeta = G_{\mathrm{m}}^2 L_0^{-\alpha_0}$ and $\zeta_i^I = G_{\mathrm{s}}^2 L_i^{\alpha_i}$ for simple representation, where G_{m} and G_{s} are analog antenna gains, L_0 and L_i are distances, α_0 and α_i are path loss exponents between the main and interfering nodes, correspondingly. Moreover, additive Gaussian distortion noise model is used to model aggregate residual transceiver noise as $\mu \sim \mathcal{CN}(0, \kappa^2 P)$, where κ is a distortion level which is measured by

EVM, described in Section 2.3.2.1. More details on Gaussian distortion model in given in Section 2.3.2.

The instantaneous signal-to-noise-distortion-interference ratio (SNDIR), γ, of the D2D network operating overlay to mmWave network which is constrained by compound system imperfections such as residual transceiver distortion noise, imperfect CSI, and interference noise is given by

$$\gamma = \frac{P\zeta(1-\lambda)|\hat{h}|^2}{P\zeta\kappa^2(1-\lambda)|\hat{h}|^2 + P\zeta\lambda\sigma_e^2(1+\kappa^2) + \sum_{i=1}^{N} I_i(1+\kappa_i^2)|g_i|^2\zeta_i^I + \sigma^2}, \tag{5.3}$$

where channel gains $|\hat{h}|^2$ and $|g_i|^2$ are i.n.i.d. Gamma RVs and we make following substitutions: $\Delta = P\zeta\lambda\sigma_e^2(1+\kappa^2)+\sigma^2$, $a = \frac{P\zeta(1-\lambda)}{\Delta}$, $b = \frac{P\zeta\kappa^2(1-\lambda)}{\Delta}$, $X = |\hat{h}|^2$, and Z represents summation of N i.n.i.d. Gamma RVs as $Y = \sum_{i=1}^{M} \frac{I_i}{\Delta}(1+\kappa^2)|g_i|^2\zeta_i^I$. As the result, the comprehensive SNDIR is represented as $\gamma = \dfrac{aX}{1+Y+bX}$.

5.5 Outage Probability Analysis

This section calculates the outage probability of the proposed system model described in Section 5.4. The outage probability is computed as probability of SNDIR that falls below a certain threshold, $\gamma_{th} = 2^{\Delta} - 1$, as

$$P_{\text{out}}(\gamma_{th}) = \Pr(\gamma \leq \gamma_{th}) = \Pr\left(\frac{aX}{1+Y+bX} \leq \gamma_{th}\right), \tag{5.4}$$

where Δ stands for a transmission rate. To compute the outage probability, we need to evaluate the CDF of the SNDIR, which requires the PDF of summation of N i.n.i.d. Gamma variates. The Lemma 3 below gives an insight on the PDF of a sum of M Gamma variates.

Lemma 3 *Consider a finite set of $\{X_i\}_{i=1}^{M}$ i.n.i.d. Gamma RVs with m_i fading and $\tau_i\beta_i$ scale parameters with $\tau_i > 0$. Then, the PDF of the sum of M i.n.i.d. Gamma variates,*

$Z = \sum_{i=0}^{M} \tau_i X_i$, may be given by using a single gamma-series given in [88, Theorem 1]

$$f_Z(z) = \Phi \sum_{k=0}^{\infty} \frac{\delta_k z^{\rho+k-1} e^{-\frac{z}{\beta_0}}}{\Gamma(\rho+k)\beta_0^{\rho+k}}, \tag{5.5}$$

where $z > 0$ or zero otherwise. Recursive parameter δ_k is assessed as

$$\delta_{k+1} = \frac{1}{k+1} \sum_{i=1}^{k+1} i\theta_i \delta_{k+1-i}, \tag{5.6}$$

where $k \geq 0$, $\delta_0 = 1$, and θ_n is determined by $\theta_i = \frac{\sum_{j=1}^{N} m_j \left(1-\frac{\beta_0}{\tau_j \beta_j}\right)^i}{i}$, where β_0 is a minimum value between a set of scaled $\tau_i \beta_i$ values, $\beta_0 = \min[\tau_1\beta_1, \tau_2\beta_2, \cdots, \tau_M\beta_M]$; ρ represents a summation of fading parameters as $\rho = \sum_{i=1}^{M} m_i$. Moreover, Φ is a product of ratios of minimum scale parameter to other scale parameters β_i raised to the power m_i

$$\Phi = \prod_{i=1}^{M} \left(\frac{\beta_0}{\tau_i \beta_i}\right)^{m_i}. \tag{5.7}$$

Proof: The proof is similar to [88, Theorem 1] with multiplication of scale fading parameter β_i to a positive constant τ_i.

■

The authors in [89] present approximation for the PDF of summation of M i.n.i.d. Gamma RVs by applying saddlepoint approximations as

$$\tilde{f}_Z(z) = \frac{\Phi z^{\rho-1} \exp(-\frac{z(1-c)}{\beta_0})}{\Gamma(\rho)\beta_0^{\rho}}, \tag{5.8}$$

where $c = \max_i (1 - \frac{\beta_0}{\tau_i \beta_i})$.

Proposition 1 *Let us denote X to be a non-negative Gamma RV, a and b are positive real numbers, and Z denotes summation of N i.n.i.d. Gamma RVs. The outage probability of the reference D2D receiver in the presence of N interferences, imperfect CSI, and residual*

distortion noise is estimated by

$$P_{out}(\gamma_{th}) = \frac{\Phi}{\Gamma(m)} \sum_{n=0}^{\infty} \frac{(-1)^n}{n!(m+n)} \sum_{k=0}^{\infty} \frac{\delta_{k+1}}{\Gamma(\rho+k)} \left(\frac{1}{\beta}\right)^{m+n} \times \sum_{t=0}^{m+n} \binom{m+n}{t} \phi_1^{m+n-t} \beta_1^t \Gamma[k+\rho+t] \phi_2^t, \tag{5.9}$$

where $\phi_1 = \frac{\gamma_{th}}{a-\gamma_{th}b}$ *and* $\phi_2 = \frac{\gamma_{th}}{a-\gamma_{th}b}$ *for* $\gamma_{th} < \frac{a}{b}$ *and* $P_{out} = 1$ *for* $\gamma_{th} \geq \frac{a}{b}$.

Proof: The proof is relegated into Appendix C.1. ■

5.5.1 Convergence Analysis for the Outage Probability

This section is devoted to providing a convergence analysis of the derived outage probability formula provided in (5.9). We apply the necessary condition for series convergence and the Cauchy ratio tests to verify the convergence of these semi-infinite series. Since constant values do not contribute to the series convergence, we neglect them during the convergence analysis.

5.6 Necessary condition for the series convergence

According to the necessary condition for convergence, if $\sum a_i$ converges, then $\lim_{i\to\infty} a_i = 0$. The outage probability in (5.9) contains two semi-infinite summation with n and k terms and one summation with t terms bounded by n. In our analysis, we consider that n and k terms are independent of each other.

5.6.1 $P_{out}(\gamma_{th})$ when k is varied and n is fixed

Next, by using the asymptotic expansion of a ratio of gamma functions given in [90] and by fixing the n terms, we evaluate the convergence of the outage probability when $k \to \infty$

as follows

$$\lim_{k\to\infty} P_{out}(\gamma_{th}) \approx \lim_{k\to\infty} \delta_{k+1}\frac{\Gamma(k+\rho+t)}{\Gamma(k+\rho)} \approx \delta_{k+1}k^t\left(1+\frac{t(2\rho+t-1)}{2k}\right) \\ = (k^t + \frac{1}{2}k^{t-1}t(2\rho+t-1))\delta_{k+1}. \tag{5.10}$$

Moreover, by the considering the fact that δ_{k+1} is a decaying function, we represent δ_{k+1} as follows

$$\delta_{k+1} \approx \frac{1}{k+1}\delta_k \approx \frac{1}{k+1}\frac{1}{k}\delta_{k-1} \approx \frac{1}{(k+1)!}. \tag{5.11}$$

Hence, $\lim_{k\to\infty} \delta_{k+1}\frac{\Gamma(k+\rho+t)}{\Gamma(k+\rho)} \approx \delta_{k+1}k^t(1+\frac{t(2\rho+t-1)}{2k}) \approx \lim_{k\approx\infty}\frac{k^t}{(k+1)!} = 0.$

So, $\lim_{k\to\infty} P_{out}(\gamma_{th}) \approx 0.$

5.6.2 $P_{out}(\gamma_{th})$ when n is varied and k is fixed

Furthermore, we evaluate the $P_{out}(\gamma_{th})$ given in (5.9) when $n \to \infty$ and k values are fixed. Moreover, if the limit taken from absolute value of the series $\lim_{i\to\infty}|a_i|$ converges, then a_i also converges. We use this property in our analysis as well.

$$\lim_{n\to\infty} P_{out}(\gamma_{th}) \approx \lim_{n\to\infty} \frac{1}{n!}\frac{1}{(m+n)}\left(\frac{1}{\beta}\right)^{m+n}\frac{(m+n)!}{t!(m+n-t)!}\phi_1^{m+n-t}. \tag{5.12}$$

In this case, we have to consider the third semi-infinite summation with t terms, more precisely, we consider the cases 1). $t = m+n$ and 2). $t = \frac{m+n}{2}$ below.

5.6.2.1 Limit Calculation when $t = m+n$

First, we consider the case when $t = m+n$ for the expression given below

$$\lim_{n\to\infty}\frac{1}{n!}\frac{1}{(m+n)}(\frac{1}{\beta})^{m+n}\beta_1^{m+n}\Gamma(k+\rho+m+n)\phi_2^{m+n} \\ = \lim_{n\to\infty}\frac{1}{(m+n)}\left(\frac{\beta_1\phi_2}{\beta}\right)^{m+n}\frac{\Gamma(k+\rho+m+n)}{\Gamma(n+1)} \\ \approx \lim_{n\to\infty}\frac{1}{(m+n)}\left(\frac{\beta_1\phi_2}{\beta}\right)^{m+n} n^{k+\rho+m-1}. \tag{5.13}$$

When $\left(\frac{\beta_1\phi_2}{\beta}\right) < 1$, then $\lim_{n\to\infty} \frac{n^{k+\rho+m-2}}{(\frac{\beta}{\beta_1\phi_2})^{m+n}} \approx 0$. Therefore, $\lim_{n\to\infty} P_{out} \approx 0$. Next, we evaluate the case when $t = \frac{m+n}{2}$.

5.6.2.2 Limit Calculation when $t = \frac{m+n}{2}$

$$\begin{aligned}
&\lim_{n\to\infty} \frac{1}{n!}\frac{1}{(m+n)}(\frac{1}{\beta})^{m+n}\frac{(m+n)!}{2(\frac{m+n}{2})\phi_1^{\frac{m+n}{2}}}\beta_1^{\frac{m+n}{2}}\phi_2^{\frac{m+n}{2}}\Gamma(k+\rho+\frac{m+n}{2}) \\
&= \lim_{n\to\infty} n^m \frac{1}{(m+n)}\left(\frac{1}{\beta}\right)^{m+n}(\phi_1\beta_1\phi_2)^{\frac{m+n}{2}}\left(\frac{n}{2}\right)^{k+\rho-1} \\
&= \lim_{n\to\infty} \left(\frac{1}{\beta}\right)^{\frac{m+n}{2}} \frac{\beta_1\phi_1\phi_2}{\beta}^{\frac{m+n}{2}}\left(\frac{n}{2}\right)^{k+\rho+m-2} \\
&= \lim_{n\to\infty} (\phi_1\beta_1\phi_2)^{\frac{m+n}{2}}\left(\frac{n}{2}\right)^{k+\rho-1} = \lim_{n\to\infty}\left(\frac{1}{\beta}\right)^{\frac{m+n}{2}}\left(\frac{\beta_1\phi_1\phi_2}{\beta^2}\right)^{\frac{m+n}{2}}\left(\frac{n}{2}\right)^{k+\rho+m-2},
\end{aligned} \tag{5.14}$$

when $\frac{\beta_1\phi_1\phi_2}{\beta^2} < 1$, then $\lim_{n\to\infty} \frac{(\frac{n}{2})^{k+\rho+m-2}}{\left(\frac{\beta^2}{\beta_1\phi_1\phi_2}\right)^{\frac{m+n}{2}}} \approx 0$. Hence, $\lim_{n\to\infty} P_{out}(\gamma_{th}) \approx 0$. By using analysis in Sections 5.6.2.1 and 5.6.2.2, we provide necessary conditions for the series convergence of $P_{out}(\gamma_{th})$ given in (5.9).

The Cauchy ratio test is also known as d'Alembert's ratio test is used to test the convergence of the series in (5.9). The limit of the ratio of the two series terms are evaluated as follows $L = \lim_{i\to\infty}\left|\frac{a_{i+1}}{a_i}\right|$. The ratio test is evaluated as: if $L < 1$ then the series converges absolutely; if $L > 1$ then the series is divergent; if $L = 1$ or the limit fails to exist, then the test is inconclusive; the series could be either convergent or divergent.

5.6.3 Cauchy Test when k is varied and n is fixed

The a_{k+1} and a_k terms of $P_{out}(\gamma_{th})$ are given as following

$$\begin{aligned}
a_{k+1} &= \frac{\delta_{k+2}\Gamma(\rho+k+t+1)}{\Gamma(\rho+k+1)} \\
a_k &= \frac{\delta_{k+1}\Gamma(\rho+k+t)}{\Gamma(\rho+k)} \\
\lim_{k\to\infty}\left|\frac{a_{k+1}}{a_k}\right| &= \left|\frac{\delta_{k+2}}{\delta_{k+1}}\frac{\Gamma(\rho+k+t+1)}{\Gamma(\rho+k+1)}\frac{\Gamma(\rho+k)}{\Gamma(\rho+k+t)}\right| \\
&= \lim_{k\to\infty}\left|\frac{\delta_{k+2}}{\delta_{k+1}}\frac{(k+\rho+t)!}{(k+\rho)!}\frac{(k+\rho-1)!}{(k+\rho+t-1)!}\right|.
\end{aligned} \tag{5.15}$$

Now, by using the following ratio $\frac{\delta_{k+2}}{\delta k+1} \approx \frac{1}{k+2}$, we re-evaluate (5.15) as follows

$$L = \lim_{k\to\infty} \left| \frac{1}{k+2} \frac{\rho+k+t}{\rho+k} \right| < 1 \tag{5.16}$$

We get $L < 1$. Therefore, we consider that $P_{out}(\gamma_{th})$ series absolutely converges when k is varied and n is fixed.

5.6.4 Cauchy Test when n is varied, k is fixed, and $t = \frac{m+n}{2}$

$$L = \lim_{n\to\infty} \left| \frac{a_{n+1}}{a_n} \right| =$$
$$\lim_{n\to\infty} \left| \frac{(m+n+t)!\phi_1^{\frac{m+2}{2}+1}\beta_1^{\frac{m+n}{2}}\Gamma(k+\rho+\frac{m+n}{2})\phi_2^{\frac{m+n}{2}} n!(m+n)\beta^{m+n}(\frac{m+n}{2})!(\frac{m+n}{2})!}{(n+1)!(m+n+1)\beta^{m+n+1}(\frac{m+n}{2})!(\frac{m+n}{2}+1)!(m+n)!\phi_1^{\frac{m+n}{2}}\beta_1^{\frac{m+n}{2}}\Gamma(k+\rho+\frac{m+n}{2})\phi_2^{\frac{m+n}{2}}} \right|$$
$$= \lim_{n\to\infty} \frac{\phi_1(m+n)}{(n+1)\beta(\frac{m+n}{2}+1)} \approx \left| \frac{n}{n^2} \right| < 1. \tag{5.17}$$

We obtain $L < 1$, and thus, $P_{out}(\gamma_{th})$ absolutely converges when n is varied, k is fixed and $t = \frac{m+n}{2}$. The $P_{out}(\gamma_{th})$ converges based on the necessary condition for series convergence and the Cauchy ratio tests when $\frac{\beta_1\phi_2}{\beta} < 1$ and $\frac{\beta_1\phi_1\phi_2}{\beta^2} < 1$.

5.7 Generic Ergodic Capacity

The generic ergodic capacity formulation for the D2D assisted mmWave system under practical system constraints is discussed in this section. From the definition of ergodic capacity we get following generic expression

$$C = \mathbb{E}\left\{ \log_2(1+\gamma) \right\} = \mathbb{E}\left\{ \log_2\left(1 + \frac{aX}{1+Y+bX}\right) \right\}. \tag{5.18}$$

5.7.1 Lower Bound for Ergodic Capacity

By using concavity property of $\log_2(1+\delta\exp(y))$ function for a variable y and positive constant $\delta > 0$ and Jensen's inequality, we obtain a lower bound for ergodic capacity as $\log_2\left(1+\exp\left(\mathbb{E}\left\{\ln\left(\frac{aX}{1+Y+bX}\right)\right\}\right)\right)$. Therefore, the lower bound for ergodic capacity

considering D2D assisted mmWave network impaired by system constraints is given as

$$C_L \;=\; \log_2\left(1+\exp\left(\mathbb{E}\{\ln(aX)\}-\mathbb{E}\{\ln(1+Y+bX)\}\right)\right). \tag{5.19}$$

5.7.2 Upper Bound for Ergodic Capacity

By using the concavity property of the $\log_2(y)$ function and by applying the Jensen's inequaliy $\mathbb{E}\{g(y)\} < g(\mathbb{E}\{y\})$, we obtain the upper bond of ergodic capacity as

$$C_U \;=\; \log_2\left(1+\mathbb{E}\left\{\frac{aX}{1+Y+bX}\right\}\right). \tag{5.20}$$

5.8 Ergodic Capacity with Bounds over Fading Channels

Proposition 2 *The exact ergodic capacity for the D2D assisted mmWave network under transceiver distortion noise, imperfect CSI, and interference constraints is evaluated as*

$$\begin{aligned} C^{\text{Nak}} \;=\; & \sum_{k\,=\,0}^{\infty}\frac{\Phi_w\delta_k}{\ln(2)\Gamma(\rho_w+k)}\sum_{r\,=\,0}^{\xi_1}\frac{(\xi_1)!}{(\xi_1-r)!} \\ & \times\left(\frac{(-1)^{\xi_1-r-1}e^{\frac{1}{\beta_{0w}}}Ei(-\frac{1}{\beta_{0w}})}{\beta_{0w}^{\xi_1-r}}+\sum_{i\,=\,1}^{\xi_1-r}\frac{(i-1)!}{(-\beta_{0w})^{\xi_1-r-i}}\right) \\ & -\sum_{t\,=\,0}^{\infty}\frac{\Phi_z\delta_t}{\ln(2)\Gamma(\rho_z+t)}\sum_{n\,=\,0}^{\xi_2}\frac{(\xi_2)!}{(\xi_2-n)!} \\ & \times\left(\frac{(-1)^{\xi_2-n-1}e^{\frac{1}{\beta_{0z}}}Ei(-\frac{1}{\beta_{0z}})}{\beta_{0z}^{\xi_2-n}}+\sum_{j\,=\,1}^{\xi_2-n}\frac{(j-1)!}{(-\beta_{0z})^{\xi_2-n-j}}\right), \end{aligned} \tag{5.21}$$

where $\xi_1 = \rho_w+k-1$, $\xi_2 = \rho_z+t-1$, *and* $Ei(\cdot)$ *is exponential integral function given in [68, Eq. 8.212.2]. We calculate the parameters in (5.21) as*

$$\begin{aligned} \beta_{0w} \;&=\; \min[\frac{I_1}{m_1\Delta}(1+\kappa_1^2)\xi_1^I,\cdots,\frac{a+b}{m}], \\ \beta_{0z} \;&=\; \min[\frac{I_1}{m_1\Delta}(1+\kappa_1^2)\xi_1^I,\cdots,\frac{b}{m}], \end{aligned}$$

and sum of fading parameters is evaluated by

$$\rho_w = \sum_{i=1}^{N} m_i + m, \qquad \rho_z = \sum_{i=1}^{N} m_i + m.$$

Furthermore, in (5.21), we get

$$\Phi_w = \prod_{i=1}^{N} \left(\frac{\beta_{0w}}{\frac{I_i}{\Delta}(1+\kappa_i^2)\xi_i^I \beta_i} \right)^{m_i} ((a+b)\beta_{N+1})^{m_{N+1}},$$
$$\Phi_z = \prod_{i=1}^{N} \left(\frac{\beta_{0z}}{\frac{I_i}{\Delta}(1+\kappa_i^2)\xi_i^I \beta_i} \right)^{m_i} (b\beta_{N+1})^{m_{N+1}}.$$

Proof: More derivation steps of the ergodic capacity C^{Nak} are provided in Appendix C.2.

■

More compact representation of the ergodic capacity is evaluated by using the saddle point approximation PDF given in (5.8) for the summation of N Gamma RVs as

$$\begin{aligned} \tilde{C}^{\text{Nak}} = & \sum_{k=0}^{\nu_1} \frac{(\nu_1)!}{(\nu_1-k)!} \left(\frac{(-1)^{\rho_w-k-2} e^{\frac{1-c_1}{\beta_{0w}}}}{(\beta_{0w}/(1-c_1))^{k-1}} E_i(-\frac{1-c_1}{\beta_{0w}}) \sum_{j=1}^{\nu_1-k} \frac{(j-1)!}{(-\frac{\beta_{0z}}{1-c_2})^{\nu_1}} \right) \\ & - \sum_{t=0}^{\nu_2} \frac{(\nu_2)!}{(\nu_2-t)!} \left(\frac{(-1)^{\rho_z-t-2}}{(\beta_{0z}/(1-c_2))^{t-1}} E_i(-\frac{1-c_2}{\beta_{0z}}) \sum_{i=1}^{\nu_2-t} \frac{(i-1)!}{(-\frac{\beta_{0z}}{1-c_2})^{\nu_2}} \right), \end{aligned} \tag{5.22}$$

where $\nu_1 = \rho_w - 1$ and $\nu_2 = \rho_z - 1$,

$$c_1 = \max\left(1 - \frac{\beta_{0w}}{\frac{I_1}{\Delta}(1+\kappa_1^2)\xi_1^I \beta_1}, \cdots, 1 - \frac{\beta_{0w}}{(a+b)\beta_{N+1}}\right),$$

$$c_2 = \max\left(1 - \frac{\beta_{0w}}{\frac{I_1}{\Delta}(1+\kappa_1^2)\xi_1^I \beta_1}, \cdots, 1 - \frac{\beta_{0w}}{b\beta_{N+1}}\right).$$

Moreover, the lower bound of ergodic capacity for the proposed system model is calculated in Proposition 3 below.

Proposition 3 *The lower bound of ergodic capacity for the D2D network operating overlay to mmWave network under system impairments is given as*

$$C_L^{\text{Nak}} = \log_2\left(1+\exp\left(\ln(a)+\frac{\psi(m)-\ln(\frac{1}{\beta})}{\Gamma(m)\beta^m}-\sum_{t=0}^{\infty}\frac{\Phi_z\delta_t}{\ln(2)\Gamma(\rho_z+t)}\sum_{n=0}^{\xi_2}\frac{(\xi_2)!}{(\xi_2-n)!}\right.\right.$$
$$\left.\left.\times\left(\frac{(-1)^{\xi_2-n-1}e^{\frac{1}{\beta_{0z}}}Ei(-\frac{1}{\beta_{0z}})}{\beta_{0z}^{\xi_2-n}}+\sum_{j=1}^{\xi_2-n}\frac{(j-1)!}{(-\beta_{0z})^{\xi_2-n-j}}\right)\right)\right), \tag{5.23}$$

where $\psi(\cdot)$ is Euler psi function.

Proof: The proof is provided in Appendix C.3. ■

We evaluate a simplified and tight approximation for the lower ergodic capacity by applying (5.8) as

$$\tilde{C}_L^{\text{Nak}} = \log_2(1+\exp(\ln(a)+\frac{\psi(m)-\ln(\frac{1}{\beta})}{\Gamma(m)\beta^m}-\sum_{t=0}^{\nu_2}\frac{(\nu_2)!}{(\nu_2-t)!}\frac{(-1)^{\rho_z-t-2}}{(\beta_{0z}/(1-c_2))^{t-1}}$$
$$\times E_i(-\frac{1-c_2}{\beta_{0z}})\sum_{i=1}^{\nu_2-i}\frac{(i-1)!}{(-\frac{\beta_{0z}}{1-c_2})^{\nu_2}}). \tag{5.24}$$

Furthermore, the upper capacity bound for the proposed system model under system imperfections over Nakagami-m fading channel is analyzed below.

Proposition 4 *The upper bound for ergodic capacity given D2D overlay mmWave network under system constraints is evaluated as*

$$C_U^{\text{Nak}} = \log_2(1+\frac{a\beta\Gamma(1+m)}{\Gamma(m)}\sum_{t=0}^{\infty}\frac{\Phi_z\,\delta_t}{\Gamma(\rho_z+t)\beta_{0z}^{\rho_z+t}}e^{\frac{1}{\beta_{0z}}}\Gamma(t+\rho_z)\Gamma(t+\rho_z,\frac{1}{\beta_{0z}}). \tag{5.25}$$

Table 5.1. Network parameters for outage probability simulations.

Parameter	Value	Description
G_{m}	16 dB	Main lobe gain
G_{s}	-1.2 dB	Side/back lobe gain
f	28 GHz	Carrier frequency
N	5	Number of interfering nodes
L_i	{150, 60, 300, 100, 100}m	Interfering nodes' distances

Proof: The proof is given in Appendix C.4. ■ A tight approximation for the upper ergodic capacity by using (5.8) is computed by

$$\tilde{C}_U^{\mathrm{Nak}} = \log_2\left(1 + \frac{a\beta\Gamma(1+m)}{\Gamma(m)}\Phi_z\beta_{0z}^{-\rho_z}e^{\frac{1-c_2}{\beta_{0z}}}\Gamma\left(1-\rho_z, \frac{1-c_2}{\beta_{0z}}\right)\right), \tag{5.26}$$

where $\frac{c_2-1}{\beta_{0z}} < 0$.

5.9 Numerical Simulations

In this section, we present simulation results that demonstrate the outage probability and ergodic capacity performance analysis of the mmWave system. For this reason, we jointly and separately investigate the effect of transceiver distortion noise, imperfect CSI, and interference noise on the system performance.

5.9.1 Outage Probability Simulations Results

The outage probability formula provided in (5.9) was calculated by using three infinite summations. We apply Mathematica software to evaluate the approximate bounds for M, K, T upper limits. As a results, we determined that upper limit bounds with $M \geq 75, K \geq 1100, T \geq m + 75$ give an error of less than 0.3% between exact and approximated outage probability values, which is considered to be a good approximation.

In Table 5.1, we present system configurations for the outage probability simulations. In Fig. 5.2, we plot the outage probability versus SNR, where SNR $= \frac{P\mathbb{E}\{|h|^2\}}{N_0}$ and

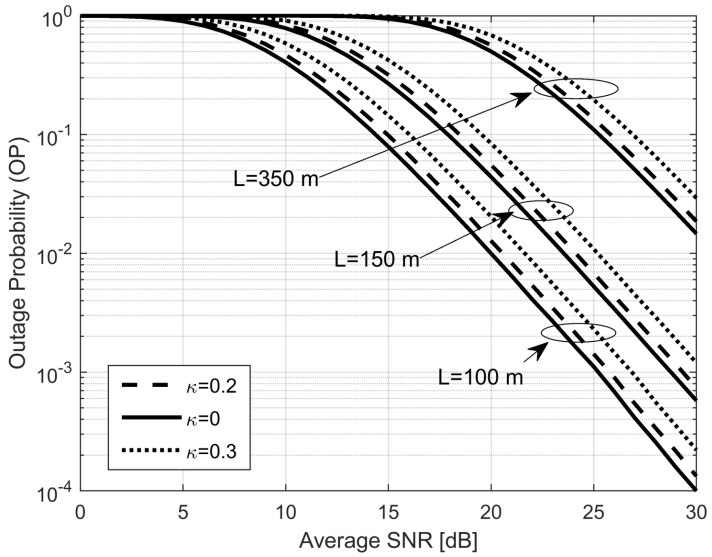

Figure 5.2. The outage probability versus average SNR at distances $L = 100; 150; 350$ m for $\kappa = 0; 0.2; 0.3$.

$\mathbb{E}\{|h|^2\} = m\beta$. Since β and P values are dependent on SNR we will not specify them. For LOS communication between links we set $m = 4$; interference fading parameters vary as $m_i = [1, 2, 3, 4, 5]$ to demonstrate i.n.i.d. fading parameters. Lower fading parameters has less LOS component and vice versa. We set $\gamma_{th} = 5$ dB, $L_0 = 100; 150; 350$ m, $\kappa = 0; 0.2; 0.3$. Fig. 5.2 demonstrates significant impact of distance on the outage probability (OP) performance. For example, when SNR = 25 dB, OP$(L_0 = 350\,\text{m}) = 0.1$, OP$(L_0 = 150\,\text{m}) = 0.5\times10^{-2}$, and OP$(L_0 = 100\,\text{m}) = 10^{-3}$. The outage probability degrade to the order of 10 every 10 m. At NLOS links, we get OP $= 1$ for both ideal/non-ideal system settings. In Fig. 5.3, we plot the outage probability versus normalized rate in bps/Hz, when $L_0 = 50$ m, $\kappa = 0.3$, SNR $= 20$ dB. Dashed lines plot ideal transceiver hardware, and solid lines plot non-ideal transceiver hardware. Also, we denote hexagonal markers for the plots with high interference fading parameters, and we denote circle markers for the plots with low m_i fading markers. In this figure, we aim to analyze how the interfering node's fading parameters may influence the performance of the outage probability.

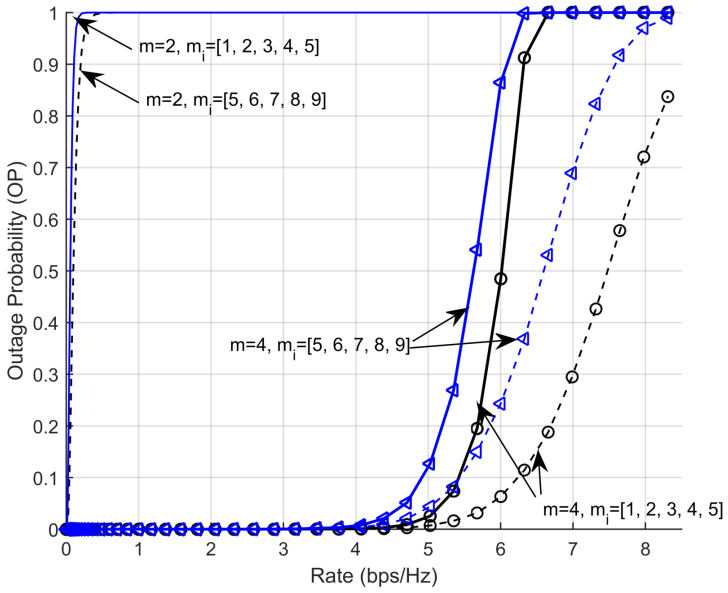

Figure 5.3. The outage probability versus rate for high and low interference fading parameters.

Table 5.2. Network parameters and their numerical values.

Parameter	Value	Description
G_{m}	16 dB	Main lobe gain
G_{s}	-1.2 dB	Side/back lobe gain
f	28 GHz	Carrier frequency
N	5	Number of interfering nodes
L_i	{150; 60; 300; 100; 100}m	Interfering nodes' distances

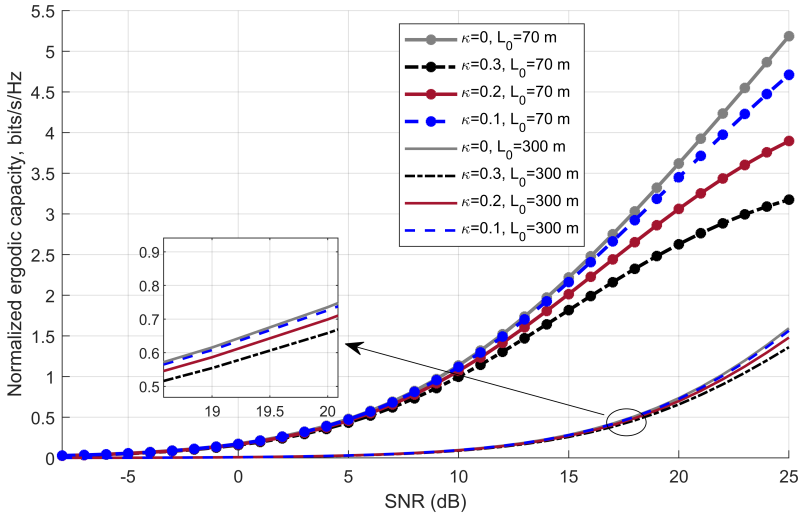

Figure 5.4. Normalized ergodic capacity for the D2D assisted communication network under the presence of interfering nodes given $L = 70, 300$ m and $\kappa = 0.1, 0.2, 0.3$.

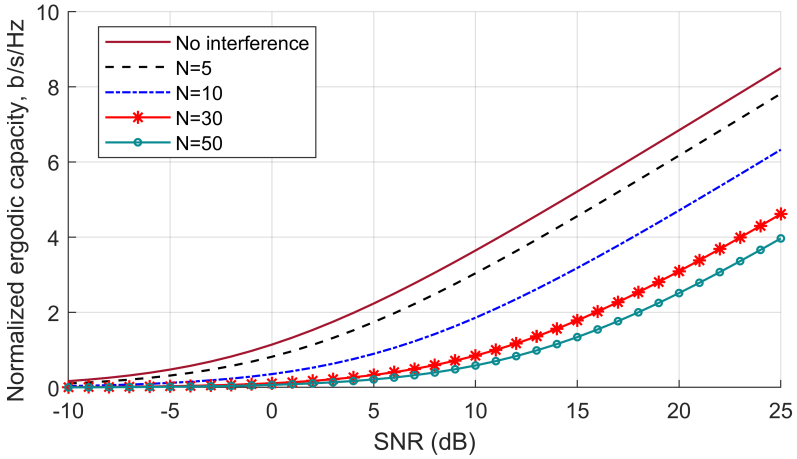

Figure 5.5. Normalized ergodic capacity for D2D network given $N = 0; 5; 10; 30; 50$, $\kappa = 0$, $L_0 = 70$ m, and ideal CSI.

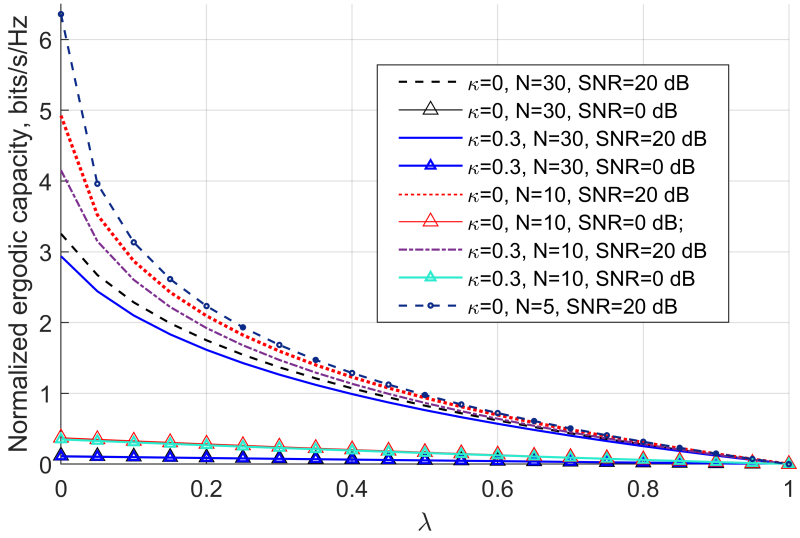

Figure 5.6. Normalized ergodic capacity versus λ for $N = 5, 10, 30$, $\kappa = 0; 0.3$, and SNR $= 0; 20$ dB.

5.9.2 Ergodic Capacity Simulation Results

In Table 5.2, we present network parameters that are used for the ergodic capacity analysis. In Fig. 5.4, we study the effect of transceiver distortion noise given ideal CSI and fixed number of interfering nodes when $\kappa = 0.1; 0.2; 0.3$, $N = 5$, $\lambda = 0$, and $L_0 = 70; 300$ m. In the case with a short distance between D2D pair at $L_0 = 70$ m, we observe that distortion level has a great impact on ergodic capacity when SNR>10 dB. For example, at $C^{\text{Nak}}(\kappa = 0.1, \text{SNR} = 20 \text{ dB}) = 2.5$ bits/s/Hz and at $C^{\text{Nak}}(\kappa = 0.3, \text{SNR} = 20 \text{ dB}) = 1$ bits/s/Hz, meaning that normalized ergodic capacity degrades 2.5 times when

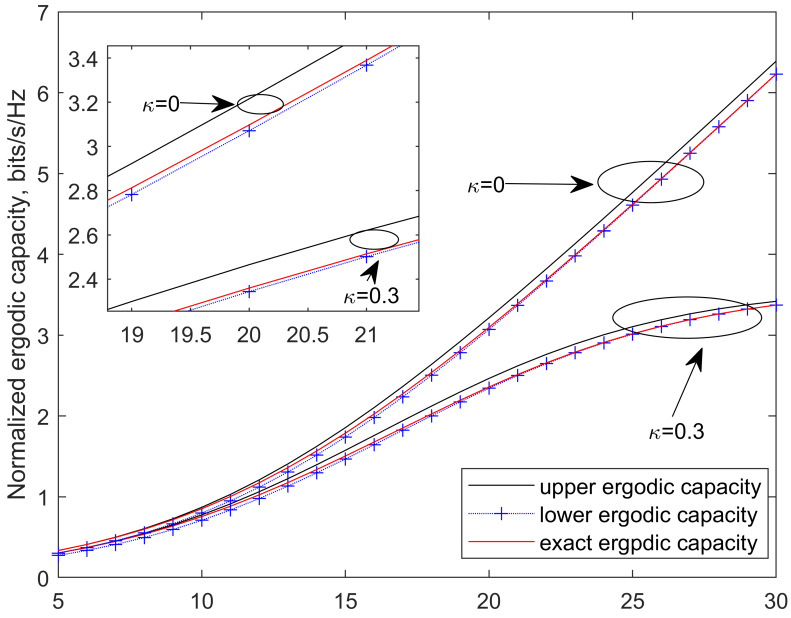

Figure 5.7. Normalized ergodic capacity and its upper/lower bounds for the D2D assisted network for $L = 70$ m, $N = 30$, $\kappa = 0; 0.3$, and ideal CSI.

distortion level increases from 0.1 to 0.3. Another observation from Fig. 5.4 is that a distortion between D2D nodes has a crucial effect on the capacity of the system. For instance, when $C^{\text{Nak}}(L_0 = 70 \text{ m}, \text{SNR} = 10 \text{ dB}, \kappa = 0.1) = 1$ bits/s/Hz and $C^{\text{Nak}}(L_0 = 300 \text{ m}, \text{SNR} = 10 \text{ dB}, \kappa = 0.1) = 0.1$ bits/s/Hz, there is 10 times performance degradation due to a higher distance. In Fig. 5.5, we vary number of interfering nodes $N = 0; 5; 10; 30; 50$ and assume ideal transceiver hardware, $\kappa = 0$, and ideal CSI, $\lambda = 0$, $L_0 = 70$ m. Hence, at SNR $= 10$ dB we get following normalized ergodic capacity performance: $C^{\text{Nak}}(N = 0) = 3.6$ bits/s/Hz, $C^{\text{Nak}}(N = 5) = 3$ bits/s/Hz, $C^{\text{Nak}}(N = 10) = 1.8$ bits/s/Hz, $C^{\text{Nak}}(N = 30) = 0.8$ bits/s/Hz, and $C^{\text{Nak}}(N = 50) = 0.58$ bits/s/Hz. From no interference case to 50 interfering nodes case the ergodic capacity performance was degraded to 6.2 times. In Fig. 5.6, we plot normalized ergodic capacity versus CSI estimation error variance, $\lambda \in [0, 1]$. At the same time, we alter number of interfering nodes $N = 10; 30$, SNR $= 0; 20$ dB, and $\kappa = 0; 0.3$. By applying these system settings we observe that as CSI error variance increases the normalized ergodic capacity rapidly decreases. SNR plays a key role in ergodic capacity performance. At low SNR $= 0$ dB, the normalized ergodic capacity barely

achieves 0.1 b/s/Hz. In Fig. 5.7, we display exact ergodic capacities with its upper and lower bounds for $L_0 = 70$ m, $\kappa = 0; 0.3$, $N = 30$, and ideal CSI. This figure demonstrates tight upper and lower ergodic capacity bounds of the exact ergodic capacity for both ideal and non-ideal system models. Ergodic capacity present similar performance at low SNR for ideal and non-ideal transceiver hardware. However, ergodic capacity performance significantly degrade at medium and high SNR regime. Transceiver impairments cause capacity ceiling and limit the performance. Capacity saturation at high SNR regime is explained due to distortion noise power proportionality to signal power.

5.10 Chapter Summary

One of the promising paradigms of next-generation networks is D2D communication that empowers both high speed and low latency communication. The advantage of D2D communication is that no base station resources are utilized during D2D communication. The major drawback of current research in D2D communication is the consideration of ideal transceiver hardware while evaluating ergodic capacity and outage probability of the network. In this chapter, we developed a comprehensive analytical framework that studied outage probability and ergodic capacity of the D2D network overlaid upon 5G mmWave network under practical hardware distortion noises, imperfect CSI, and interference noises. Note that all channels are modelled as i.n.i.d. Nakagami-m fading channels, which is a suitable assumption for mmWave communication according to recent research. We derived closed-form expressions for the outage probability and presented the convergence analysis of the outage probability formula. Moreover, we calculated the exact ergodic capacity with it's upper and lower bounds and presented a simplified version of the ergodic capacity expressions by using saddlepoint approximation of the summation of N i.n.i.d Gamma RVs. We corroborate numerical results by Monte Carlo simulations.

Chapter 6

Maximum Sub-Array Transmission Diversity for Millimeter Wave Network under RF Power Leakage and Distortion Noise Constraints

In this chapter, we study the effect of distortion noise and RF power leakage in a massive MIMO mmWave system. A multi-user base station operates on a hybrid beamforming structure and communicates with a single antenna user equipment. Regardless of spatial separations between adjacent data transmissions, RF power leaks from side/back lobes of beamformed antennas during simultaneous transmission. Moreover, distortion noise from transceiver hardware adds further performance degradation. We propose a maximum sub-array transmission diversity technique based on hybrid beamforming to compensate for the effect of RF power leakage and residual distortion noises. In this chapter, we study how RF power leakage and distortion noise levels degrade the outage probability and ergodic capacity performance. An analytical model for mmWave connectivity yields closed-form expressions for the outage probability and ergodic capacity. These closed-form expressions were through Monte-Carlo Matlab simulations. This chapter was written based on author's work in [91].

6.1 Introduction

Massive MIMO antennas and mmWave frequency are two fundamental technologies for future communication networks. Currently, 5G pioneer countries like China, South Korea, the USA, and the UK are already building commercial 5G networks. The major advantage of mmWave systems is beamforming and beam steering techniques. There are three major types of beamforming/steering, such as digital [92, 93], analog, and hybrid beamforming [94–96] in mmWave systems. On the one hand, digital beamforming demonstrates accurate beamforming at the cost of a high number of RF chains that convert the analog signal to the digital domain through ADCs/DACs, which allows taking full advantage of digital processing algorithms. On the other hand, digital beamforming is cost-ineffective in mmWave systems due to a high number and cost of ADCs/DACs that require massive MIMO systems. Alternatively, analog beamforming is easy and chip to implement since it requires only one RF chain, i.e., one ADC/DAC per user equipment, and the cost of phase shifters is not high as well. The major limitation of analog beamforming is a calibration of phase shifters, which is time-consuming and imprecise. The main disadvantage of analog beamforming is single-user communication per analog beamformer network as opposed to digital and hybrid beamforming networks that could serve multi-users per cell. Hybrid beamforming combines the advantages of both analog beamforming and digital beamforming: multistream digital processing and array gain. Therefore, hybrid beamforming is proposed as a potential beamforming structure in mmWave systems by industry and research community. It is well investigated that mmWave frequencies suffer from a high propagation path loss caused by water vapor and oxygen absorption, as well as signal blockages (self blockage, static blockage, and dynamic blockage) that complicates mmWave communication. Therefore, it's essential to consider independent diversity communication between a reference transmitter and receiver nodes to sustain high performance communication.

In this chapter, we assume downlink communication from the mmWave base station to corresponding UE nodes by using maximum sub-array combining diversity technique

built on hybrid beamforming structure. The proposed system model is constrained by RF power leakage and transceiver distortion noises.

6.1.1 Related work

The authors in [97] implemented dual function hybrid beamforming that performs diversity and beamforming functionalities at the same time. For this purpose, it was suggested to separate antenna array elements into sub-arrays, where each sub-array is dedicated per a single UE. These sub-arrays were spatially separated by more than 5λ distance to guarantee independent data transmission and fading channels. The work in [98] proposed a novel hybridly connected beamforming structure that outperforms the partially connected beamforming structure. However, authors in [97, 98] considered ideal transceiver hardware similar to majority work in the technical literature. Cm wave frequencies are more prone to distortion noise than mmWave frequencies. We model the aggregate effect of transceiver hardware imperfections by the statistical additive Gaussian model discussed in 2.3.2.

RF power leakage that we consider in this chapter takes place when the side/back lobe of the neighboring user signal is leaked to the reference transmitter's data stream and received as RF power leakage noise at the reference receiver side. There is limited work that investigates RF power leakage from neighboring nodes in multi-user communication based on hybrid beamforming. The authors in [11] proposed a leakage-based precoding scheme for a downlink multi-user MIMO system considering ideal transceiver hardware and channel estimation errors. Similarly, a leakage-based hybrid beamforming design for a multi-user mmWave network was studied in [12]. This work emphasized analog precoder/combiner design to increase channel gains between transmitter and receiver nodes, as well as it aimed to design digital precoder to optimize signal-to-leakage-noise ratio.

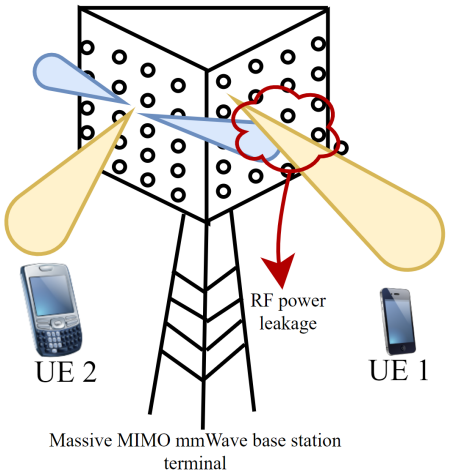

Figure 6.1. Hybrid beamforming mmWave network model under RF power leakage constraint by using SDMA to separate users.

6.1.2 Contributions

- We develop a practical model for multi-user mmWave network based on hybrid beamforming and studied RF power leakage from neighboring UEs and aggregate transceiver distortion noise.
- MST diversity allows giving a weight to independent sub-arrays to enhance the resultant outage probability. The MST technique compromise for RF power leakage, the path loss of mmWave link, and transceiver distortion noise.
- Signal-to-RF leakage-distortion-noise ratio (SRDNR) is defined, and its distribution is formulated to evaluate the outage probability and ergodic capacity.

6.2 System Model

A downlink multi-user mmWave network presented in Fig. 6.1 uses space-division multiple access (SDMA) for concurrent communication with UE nodes. We consider two UE nodes in the network for analytical tractability; UE 1 is the reference Rx user, and simultaneous transmission to UE 2 causes RF power leakage from the side/back lobe gains of UE 2. Therefore, N_s multiple analog beams are created with the same steering direction towards desired UE 1. It is important to separate two consecutive sub-arrays

to the distance d, $d > 5\lambda$, that is at least 5 times more separation than the length of the wavelength [97] for independent and uncorrelated communication paths from each sub-array. Therefore, we consider $d > 5\lambda$ separation between sub-arrays for independent and uncorrelated Nakagami-m fading channels between mmWave base station and UEs.

$$G(\theta) = \begin{cases} G_{\mathrm{m}}, & |\theta| \leq \theta_b, \\ G_{\mathrm{s}}, & \text{otherwise}, \end{cases} \tag{6.1}$$

where θ is a boresight angle, θ_b is an antenna beamwidth, G_{m} and G_{s} are main lobe and side/back lobe antenna gains within given antenna beamwidth. Also, we consider that the mmWave base station uses control channels to be aligned to UEs. An ideal beam sweeping process is assumed to estimate an angle of arrival. In Fig. 6.2, we present a general structure of the hybrid beamformer network that is dedicated to each UE node. It could be seen from this figure that the base station dedicates N_t antennas per UE, which are sub-divided into N_s sub-arrays with N antennas per sub-array. Sub-array antennas are fed to phase shifter networks to create N_s beams towards desired UE. We assume that a receiver UE is equipped with a single antenna. In Fig. 6.2, we present a general structure of the hybrid beamformer network that is dedicated to each UE node. The data signal s with average power $P = \mathbb{E}\{|s|^2\}$ is fed to linear digital precoder w with the size $N_s \times 1$. Hence, the digital precoder weight for arbitrary sub-array k is defined as

$$w_k = \frac{h_k^*}{\|h_k\|}, \tag{6.2}$$

where $\|\cdot\|$ is the Euclidian norm, h_k is the Nakagami-m fading channel amplitude with fading parameter $m_k > 0$ and integer positive scale parameter $\beta_k > 0$. After the data signal is multiplied to the digital precoder vector w it is fed to N_s phase shifter networks to build N_s independent beams towards UE 1. Mathematically, we could represent the received signal as

$$y = \sqrt{Q}\boldsymbol{h}^t \left(\boldsymbol{w}\sqrt{G_m}(s_1 + \epsilon_1) + \boldsymbol{w}'\sqrt{G_s}(s_2 + \epsilon_2) \right) + n. \tag{6.3}$$

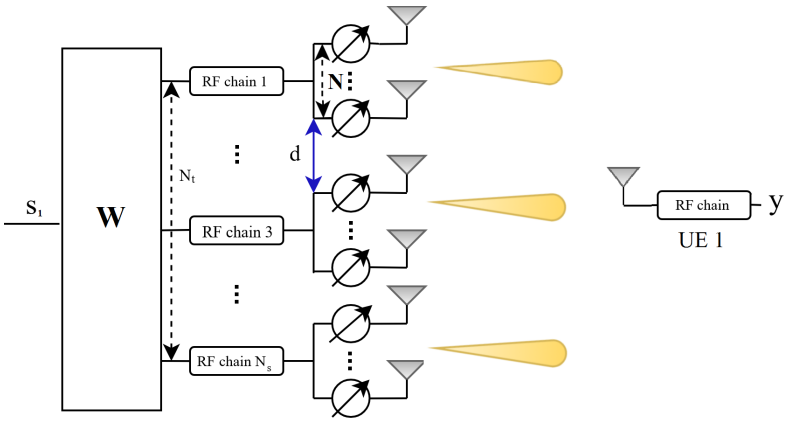

Figure 6.2. Hybrid beamforming network with maximum sub-array transmission diversity technique towards UE 1.

We consider that the base station dedicates same number of resources namely antenna elements and phase shifters to the UE 2 as well. We call g for Nakagami-m fading channel from UE 2. Similarly to UE 1, $\boldsymbol{w}'$ is the digital precoder vector of UE 2 which is evaluated as $\boldsymbol{w}' = \frac{\boldsymbol{g}^*}{\|\boldsymbol{g}\|}$. We denote path loss as $Q = L^{-\alpha_0}$, where L is a communication distance, α_0 is path loss exponent. Moreover, aggregate transceiver distortion noise is modelled as the statistical Gaussian model $\epsilon_{1,2} \sim \mathcal{CN}(0, \kappa^2 P_{1,2})$, where κ is a measure of EVM that was discussed in Section 2.3.2.1. Now, by using expression for the digital precoder $\boldsymbol{w}$ and $\boldsymbol{w}'$ the following equation is obtained for the received signal

$$y = \sqrt{Q}\|\boldsymbol{h}\|\sqrt{G_m}(s_1 + \epsilon_1) + \sqrt{Q}\frac{\boldsymbol{g}^*}{\|\boldsymbol{g}\|}\boldsymbol{h}^{\boldsymbol{t}}\sqrt{G_s}(s_2 + \epsilon_2) + n. \tag{6.4}$$

From (6.4), the SRDNR can be calculated as,

$$\gamma^{\mathrm{RD}} = \frac{P_1 Q G_m \sum_{k=1}^{N_s} |h_k|^2}{P_1 Q \kappa^2 G_m \sum_{k=1}^{N_s} |h_k|^2 + \frac{P_2 Q G_s |\sum_{k=1}^{N_s} h_k g_k^*|^2 (1+\kappa^2)}{\sum_{k=1}^{N_s} |g_k|^2} + \sigma^2}. \tag{6.5}$$

For simplification purposes of (6.5), we apply the Cauchy-Schwarz inequality $|\sum_{k=1}^{N_s} h_k g_k^*|^2 \leq \sum_{k=1}^{N_s} |h_k|^2 \sum_{k=1}^{N_s} |g_k^*|^2$ and obtain simplified SRDNR as

$$\gamma^{\mathrm{RD}} \geq \frac{a \sum_{k=1}^{N_s} X_k}{b \sum_{k=1}^{N} X_k + c \sum_{k=1}^{N} X_k + 1}, \tag{6.6}$$

where we make following variable assignment $X_k = |h_k|^2$, $a = \frac{P_1 G_m Q}{\sigma^2}$, $b = \frac{\kappa^2 P_1 G_m Q}{\sigma^2}$, and $c = \frac{P_2 G_s Q(1+\kappa^2)}{\sigma^2}$. The channel power gains of i.i.d. Nakagami-m distribution are i.i.d. Gamma distributed RVs, X_k for $k = 1, \cdots, N_s$.

Lemma 4 *Let us consider a finite set of non-negative i.i.d. Gamma RVs $X_k = \{1, \cdots, N_s\}$. The CDF of summation of N_s i.i.d. Gamma RVs is another Gamma RV with the scaled non-negative fading parameter given as*

$$F_Y(y) = \frac{1}{\Gamma(m_k N_s)} \gamma\left(m_k N_s, \frac{y}{\beta_k}\right), \tag{6.7}$$

$\Gamma(\cdot)$ is the Gamma function defined in [68, Eq. 8.310.1] and $\Gamma(\cdot,\cdot)$ is incomplete Gamma function described in [68, Eq. 8.350.1]. Similarly, the PDF of summation of N_s Gamma RVs is given as

$$f_Y(y) = \frac{1}{\Gamma(mN_s)\beta^{mN_s}} y^{mN_s - 1} e^{-\frac{y}{\beta}}. \tag{6.8}$$

Next, the outage probability was evaluated by making use of Lemma 4 below.

6.3 Outage Probability Analysis

In this section, we evaluate the closed-form expression for the outage probability given N_s RF leakages created by side/back lobe gains of MST diversity transmission from neighbouring UE 2. According to definition, the outage probability is defined as $P_{out} = \Pr(\gamma^{\mathrm{RD}} \leq \gamma_{th})$, where γ_{th} is a predefined threshold on γ^{RD}. The closed-form expression for the outage probability is evaluated in Proposition 5 below.

Proposition 5 *Let us consider a finite set of non-negative i.i.d. Gamma RVs* $X_k = \{X_1, \cdots X_{N_s}\}$ *i.i.d. Gamma distributed RVs and* $a > 0$, $b > 0$, *and* $c > 0$ *are positive and real constants. The CDF of* γ^{RD} *presented in (6.6) results in outage probability given as*

$$\Pr(\gamma^{\mathrm{RD}} < \gamma_{th}) = \begin{cases} \frac{\gamma\left(mN_s, \frac{\gamma_{th}}{(a-b\gamma_{th}-c\gamma_{th})\beta}\right)}{\Gamma(mN_s)}, \gamma_{th} < \frac{a}{b+c} \\ 1, \quad \gamma_{th} > \frac{a}{b+c}. \end{cases} \tag{6.9}$$

Proof: By expressing $Y = \sum_{k=0}^{N_s}$ *and with the aid of Lemma 4, we define the outage probability of the proposed system as*

$$\begin{aligned} \Pr(\gamma^{\mathrm{RD}} < \gamma_{th}) &= \Pr\left(\frac{aY}{bY + cY + 1} < \gamma_{th}\right) \\ &= \begin{cases} \Pr\left(Y < \frac{\gamma_{th}}{a-b\gamma_{th}-c\gamma_{th}}\right), & \gamma_{th} < \frac{a}{b+c} \\ 1, \quad \gamma_{th} \geq \frac{a}{b+c}. \end{cases} \end{aligned} \tag{6.10}$$

■

Next section delivers the ergodic capacity analysis of the proposed system model.

6.4 Ergodic Capacity Analysis

Let us consider two UEs in a mmWave network that uses MST diversity with RF power leakage and distortion noise constraints. The ergodic capacity is a function of SRDNR defined in (6.6) and evaluated by $C = \mathbb{E}\{\log_2(1 + \gamma^{\mathrm{RD}})\}$. Hence, ergodic capacity is represented as

$$\begin{aligned} C =& \mathbb{E}\left\{\log_2(1 + \frac{aY}{(b+c)Y + 1})\right\} \\ =& \mathbb{E}\left\{\log_2((a+b+c)Y + 1) - \log_2((b+c)Y + 1)\right\}. \end{aligned} \tag{6.11}$$

Proposition 6 *Let us consider two users mmWave network that uses MST diversity, while RF power leakage and distortion noise present in the system. The ergodic capacity is calculated as*

$$C = \frac{1}{\Gamma(m_k N_s)} \sum_{i=0}^{m_k N_s - 1} \frac{(m_k N_s - 1)!}{(m_k N_s - 1 - i)!} \left(\frac{(-1)^{m_k N_s - i - 2} e^{\frac{1}{(a+b+c)\beta}}}{((a+b+c)\beta)^{m_k N_s - 1 - i}} \right.$$
$$\times Ei\left(-\frac{1}{(a+b+c)\beta}\right) + \sum_{k=1}^{m_k N_s - 1 - i} \frac{(k-1)!}{(-(a+b+c)\beta)^{m_k N_s - 1 - i - k}}$$
$$\left. - \frac{(-1)^{m_k N_s - i - 2} e^{\frac{1}{(b+c)\beta}}}{((b+c)\beta)^{m_k N_s - 1 - i}} Ei\left(-\frac{1}{(b+c)\beta}\right) - \sum_{k=1}^{m_k N_s - 1 - i} \frac{(k-1)!}{(-(b+c)\beta)^{m_k N_s - 1 - i - k}} \right), \tag{6.12}$$

Proof: More derivation steps for evaluating ergodic capacity with system constraints are given Appendix D.1. ■

6.4.1 Lower Bound for Ergodic Capacity

The lower ergodic capacity is approximated by $C_L = \log_2(1 + a\exp(x))$ function with $a > 0$ and variable x. Since $\log_2(1 + a\exp(x))$ is a concave function, the lower bound for ergodic capacity for non-ideal trasnceiver with MST diversity constrained by RF power leakage and distortion is given by

$$C_L = \log_2\left(1 + \exp(\mathbb{E}\{\ln(aY)\}) - \mathbb{E}\{\ln\left((b+c)\,Y + 1\right)\}\right). \tag{6.13}$$

Proposition 7 *A lower bound for the ergodic capacity over Nakagami-m fading channel for the mmWave network with two UEs constrained by RF power leakage and distortion noise is evaluated as*

$$C_L^{\text{Nak}} = \log_2(1 + \exp(\ln(a) + \psi(m_k N_s) - \ln(\frac{1}{\beta}) - \ln(1 + (b+c) m_k N_s \beta)), \tag{6.14}$$

where $\psi(\cdot)$ is Euler psi function [68, Eq. 8.360].

Proof: More details are presented in Appendix D.2. ■

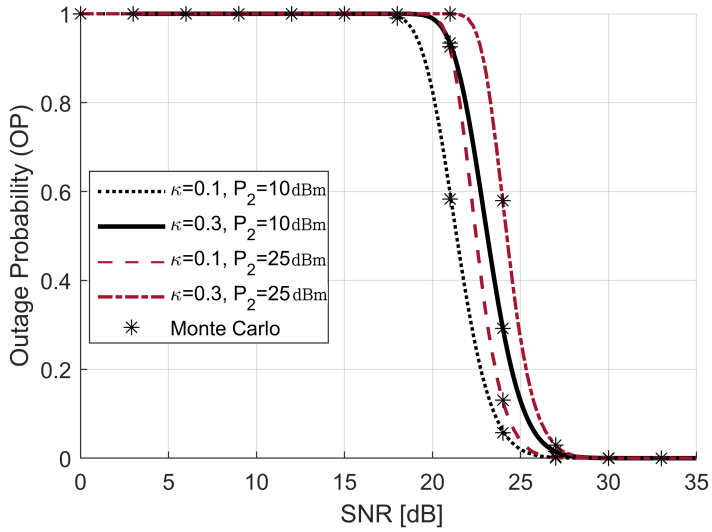

Figure 6.3. Outage probability curves versus receive SNR for different levels of transceiver distortion noise and UE 2 average power.

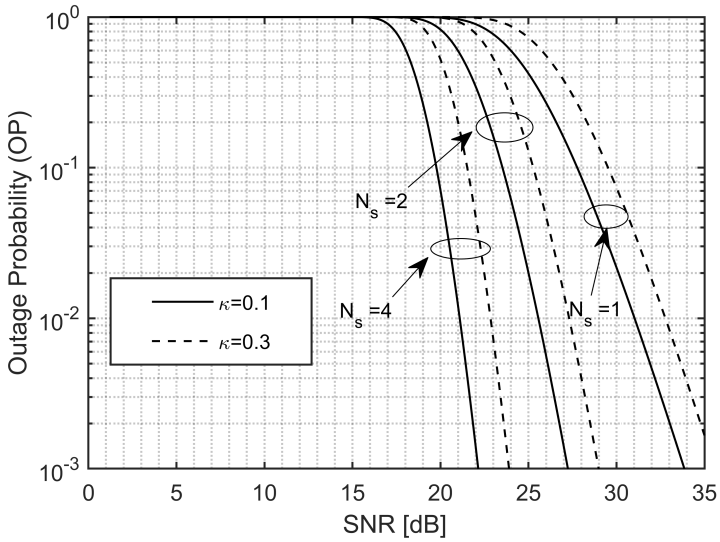

Figure 6.4. Outage probability for a hybrid beamforming mmWave network model for $L = 50$ m and different levels of transceiver distortion noise.

6.5 Numerical Simulations

In this section, we present simulation results that validate the closed-form analytical expressions given in Sections 6.3 and 6.4. The configurations of network parameters are presented in Table 6.1. In Figs 6.3-6.5, we notice that performance analysis of outage

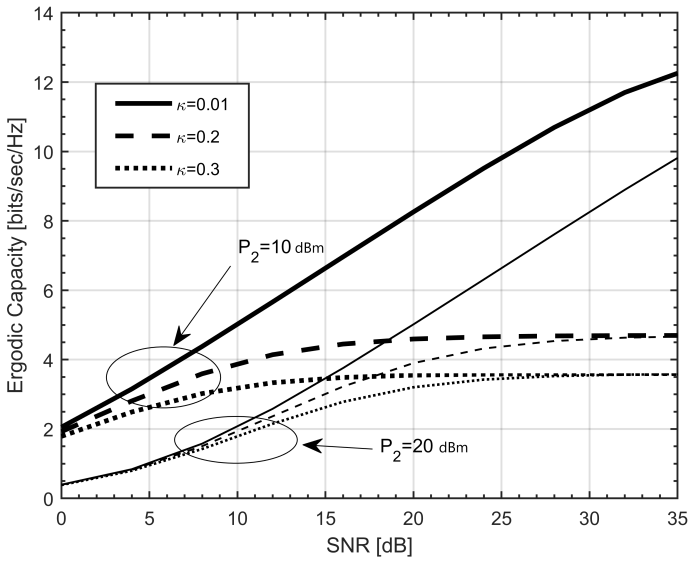

Figure 6.5. Ergodic capacity for a hybrid beamforming mmWave network model under RF power leakage constraint and transceiver distortion parameters $\kappa = 0.01; 0.2; 0.3$.

probability and ergodic capacity plots at $\kappa = 0$ and $\kappa = 0.01; 0.1$ are very close to each other, therefore, we decided not to include $\kappa = 0$ plots in the figures for clarity purposes. In Fig. 6.3, we present the outage probability performance analysis given aggregate distortion noise and RF power leakage constraints. We assume LOS links for UE 1 and UE 2. In Fig. 6.3, we vary both distortion level and UE 2 transmit power $P_2 = 10, 25$ dBm that causes RF power leakage. From this figure, we notice that both higher level of distortion noise level and RF power leakage negatively affects the outage probability performance.

Table 6.1. System parameters of the proposed system model

Parameter	Value	Description
α_L	2	LOS path-loss exponent
α_N	4	NLOS path-loss exponent
L	50 m	Distance
m_L	4	LOS fading parameter
m_N	2	NLOS fading parameter
W	100 MHz	Bandwidth
f	28 GHz	Operating frequency
G_m	16 dB	Main lobe gain
G_s	-5 dB	Side lobe gain
N_s	2	Number of sub-arrays
γ_{th}	6 dB	Threshold

In Fig. 6.4, we vary number of diversity branches N_s of UE 1 given UE 2 power level $P_2 = 10$ dBm. In this figure, we alter the number of diversity branches $N_s = 1, 2, 4$ with for different distortion values $\kappa = 0.1, 0.3$. As a number of diversity branches increases, the quality of communication is increasing as well. In Fig. 6.5, we study ergodic capacity versus SNR for $P_2 = 10, 20$ dBm and $\kappa = 0.01, 0.2, 0.3$. Distortion noise significantly deteriorates the performance of ergodic capacity. As the power of UE 2 increases, it creates more RF power leakage from side/back levels of UE 2 towards UE 1.

6.6 Chapter Summary

In this chapter, we proposed to implement the MST diversity based hybrid beamforming mmWave network to mitigate the negative impacts of RF power leakage and transceiver distortion noise. The MST diversity technique has demonstrated a better outage probability performance in comparison to a non-diversity transmitter case at the cost of multiple RF chains. Simulation results have demonstrated that both RF power leakage and transceiver distortion noise considerably deteriorate the outage probability and ergodic capacity performances. The MST diversity can also cope with communication link blockages since we consider independent and uncorrelated paths, which are less likely to be blocked at the same time.

Chapter 7

Conclusion and Future Work

7.1 Conclusion

Future communication technologies such as 5G/6G will not only revolutionize current network deployment but also change people's lifestyles and perceptions about services. HD TV streaming, remote robotic operations, self-driving vehicles, remote health monitoring systems are all potential services that are coming to reality with 5G/6G services. A large number of bandwidth-hungry devices and services require a wide spectrum for their operation. Therefore, it is crucial to study efficient spectrum sensing/sharing techniques as well as mmWave frequencies with enormous spectrum potential. This work studies future communication systems such as spectrum sensing/sharing networks and mmWave communication considering non-ideal transceiver hardware by using statistical Gaussian distortion noise.

In Chapter 3, we investigated the underlay dual-hop cognitive relay network by inspecting the effect of residual distortion noise constraint. We presented a closed-form expression for the outage probability and performed numerical analysis. It was shown that the transmission rate could be adjusted based on channel fading parameters to meet a specific outage probability.

In Chapter 4, we developed novel hypotheses test statistics for the improved ED under residual distortion noise constraints. This chapter presented closed-form expressions for the detection and false alarm probabilities subjected to fading and non-fading environment. Additionally, the total error rate, AUC, and ROC analysis are performed to verify

detection accuracy of the improved ED. In Chapter 5, one of the key technologies of 5G network D2D communication in mmWave was modelled considering several system imperfections, including residual distortion noise, imperfect CSI, and N interfering nodes. In Chapter 6, hybrid beamforming based mmWave base station with the MST diversity technique was proposed to improve the system performance while RF power leakage and transceiver distortion noises were present in the system.

7.2 Future Work

Further research related to Chapter 3 could be on underlay multihop relay network with a data fusion center that considers transceiver distortion noise and mmWave channel modelling. Moreover, secure communication in mmWave relaying network considering residual distortion noise could be investigated as a future research direction. The recent work in [99] studied randomize-and-forward relaying mmWave network in the presence of several eavesdroppers, however, this work did not consider the effect of residual distortion noise and other channel imperfections. In this chapter, we studied i.i.d. Nakagami-m fading channels between nodes. As a future work, one can extend this to the case of correlated Nakagami-m channels.

The future research concerning Chapter 4 will study other transceiver distortion models and derive closed-form expressions for the detection and false alarm probabilities for fading and non-fading channel models. An accurate distortion model that describes the behavior of nonlinear low-noise amplifier, local oscillator phase noise, and oversampling finite-resolution analog-to-digital converter by using Bussgang's theorem [100] could be applied for hardware distortion noise modelling.

The network model in Chapter 5 considered fixed geometry of the device nodes, and it did not consider device mobility. It would be essential to study the stochastic geometry of the device nodes as well as mobility factor for practical D2D assisted mmWave networks. Moreover, the continuation of this study would be modelling of blockage effect in

D2D assisted mmWave communication. Moreover, it would be particularly interesting to investigate side/back lobe suppression techniques discussed in [101].

The future work for Chapters 5 and 6 will be optimization problems using the derived expressions that can be formulated to find optimal power control schemes. Also, hardware and power-efficient hybrid beamforming structure is a key to reduce the cost for mmWave network deployment as well as essential for green communication. A simple phase over-samplers and a switch network were proposed in [102] for building low complexity hybrid precoding/combining architecture at satisfactory spectral efficiency. One could study low complexity hybrid precoding/combining structures that would be prone to residual distortion noise. The authors in [103] presented power consumption, spectral efficiency, and hardware complexity analysis for hybrid beamforming structure that uses either a phase-shifting network or switching network for analog processing purposes. Therefore, one potential research direction could be on the optimum structure for the analog part of the hybrid beamforming network to enhance energy efficiency and reduce cost.

Moreover, the future research direction could be studying residual distortion noise mitigation algorithms and techniques. Preliminary work that attempted to mitigate the transmitter residual distortion noise component was presented in [32]. The next step would be studying the transmitter/receiver distortion noise whitening algorithms and techniques.

Appendix A

Appendix for Chapter 3

The derivation of Lemma 1 is demonstrated in this section. The CDF of SNDR, $F_T(x)$ for Nakagami-m channel is used to obtain the outage probability as follows

$$\begin{aligned} F_{T_j}(x) &= \Pr(T_j \leq x) = \Lambda_1 + \Lambda_2, \\ \text{where } \Lambda_1 &= \Pr\Big\{\frac{P_j|h_1|^2}{P_j|h_1|^2\kappa_j^2 + N_j} \leq x, P_j \leq \frac{I}{|h_2|^2}\Big\} \\ &= \Pr\{|h_1|^2 \leq \frac{xN_j}{P_j - xP_j\kappa_j^2}, |h_2|^2 > \frac{I}{P_j}\}. \end{aligned} \tag{A.1}$$

Due to the independence of $|h_1|^2$ and $|h_2|^2$ RVs, The Λ_1 and the Λ_2 terms could be written as

$$\Lambda_1 = F_{h_1}(\frac{xN_j}{P_j - xP_j\kappa_j^2})F_{h_2}(\frac{I}{P_j}) \tag{A.2}$$

The Λ_1 term is expanded by using the CDF of gamma distribution as

$$\Lambda_1 = \frac{\gamma(m_1, \frac{\beta_1 xN_j}{P_j - xP_jk_j^2})}{\Gamma(m_1)} \frac{\gamma(m_2, \frac{\beta_2 I}{P_j})}{\Gamma(m_2)}. \tag{A.3}$$

and

$$\Lambda_2 = \Pr\Big\{\frac{\frac{\bar{I}}{N_j}\frac{|h_1|^2}{|h_2|^2}}{\frac{\bar{I}}{N_j}\frac{|h_1|^2}{|h_2|^2}\kappa_j^2 + N_j} \leq x, P_j > \frac{I}{|h_2|^2}\Big\}, \tag{A.4}$$

or equivalently

$$\begin{aligned}\Lambda_2 &= \Pr(|h_1|^2 \leq (\frac{x|h_2|^2 N_j^2}{I(1-x\kappa_j^2)}, |h_2|^2 > \frac{I}{P_j}) \\ &= \int_{\frac{I}{P_j}}^{\infty} f_{h_2}(y) \int_0^{\frac{xyN_j^2}{I(1-x\kappa_j^2)}} f_{h_1}(z) dz dy.\end{aligned} \tag{A.5}$$

The integral in (A.5) is evaluated by using the PDF and the CDF of Nakagami-m fading channel and [68, Eq. (3.381.9)] as

$$\begin{aligned}\Lambda_2 &= \frac{1}{\Gamma(m_1)} \int_{\frac{I}{P_j}}^{\infty} f_{h_2}(y) \Gamma(m_1) \big(1 - e^{-\frac{xyN_j^2\beta_1}{I(1-x\kappa_j^2)}} \sum_{i=0}^{m_1-1} \frac{(\frac{xyN_j^2\beta_1}{I(1-x\kappa_j^2)})^i}{i!}\big) dy \\ &= \frac{\Gamma(m_2, \frac{I\beta_2}{P_j})}{\Gamma(m_2)} - \int_{\frac{I}{P_j}}^{\infty} \frac{\beta_2^{m_2}}{\Gamma(m_2)} y^{m_2-1} e^{-\beta_2 y} e^{-\frac{xyN_j^2\beta_1}{I(1-x\kappa_j^2)}} \sum_{i=0}^{m_1-1} \frac{(\frac{xyN_j^2\beta_1}{I(1-x\kappa_j^2)})^i}{i!}.\end{aligned} \tag{A.6}$$

By solving the above integral and by doing some algebraic simplification we get the following expression below

$$\begin{aligned}\Lambda_2 &= \frac{\Gamma(m_2, \frac{I\beta_2}{P_j})}{\Gamma(m_2)} - \frac{\beta_2^{m_2}}{\Gamma(m_2)} \sum_{i=0}^{m_1-1} \frac{(\frac{x\beta_1 N_j^2}{I(1-x\kappa_j^2)})^i}{i!} \int_{\frac{I}{P_j}}^{\infty} y^{m_2-1+i} e^{-(\beta_2 + \frac{x\beta_1 N_j^2}{I(1-x\kappa_j^2)})y} dy \\ &= \frac{\Gamma(m_2, \frac{I\beta_2}{P_j})}{\Gamma(m_2)} - \frac{\beta_2^{m_2}}{\Gamma(m_2)} \sum_{i=0}^{m_1-1} \frac{(\frac{x\beta_1 N_0^2}{I(1-x\kappa^2)})^i}{i!} \Gamma\left(m_2 + i, (\beta_2 + \frac{x\beta_1 N_0^2}{I(1-x\kappa^2)})\frac{I}{P}\right) \\ &\quad \times \left(\beta_2 + \frac{x\beta_1 N_0^2}{I(1-x\kappa^2)}\right)^{-m_2-i}.\end{aligned} \tag{A.7}$$

Finally, by adding the Λ_1 and the Λ_2 components in (A.3) and (A.7), we obtain the CDF of RV T_j yielded in (3.8).

Appendix B

Appendix for Chapter 4

B.1 Derivation of the Moments for Weibull Summands

Closed-form expressions for evaluating the exact moments of $\alpha - \mu$ distribution $\mathbb{E}[\Lambda]$, $\mathbb{E}[\Lambda^2]$, and $\mathbb{E}[\Lambda^4]$ will be discussed in this section. By using (4.13) and (4.14), $\mathbb{E}[\Lambda]$ can be calculated as

$$\begin{aligned}
\mathbb{E}[\Lambda] = &\binom{1}{0}\binom{0}{0}\cdots\binom{0}{0}\mathbb{E}[\Lambda_1^1]\mathbb{E}[\Lambda_2^0]...\mathbb{E}[\Lambda_N^0] \\
&+\binom{1}{1}\binom{1}{0}\cdots\binom{0}{0}\mathbb{E}[\Lambda_1^0]\mathbb{E}[\Lambda_2^1]...\mathbb{E}[\Lambda_N^0] \\
&+\binom{1}{1}\binom{1}{1}\binom{1}{0}\cdots\binom{0}{0}\mathbb{E}[\Lambda_1^0]\mathbb{E}[\Lambda_2^0]\mathbb{E}[\Lambda_3^0]...\mathbb{E}[\Lambda_N^0] \\
&+\binom{1}{1}\binom{1}{1}\cdots\binom{1}{1}\mathbb{E}[\Lambda_1^0]\mathbb{E}[\Lambda_2^0]...\mathbb{E}[\Lambda_N^1] \\
&= \mathbb{E}[\Lambda_1^1] + \mathbb{E}[\Lambda_2^1] + \mathbb{E}[\Lambda_3^1] + \cdots \mathbb{E}[\Lambda_N^1] \\
&= \Phi^{\frac{1}{\beta}}\Gamma(1+\frac{1}{\beta}) + \Phi^{\frac{1}{\beta}}\Gamma(1+\frac{1}{\beta}) + \cdots + \Phi^{\frac{1}{\beta}}\Gamma(1+\frac{1}{\beta}) \\
&= N\Phi^{\frac{1}{\beta}}\Gamma\Big(1+\frac{1}{\beta}\Big).
\end{aligned} \tag{B.1}$$

The order two moment of $\alpha - \mu$ distribution is given by

$$
\begin{aligned}
\mathbb{E}[\Lambda^2] = & \sum_{n_1=0}^{2} \sum_{n_2=0}^{n_1} \cdots \sum_{n_{N-1}=0}^{n_{N-2}} \binom{2}{n_1} \binom{n_1}{n_2} \cdots \binom{n_{N-2}}{n_{N-1}} \\
& \times \mathbb{E}[\Lambda_1^{2-n_1}] \mathbb{E}[\Lambda_2^{n_1-n_2}] \cdots \mathbb{E}[\Lambda_N^{n_{N-1}}] \\
= & \begin{pmatrix} 2 \\ 0 \end{pmatrix} \begin{pmatrix} 0 \\ 0 \end{pmatrix} \cdots \begin{pmatrix} 0 \\ 0 \end{pmatrix} \begin{pmatrix} 0 \\ 0 \end{pmatrix} \mathbb{E}[\Lambda_1^2] \mathbb{E}[\Lambda_2^0] ... \mathbb{E}[\Lambda_{N-1}^0] \mathbb{E}[\Lambda_N^0] \\
& + \begin{pmatrix} 2 \\ 1 \end{pmatrix} \begin{pmatrix} 1 \\ 0 \end{pmatrix} \cdots \begin{pmatrix} 0 \\ 0 \end{pmatrix} \begin{pmatrix} 0 \\ 0 \end{pmatrix} \mathbb{E}[\Lambda_1^1] \mathbb{E}[\Lambda_2^1] ... \mathbb{E}[\Lambda_{N-1}^0] \mathbb{E}[\Lambda_N^1] \\
& \cdots \\
& + \begin{pmatrix} 2 \\ 2 \end{pmatrix} \begin{pmatrix} 2 \\ 2 \end{pmatrix} \cdots \begin{pmatrix} 2 \\ 2 \end{pmatrix} \begin{pmatrix} 2 \\ 1 \end{pmatrix} \mathbb{E}[\Lambda_1^0] \mathbb{E}[\Lambda_2^0] ... \mathbb{E}[\Lambda_{N-1}^1] \mathbb{E}[\Lambda_N^1] \\
& + \begin{pmatrix} 2 \\ 2 \end{pmatrix} \begin{pmatrix} 2 \\ 2 \end{pmatrix} \cdots \begin{pmatrix} 2 \\ 2 \end{pmatrix} \begin{pmatrix} 2 \\ 2 \end{pmatrix} \mathbb{E}[\Lambda_1^0] \mathbb{E}[\Lambda_2^0] ... \mathbb{E}[\Lambda_{N-1}^0] \mathbb{E}[\Lambda_N^2] \\
= & \mathbb{E}[\Lambda_1^1] + 2\mathbb{E}[\Lambda_1^1] \mathbb{E}[\Lambda_2^1] + 2\mathbb{E}[\Lambda_1^1] \mathbb{E}[\Lambda_3^1] + ... + 2\mathbb{E}[\Lambda_1^1] \\
& \times \mathbb{E}[\Lambda_{N-1}^1] + 2\mathbb{E}[\Lambda_1^1] \mathbb{E}[\Lambda_N^1] + \mathbb{E}[\Lambda_2^2] + 2\mathbb{E}[\Lambda_2^1] \mathbb{E}[\Lambda_3^1] \\
& + ...2\mathbb{E}[\Lambda_2^1] \mathbb{E}[\Lambda_N^1] + \mathbb{E}[\Lambda_3^2] + 2\mathbb{E}[\Lambda_3^1] \mathbb{E}[\Lambda_N^1] \\
& + ... + \mathbb{E}[\Lambda_{N-1}^2] + 2\mathbb{E}[\Lambda_{N-1}^1] E[\Lambda_N^1] + \mathbb{E}[\Lambda_N^2]. \qquad \text{(B.2)}
\end{aligned}
$$

By further expanding $\mathbb{E}[\Lambda_i^n]$ terms, we get the closed-form solution for $\mathbb{E}[\Lambda^2]$ given in (4.16).

Similarly, we show derivation of $\mathbb{E}[\Lambda^4]$ for $n = 4$ by referring to (4.13)

$$\begin{aligned}
\mathbb{E}[\Lambda^4] =& \binom{4}{0}\binom{0}{0}\dots\binom{0}{0}\binom{0}{0}\mathbb{E}[\Lambda_1^4]\mathbb{E}[\Lambda_2^0]...\mathbb{E}[\Lambda_{N-1}^0] \\
&\times \mathbb{E}[\Lambda_N^0] + \binom{4}{1}\binom{1}{1}\dots\binom{0}{0}\binom{0}{0}\mathbb{E}[\Lambda_1^3]\mathbb{E}[\Lambda_2^1]...\mathbb{E}[\Lambda_{N-1}^0] \\
&\times \mathbb{E}[\Lambda_N^0]\cdots \\
&+ \binom{4}{1}\binom{1}{1}\dots\binom{1}{1}\binom{1}{1}\mathbb{E}[\Lambda_1^3]\mathbb{E}[\Lambda_2^0]...\mathbb{E}[\Lambda_{N-1}^0]\mathbb{E}[\Lambda_N^0]... \\
&\dots \\
&+ \binom{4}{4}\binom{4}{4}\dots\binom{4}{4}\binom{4}{4}\mathbb{E}[\Lambda_1^0]\mathbb{E}[\Lambda_2^0]...\mathbb{E}[\Lambda_{N-1}^0]\mathbb{E}[\Lambda_N^4] \\
=&\mathbb{E}[\Lambda_1^4] + 4\mathbb{E}[\Lambda_1^3]\mathbb{E}[\Lambda_2^1] + 4\mathbb{E}[\Lambda_1^3]\mathbb{E}[\Lambda_3^1] + ... + 4\mathbb{E}[\Lambda_1^3] \\
&\times \mathbb{E}[\Lambda_N^1] + \mathbb{E}[\Lambda_2^1]\mathbb{E}[\Lambda_2^2] + 12\mathbb{E}[\Lambda_1^2]\mathbb{E}[\Lambda_2^1]\mathbb{E}[\Lambda_3^1] + ... \\
&+ 12\mathbb{E}[\Lambda_1^2]\mathbb{E}[\Lambda_2^1]\mathbb{E}[\Lambda_N^1] + 6\mathbb{E}[\Lambda_1^2]\mathbb{E}[\Lambda_3^2] + 12\mathbb{E}[\Lambda_1^2] \\
&\times \mathbb{E}[\Lambda_3^1]\mathbb{E}[\Lambda_4^1]... + 12\mathbb{E}[\Lambda_1^2]\mathbb{E}[\Lambda_3^1]\mathbb{E}[\Lambda_N^1]... \\
&\dots \\
&+ 4\mathbb{E}[\Lambda_2^1]\mathbb{E}[\Lambda_N^3] + \mathbb{E}[\Lambda_3^4] + ... + \mathbb{E}[\Lambda_N^4].
\end{aligned} \tag{B.3}$$

We partially represent Weibull summand terms of $E[\Lambda^4]$ in (B.3). After some algebraic manipulations and expanding Weibull moment terms we get the final closed-form expression for the fourth order $\alpha - \mu$ distribution given in (4.17).

B.2 Calculation of the AUC over AWGN Channel

Derivation of the AUC over AWGN channel in [69] is given by

$$A(\gamma) = \int_0^1 P_D(P_F)dP_F. \tag{B.4}$$

P_F is a function of γ_{th}, therefore the variable of integration is changed, which results in

$$A(\gamma) = \int_{\infty}^{0} P_D(\gamma, \gamma_{th}) \frac{dP_F(\gamma_{th})}{\gamma_{th}} d\gamma_{th}, \tag{B.5}$$

where limits of integration are found as $\gamma_{th} = \infty \rightarrow \Gamma(\mu_0, \infty) = 0 \rightarrow P_F(\gamma_{th}) = 0$ and $\gamma_{th} = 0 \rightarrow \Gamma(\mu_0, 0) = \Gamma(\mu_0) \rightarrow P_F(\gamma_{th}) = 1$. We expand the $\dfrac{dP_F(\gamma_{th})}{d\gamma_{th}}$ term as

$$\begin{aligned} \frac{dP_F(\gamma_{th})}{d\gamma_{th}} &= \frac{1}{\Gamma(\mu_0)} \frac{d}{d\gamma_{th}} (\Gamma(\mu_0, \psi_0)) \\ &= \frac{1}{\Gamma(\mu_0)} \frac{d}{d\gamma_{th}} \int_{\psi_0}^{\infty} t^{\mu_0 - 1} e^{-t} dt. \end{aligned} \tag{B.6}$$

We evaluate Ω_0 and Ω_1 by using (4.18). Next, with the aid of $\psi_0 = \frac{\mu_0 \gamma_{th}^{\alpha_0}}{\Omega_0}$ and the Leibniz rule, we get

$$\begin{aligned} &\frac{d}{d\gamma_{th}} \int_{\frac{\mu_0 \gamma_{th}^{\alpha_0}}{\Omega_0}}^{\infty} t^{\mu_0 - 1} e^{-t} dt = t^{\mu_0 - 1} e^{-t} \big|_{t=\infty} \\ &- t^{\mu_0 - 1} e^{-t} \big|_{t=\frac{\mu_0 \gamma_{th}^{\alpha_0}}{\Omega_0}} \frac{\alpha_0 \mu_0 \gamma_{th}^{\alpha_0 - 1}}{\Omega_0} + \int_{\frac{\mu_0 \gamma_{th}^{\alpha_0}}{\Omega_0}}^{\infty} \frac{d}{d\gamma_{th}} (t^{\mu_0 - 1} e^{-t}) dt. \end{aligned} \tag{B.7}$$

Now, by substituting (4.20) and (D.2) into (B.5) and using [68, eq. (6.455)], we get

$$A(\gamma) = \int_{0}^{\infty} \frac{\Gamma(\mu_1, \frac{\mu_1 \gamma_{th}^{\alpha_1}}{\Omega_1})}{\Gamma(\mu_1)\Gamma(\mu_0)} \frac{\alpha_0}{\gamma_{th}} \left(\frac{\mu_0 \gamma_{th}^{\alpha_0}}{\Omega_0}\right)^{\mu_0} \exp\left(-\frac{\mu_0 \gamma_{th}^{\alpha_0}}{\Omega_0}\right) d\gamma_{th}, \tag{B.8}$$

where limits of integration where switched by minus sign. The following substitutions $\alpha_1 = \alpha_0 = \alpha$ and the change of variables $\gamma_{th}^{\alpha} = s$, $d\gamma_{th} = \frac{1}{\alpha} s^{(\frac{1}{\alpha} - 1)} ds$, as well as Ω_1 and Ω_0 parameters expansions in (B.8) lead to the final expression given in (4.24).

B.3 Derivation of $\bar{P}_{D\mathrm{Nak}}^{\mathrm{id}}$ over Nakagami-m Fading Channels

Derivation of the average detection probability $\bar{P}_{D\mathrm{Nak}}^{\mathrm{id}}$ over Nakagami-m fading for ideal system model is shown as

$$\begin{aligned}\bar{P}_{D\mathrm{Nak}}^{\mathrm{id}} &= \epsilon \int_0^{\infty} \gamma^{m-1} e^{-\frac{\gamma m}{\bar{\gamma}}} \left(\Gamma(\mu_1) - \sum_{n=0}^{\infty} \frac{(-1)^n \psi_1^{\mu_1+n}}{n!(\mu_1+n)(\gamma+1)^{\frac{\alpha_1(\mu_1+n)}{\beta}}}\right) d\gamma \\ &= \underbrace{\epsilon\Gamma(\mu_1) \int_0^{\infty} \gamma^{m-1} e^{-\frac{\gamma m}{\bar{\gamma}}} d\gamma}_{\mathrm{C1}} - \underbrace{\epsilon \sum_{n=0}^{\infty} \frac{(-1)^n \psi_1^{\mu_1+n}}{n!(\mu_1+n)} \int_0^{\infty} \gamma^{m-1} e^{-\frac{\gamma m}{\bar{\gamma}}} \left(\frac{1}{\gamma+1}\right)^{\frac{\alpha_1(\mu_1+n)}{\beta}} d\gamma}_{\mathrm{C2}}.\end{aligned} \tag{B.9}$$

By using (4.28), integral of the $C1$ term is found as

$$C1 = \epsilon\Gamma(\mu_1)\Gamma(m) \left(\frac{m}{\bar{\gamma}}\right)^{-m} = 1, \tag{B.10}$$

where $m > 0$ and $\frac{m}{\bar{\gamma}} > 0$. By making use of the power of binomials in [68, eq. (1.110)], we represent power of the ratio as the summation terms given as

$$\left(\frac{1}{\gamma+1}\right)^s = \left(1 - \frac{\gamma}{\gamma+1}\right)^s = \sum_{j=0}^{\infty} \binom{s}{j} (-1)^j \left(\frac{\gamma}{\gamma+1}\right)^j, \tag{B.11}$$

where $\left(1 - \frac{\gamma}{\gamma+1}\right) < 1$ and $s = \frac{\alpha_1(\mu_1+n)}{\beta}$. Next, the integral of the $C2$ term in (B.9) is evaluated as

$$C2 = \epsilon \sum_{n=0}^{\infty} \sum_{j=0}^{\infty} \frac{(-1)^n (-1)^j}{n!(\mu_1+n)} \psi_1^{\mu_1+n} \binom{s}{j} \underbrace{\int_0^{\infty} \gamma^{m+j-1} e^{-\frac{\gamma m}{\bar{\gamma}}} \frac{1}{(1+\gamma)^j} d\gamma}_{\mathrm{C3}}, \tag{B.12}$$

where we evaluate $C3$ as

$$\begin{aligned} C3 &= \int_0^\infty \gamma^{m+j-1} e^{-\frac{\gamma m}{\bar{\gamma}}} \frac{1}{(1+\gamma)^j} d\gamma \\ &= \int_0^\infty \sum_{k=0}^{m+j-1} \binom{m+j-1}{k} (1+\gamma)^{m+j-1-k} (-1)^k e^{-\frac{\gamma m}{\bar{\gamma}}} \frac{1}{(\gamma+1)^j} d\gamma \\ &= \sum_{k=0}^{m+j-1} \binom{m+j-1}{k} (-1)^k \underbrace{\int_0^\infty (\gamma+1)^{m-1-k} e^{-\frac{\gamma m}{\bar{\gamma}}} d\gamma}_{\text{C4}} . \end{aligned} \tag{B.13}$$

Now by using the change of variables and limits of the integral in (B.13) as $\gamma + 1 = s$ and $\gamma = 0 \Rightarrow s = 1$ and $\gamma = \infty \Rightarrow s = \infty$, we get the following integral

$$C4 = \int_0^\infty \left(s\frac{m}{\bar{\gamma}}\right)^{m-1-k} e^{-\frac{sm}{\bar{\gamma}}} d(s\frac{m}{\bar{\gamma}})(\frac{m}{\bar{\gamma}})^{k-m}. \tag{B.14}$$

Next, we take another turn of variable and limit change of the integral in (B.14) as $\frac{sm}{\bar{\gamma}} = z$, $s = 1 \Rightarrow z = \frac{m}{\bar{\gamma}}$ and $s = \infty \Rightarrow z = \infty$. Hence, we get the following expression

$$C4 = \left(\frac{m}{\bar{\gamma}}\right)^{k-m} \int_{\frac{m}{\bar{\gamma}}}^\infty z^{m-1-k} e^{-z} dz = \left(\frac{m}{\bar{\gamma}}\right)^{k-m} \Gamma\left(m-k, \frac{m}{\bar{\gamma}}\right). \tag{B.15}$$

Final solution for the P_{DNak}^{id} is found by placing the $C3$ term into the $C2$ term and displayed in (4.27).

B.4 Derivation of $\bar{P}_{DNak}^{\text{hi}}$ at Non-ideal System Model

Calculation of the average detection probability for the ideal system model over Nakagami-m fading channel was presented in Section B.3. Similar approach is used to derive the average detection probability over Nakagami-m fading channel for hardware impaired system model. Instead of γ in (B.9) we replace SNDR, γ_{hi}, given in (4.2) and calculate the average detection probability, $\bar{P}_{DNak}^{\text{hi}}$, as

$$\bar{P}_{D\text{Nak}}^{\text{hi}} = \epsilon \int_0^\infty \gamma^{m-1} e^{-\frac{\gamma m}{\bar{\gamma}}} \Big(\Gamma(\mu_1) - \sum_{n=0}^{\infty} \frac{(-1)^n \psi_1^{\mu_1+n}}{n!(\mu_1+n)(\frac{\gamma}{k^2\gamma+1}+1)^{\frac{\alpha_1(\mu_1+n)}{\beta}}} \Big) d\gamma$$

$$= \underbrace{\epsilon\Gamma(\mu_1) \int_0^\infty \gamma^{m-1} e^{-\frac{\gamma m}{\bar{\gamma}}} d\gamma}_{\text{D1}} - \underbrace{\epsilon \sum_{n=0}^{\infty} \frac{(-1)^n \psi_1^{\mu_1+n}}{n!(\mu_1+n)} \int_0^\infty \gamma^{m-1} e^{-\frac{\gamma m}{\bar{\gamma}}} \underbrace{\Big(\frac{1}{\frac{\gamma}{k^2\gamma+1}}+1\Big)^{\frac{\alpha_1(\mu_1+n)}{\beta}}}_{D3} d\gamma}_{D2}, \tag{B.16}$$

where the integral of the $D1$ term is shown in (B.10). By using [68, eq. (1.110)], we expand and calculate the $D3$ term as

$$D3 = \Big(\frac{1}{\frac{\gamma}{k^2\gamma+1}}+1\Big)^{\frac{\alpha_1(\mu_1+n)}{\beta}} = \Big(1 - \frac{\gamma}{\gamma+\gamma\kappa^2+1}\Big)^{\frac{\alpha_1(\mu_1+n)}{\beta}}$$
$$= \sum_{j=0}^{\infty} \binom{\frac{\alpha_1(\mu_1+n)}{\beta}}{j} \Big(-\frac{\gamma}{\gamma+\gamma\kappa^2+1}\Big)^j. \tag{B.17}$$

Hence, the integral of the $D2$ term is found as follows

$$D2 = \epsilon \sum_{n=0}^{\infty} \sum_{j=0}^{\infty} \frac{(-1)^n (-1)^j \psi_1^{\mu_1+n}}{n!(\mu_1+n)} \binom{\frac{2}{\beta}(\mu_1+n)}{j}$$
$$\times \underbrace{\int_0^\infty \underbrace{\gamma^{m+j-1}}_{\text{D5}} e^{-\frac{m\gamma}{\bar{\gamma}}} \frac{1}{(\gamma(1+k^2)+1)^j} d\gamma}_{\text{D4}}. \tag{B.18}$$

Next, we evaluate the integral given in (B.18) with the following conversion of the $D5 = \gamma^{m+j-1} = \frac{(\gamma\tau)^{m+j-1}}{\tau^{m+j-1}} = \frac{(\gamma\tau+1-1)^{m+j-1}}{\tau^{m+j-1}}$ and $\tau = 1+\kappa^2$. By using the power of binomials, the $D5$ term is expressed as

$$D5 = \tau^{-j-m+1} \sum_{t=0}^{j+m-1} (-1)^t \binom{j+m-1}{t} (\tau\gamma+1)^{m+j-1-t}. \tag{B.19}$$

Hence, the integral of the $D4$ term can be evaluated as

$$\begin{aligned} D4 = &\int_0^\infty \exp\left(-\frac{m(\gamma\tau+1}{\bar{\gamma}\tau}\right)\exp\left(\frac{m}{\bar{\gamma}\tau}\right)\frac{1}{(\gamma\tau+1)^j} \\ &\times \frac{1}{\tau^{j+m-1}}\sum_{t=0}^{j+m-1}(-1)^t\binom{j+m-1}{t}\left(\frac{m}{\tau\bar{\gamma}}\right)^{t-m} \\ =&\frac{\exp\left(\frac{m}{\bar{\gamma}\tau}\right)}{\tau^{m+j-1}}\sum_{t=0}^{j+m-1}\binom{j+m-1}{t}(-1)^t \\ &\times \int_0^\infty \underbrace{\exp\left(-\frac{m(\gamma\tau+1)}{\bar{\gamma}\tau}\right)(\gamma\tau+1)^{m-t-1}\,d\gamma}_{\text{D6}}. \end{aligned} \tag{B.20}$$

In order to solve the above integral in (B.20), we used the variable and limit change as $s = \gamma\tau + 1$, $\gamma = 0 \Rightarrow s = 1$ and $\gamma = \infty \Rightarrow s = \infty$ and present the integral as

$$D6 = \frac{1}{\tau}\int_1^\infty \left(\frac{ms}{\bar{\gamma}\tau}\right)^{m-t-1}\exp\left(-\frac{ms}{\bar{\gamma}\tau}\right)\left(\frac{m}{\bar{\gamma}\tau}\right)^{t-m} d\left(\frac{ms}{\bar{\gamma}\tau}\right). \tag{B.21}$$

Next, we change the integral variables of the (B.21) as $z = \frac{ms}{\bar{\gamma}\tau}$, and exchange the limits as $s = 1 \Rightarrow z = \frac{m}{\bar{\gamma}\tau}$ and $s = \infty \Rightarrow z = \infty$, and finally solve the integral as

$$\begin{aligned} D6 &= \frac{1}{\tau}\int_{\frac{m}{\bar{\gamma}\tau}}^\infty z^{m-t-1}e^{-z}dz\left(\frac{m}{\bar{\gamma}\tau}\right)^{t-m} \\ &= \frac{1}{\tau}\Gamma\left(m-t, \frac{m}{\tau\bar{\gamma}}\right)\left(\frac{m}{\tau\bar{\gamma}}\right)^{t-m}. \end{aligned} \tag{B.22}$$

Now, by placing the $D4$ and the $D5$ terms into the $D2$ term, we get the final expression that represents $\bar{P}_{DNak}^{\text{hi}}$ given in (4.29).

Appendix C

Appendix for Chapter 5

C.1 Proof of Proposition 1

In this section, we present derivation details for calculating the outage probability given in (5.9). The outage probablity is evaluated as

$$\begin{aligned} P_{\text{out}}(\gamma_{th}) &= \Pr\left(\frac{aX}{bX+Z+1} < \gamma_{th}\right) \\ &= \begin{cases} \int_0^\infty F_X\left(\frac{\gamma_{th}(1+z)}{a-\gamma_{th}b}\right) f_Z(z)dz, 0 \le \gamma_{th} < \frac{a}{b} \\ 1, \quad \gamma_{th} \ge \frac{a}{b}, \end{cases} \end{aligned} \tag{C.1}$$

where the expression for $f_Z(z)$ is given in (5.5) and the CDF of Gamma distribution is given as $F_X(x) = \frac{\gamma(m,\frac{x}{\beta})}{\Gamma(m)}$, which could be expressed as in [68, Eq. 8.354.1]

$$F_X(x) = \frac{1}{\Gamma(m)} \sum_0^\infty \frac{(-1)^n \left(\frac{x}{\beta}\right)^{m+n}}{n!(m+n)}. \tag{C.2}$$

By using (C.2), the outage probability is calculated as

$$\begin{aligned} P_{\text{out}}(\gamma_{th}) &= \int_0^{\infty} F_X\left(\phi_1+\phi_2 z\right)\Phi\sum_{k=0}^{\infty}\frac{\delta_{k+1}z^{\rho+k-1}e^{-\frac{z}{\beta_1}}}{\Gamma(\rho+k)\beta_1^{\rho+k}}dz \\ &= \int_0^{\infty}\frac{\Phi}{\Gamma(m)}\sum_{n=0}^{\infty}\frac{(-1)^n(\frac{\phi_1+\phi_2 z}{\beta})^{m+n}}{n!(m+n)}\sum_{k=0}^{\infty}\frac{\delta_{k+1}z^{\rho+k-1}e^{-\frac{z}{\beta_1}}}{\Gamma(\rho+k)\beta_1^{\rho+k}}dz \\ &= \frac{\Phi}{\Gamma(m)}\sum_{n=0}^{\infty}\frac{(-1)^n}{n!(m+n)}\sum_{k=0}^{\infty}\frac{\delta_{k+1}}{\Gamma(\rho+k)\beta_1^{\rho+k}}\underbrace{\int_0^{\infty}\underbrace{\left(\frac{\phi_1+\phi_2 z}{\beta}\right)^{m+n}}_{A_1}z^{\rho+k-1}e^{-\frac{z}{\beta_1}}dz}_{A_2}, \end{aligned} \tag{C.3}$$

where $\phi_1+\phi_2 z$ denotes $\frac{\gamma_{th}(1+z)}{a-\gamma_{th}b}$ for simplicity. Next, the A_1 term is expanded by using the power of binomials given in [68, Eq. 1.111] as

$$A_1 = \left(\frac{\phi_1+\phi_2 z}{\beta}\right)^{m+n} = \left(\frac{1}{\beta}\right)^{m+n}\sum_{t=0}^{m+n}\binom{m+n}{t}(\phi_2 z)^t\phi_1^{m+n-t}. \tag{C.4}$$

In the following step, we evaluate the integral of the A_2 term as below

$$A_2 = \nu\int_0^{\infty}(\phi_2 z)^t z^{\rho+k-1}e^{-\frac{z}{\beta_1}}dz = \nu\phi_2^t\beta_1^{k+\rho+t}\Gamma[k+\rho+t], \tag{C.5}$$

where $\nu = \left(\frac{1}{\beta}\right)^{m+n}\sum_{t=0}^{m+n}\binom{m+n}{t}\phi_1^{m+n-t}$, $\beta_1>0$ and $(k+p+t)>0$. Finally, by combining the A_1 and A_2 terms together we display the final expression for the outage probability $P_{\text{out}}(\gamma_{th})$ in (5.9).

C.2 Proof of Proposition 2

The ergodic capacity in (5.18) can be rewritten as

$$C^{\text{Nak}} = \mathbb{E}\left\{\log_2\left(\frac{1+Y+(a+b)X}{1+Y+bX}\right)\right\}. \tag{C.6}$$

Let us represent the sum of Y and $(a+b)X$ RVs as $W = Y + (a+b)X$ and as well as the sum of Y and bX RVs as $Z = Y + bX$. Hence, we may present C^{Nak} given in (5.18) as

$$\begin{aligned} C^{\text{Nak}} =& \mathbb{E}\{\log_2(W+1) - \log_2(Z+1)\} \\ =& \underbrace{\int_0^\infty \log_2(w+1) f_W(w) dw}_{A_1} - \underbrace{\int_0^\infty \log_2(z+1) f_Z(z) dz}_{A_2}. \end{aligned} \tag{C.7}$$

By using [68, Eq. 4.222.8] and the PDF of W RV in (5.5), we evaluate A_1 integral as

$$\begin{aligned} A_1 =& \sum_{k=0}^{\infty} \frac{\Phi_w \delta_k}{\ln(2)\Gamma(\rho_w + k)} \sum_{r=0}^{\xi_1} \frac{(\xi_1)!}{(\xi_1 - r)!} \\ &\times \left(\frac{(-1)^{\xi_1 - r - 1} e^{\frac{1}{\beta_{0w}}} Ei(-\frac{1}{\beta_{0w}})}{\beta_{0w}^{\xi_1 - r}} + \sum_{i=1}^{\xi_1 - r} \frac{(i-1)!}{(-\beta_{0w})^{\xi_1 - r - i}} \right), \end{aligned} \tag{C.8}$$

where $\xi_1 = \rho_w + k - 1$ and $Ei(\cdot)$ is exponential integral function defined in [68, Eq. 8.212.2]. Similar to A_1 we calculate A_2 as

$$\begin{aligned} A_2 =& \sum_{t=0}^{\infty} \frac{\Phi_z \delta_t}{\ln(2)\Gamma(\rho_z + t)} \sum_{n=0}^{\xi_2} \frac{(\xi_2)!}{(\xi_2 - n)!} \\ &\times \left(\frac{(-1)^{\xi_2 - n - 1} e^{\frac{1}{\beta_{0z}}} Ei(-\frac{1}{\beta_{0z}})}{\beta_{0z}^{\xi_2 - n}} + \sum_{j=1}^{\xi_2 - n} \frac{(j-1)!}{(-\beta_{0z})^{\xi_2 - n - j}} \right), \end{aligned} \tag{C.9}$$

where $\xi_2 = \rho_z + t - 1$. By using (C.8) and (C.9), we present the final expression for the ergodic capacity in (5.21).

C.3 Proof of Proposition 3

According to (5.19), we need to calculate $\mathbb{E}\{\ln(aX)\}$ and $\mathbb{E}\{\ln(1+Y+bX)\}$ to find the lower ergodic capacity. Note that we denote $Z = Y + bX$ as in Proposition C.2 and evaluate $\mathbb{E}\{\ln(1+Z)\}$ similarly to Eq. (C.9). Moreover, $\mathbb{E}\{\ln(aX)\}$ calculation is given

as

$$\mathbb{E}\{\ln(aX)\} = \ln(a) + \underbrace{\int_0^\infty \ln(x) f_X(x) dx}_{B_1}, \tag{C.10}$$

where

$$f_X(x) = \frac{1}{\Gamma(m)\beta^m} x^{m-1} e^{-\frac{x}{\beta}}. \tag{C.11}$$

Hence, we calculate B_1 by using [68, (Eq. 4.352.1)] as following

$$B_1 = \frac{1}{\Gamma(m)\beta^m} \int_0^\infty x^{m-1} e^{-\frac{x}{\beta}} \ln(x) dx = \frac{\psi(m) - \ln(\frac{1}{\beta})}{\Gamma(m)\beta^m}, \tag{C.12}$$

where $\psi(\cdot)$ is the Euler psi function. Furthermore, by using (5.19), we obtain the final expression for the lower ergodic capacity displayed in (5.23).

C.4 Proof of Proposition 4

The ergodic capacity upper bound expression in (5.20) can be approximated by $\log_2\left(1 + a\mathbb{E}\{X\}\,\mathbb{E}\left\{\frac{1}{1+Z}\right\}\right)$, where $Z = bX + Y$. We need to calculate $\mathbb{E}\{X\} = \int_0^\infty f_X(x) x dx$ and $\mathbb{E}\{\frac{1}{1+Z}\} = \int_0^\infty \frac{1}{z+1} f_Z(z) dz$, where $f_X(x)$ is defined in (C.11) and $f_Z(z)$ is given in (5.5). Thus, we have

$$\mathbb{E}\{X\} = \frac{1}{\Gamma(m)\beta^m} \int_0^\infty x^{m-1} x e^{-\frac{x}{\beta}} dx = \frac{\beta\Gamma(1+m)}{\Gamma(m)}. \tag{C.13}$$

Similarly, expected value for the inverse summation of $N+1$ i.n.i.d. gamma variables is found by using [104, Eq. 2.3.6.13] as below

$$\begin{aligned}\mathbb{E}\left\{\frac{1}{Z+1}\right\} &= \sum_{t=0}^{\infty} \frac{\Phi_z\,\delta_t}{\Gamma(\rho_z+t)\beta_{0z}^{\rho_z+t}} \int_0^\infty \frac{z^{\rho_z+t-1}}{z+1} e^{-\frac{z}{\beta_{0z}}} dz \\ &= \sum_{t=0}^{\infty} \frac{\Phi_z\,\delta_t}{\Gamma(\rho_z+t)\beta_{0z}^{\rho_z+t}} e^{\frac{1}{\beta_{0z}}} \Gamma(t+\rho_z)\Gamma(t+\rho_z, \frac{1}{\beta_{0z}}).\end{aligned} \tag{C.14}$$

Now, by using equations (5.20), (C.13), and (C.14), we obtain the upper bound for ergodic capacity displayed in (5.25).

Appendix D

Appendix for Chapter 6

D.1 Proof of Proposition 6

The ergodic capacity for the proposed system model is is evaluated as follows

$$C = \underbrace{\int_0^\infty \log_2(1+(a+b+c)y) f_Y(y) dy}_{A_1} - \underbrace{\int_0^\infty \log_2(1+(b+c)y) f_Y(y) dy}_{A_2}. \tag{D.1}$$

We evaluate A_1 integral by using (6.8) and change of variables $\frac{y}{\beta} = z$ and $dy = \beta dz$ as

$$A_1 = \frac{1}{\Gamma(mN_s)} \int_0^\infty \log_2(1+(a+b+c)\beta z) z^{mN_s-1} e^{-z} dz. \tag{D.2}$$

Next, by applying [68, Eq 4.222.8], we solve the integral in (D.2) as

$$\begin{aligned} A_1 = & \frac{1}{\Gamma(mN_s)\ln(2)} \sum_{i=0}^{mN_s-1} \frac{(mN_s-1)!}{(mN_s-1-i)!} \left(\frac{(-1)^{mN_s-i-2} e^{\frac{1}{(a+b+c)\beta}}}{((a+b+c)\beta)^{mN_s}-1-i} \right. \\ & \left. \times Ei(-\frac{1}{(a+b+c)\beta}) + \sum_{k=1}^{mN_s-1-i} \frac{(k-1)!}{(-(a+b+c)\beta)^{mN_s-1-i-k}} \right), \end{aligned} \tag{D.3}$$

where $m-1>0$. Similarly, we calculate A_2 integral in (D.1) and present the final expression for the ergodic capacity in (6.12).

D.2 Proof of Proposition 7

A lower bound for the ergodic capacity is evaluated by using (6.13) as

$$C_l^{\text{Nak}} = \log_2\left(1+\exp\left(\underbrace{\int_0^\infty \ln(ay) f_Y(y)dy}_{B_1} - \underbrace{\int_0^\infty \ln((b+c)y+1) f_Y(y)dy}_{B_2}\right)\right). \tag{D.4}$$

By using [68, Eq. 4.352.1], we evaluate the integral in B_1 as

$$\begin{aligned} B_1 &= \frac{1}{\Gamma(mN_s)\beta^{mN_s}} \int_0^\infty \ln(ay) y^{mN_s-1} e^{\frac{y}{\beta}} dy \\ &= \ln(a) + \psi(mN_s) - \ln(\frac{1}{\beta}). \end{aligned} \tag{D.5}$$

Furthermore, we evaluate B_2 integral by using [68, Eq 4.222.8] as

$$\begin{aligned} B_2 &= \frac{1}{\Gamma(mN_s)\beta^{mN_s}} \int_0^\infty \ln((b+c)y+1) y^{mN_s-1} e^{\frac{y}{\beta}} dy \\ &= \ln(1+(b+c)mN_s\beta). \end{aligned} \tag{D.6}$$

Finally, by using B_1 and B_2 integral evaluations and (D.4), we present a lower bound for the ergodic capacity in (6.14).

Bibliography

[1] N. Tesla and J. T. Ratzlaff, *Tesla Said*. Millbrae, California, USA: Tesla Book Company, 1984.

[2] ITU. (2008) Number of active mobile broadband subscriptions worldwide from 2007 to 2018 (in millions). [Online]. Available: https://www.statista.com/statistics/273016/number-of-mobile-broadband-subscriptions-worldwide-since-2007

[3] In Statista - The Statistics Portal. (2019) Number of wireless subscriptions by generation worldwide from 2010 to 2023 (in millions). Accessed June 21. [Online]. Available: https://www.statista.com/statistics/858244/subscriptions-to-wireless-services-worldwide-by-generation/

[4] C. Systems. (2019) Global mobile data traffic from 2017 to 2022 (in exabytes per month). [Online]. Available: https://www.statista.com/statistics/271405/global-mobile-data-traffic-forecast

[5] S. Haykin, "Cognitive radio: brain-empowered wireless communications," *IEEE Journal on Selected Areas in Communications*, vol. 23, no. 2, pp. 201–220, Feb 2005.

[6] J. Mitola, "Cognitive radio for flexible mobile multimedia communications," in *1999 IEEE International Workshop on Mobile Multimedia Communications (MoMuC'99) (Cat. No.99EX384)*, Nov 1999, pp. 3–10.

[7] M. Xiao, S. Mumtaz, Y. Huang, L. Dai, Y. Li, M. Matthaiou, G. K. Karagiannidis, E. Björnson, K. Yang, C. I, and A. Ghosh, "Millimeter wave communication for future mobile networks," *IEEE J. on Sel. Areas in Commun.*, vol. 35, no. 9, pp. 1909–1935, Sept 2017.

[8] M. Shafi, A. F. Molisch, P. J. Smith, T. Haustein, P. Zhu, P. De Silva, F. Tufvesson, A. Benjebbour, and G. Wunder, "5G: A tutorial overview of standards, trials, challenges, deployment, and practice," *IEEE Journal on Selected Areas in Communications*, vol. 35, no. 6, pp. 1201–1221, June 2017.

[9] T. Schenk, *RF Imperfections in High-Rate Wireless Systems: Impact and Digital Compenstion*. Springer, The Netherlands, 2008.

[10] J. Zhang, L. Dai, X. Zhang, E. Björnson, and Z. Wang, "Achievable rate of rician large-scale MIMO channels with transceiver hardware impairments," *IEEE Trans. on Veh. Technol.*, vol. 65, no. 10, pp. 8800–8806, Oct 2016.

[11] M. Sadek, A. Tarighat, and A. H. Sayed, "A leakage-based precoding scheme for downlink multi-user MIMO channels," *IEEE Trans. on Wireless Commun.*, vol. 6, no. 5, pp. 1711–1721, May 2007.

[12] D. Zhang, Y. Wang, and W. Xiang, "Leakage-based hybrid beamforming design for downlink multiuser mmWave MIMO systems," in *2017 IEEE 28th Annual International Symposium on Personal, Indoor, and Mobile Radio Communications (PIMRC)*, Oct 2017, pp. 1–5.

[13] K.-C. Chen and R. Prasad, *Cognitive Radio Networks*. The Atrium, Southern Gate, Chichester, West Sussex,United Kingdom: John Wiley & Sons Ltd., 2009.

[14] S. K. Sharma, T. E. Bogale, S. Chatzinotas, B. Ottersten, L. B. Le, and X. Wang, "Cognitive radio techniques under practical imperfections: A survey," *IEEE Commun. Surveys Tuts.*, vol. 17, no. 4, pp. 1858–1884, Fourthquarter 2015.

[15] A. Khattab, D. Perkins, and M. Bayoumi, *Cognitive Radio Networks from theory to practice*. Springer, 2013.

[16] Huawei. (2020) World's first remote operation using 5G surgery.

[17] C. Rowell and A. Tankielun, "Plane wave converter for 5G massive MIMO basestation measurements," in *12th European Conference on Antennas and Propagation (EuCAP 2018)*, April 2018, pp. 1–3.

[18] J.Nsenga, W. V. Thillo, F. Horlin, A.Bourdoux, and R.Lauwereins, "Comparison of OQPSK and CPM for communications at 60 GHz with a nonideal front end," *EURASIP Journal on Wireless Commun. and Netw.*, vol. 2007, January 2007.

[19] E. G. Larsson, O. Edfors, F. Tufvesson, and T. L. Marzetta, "Massive MIMO for next generation wireless systems," *IEEE Communications Magazine*, vol. 52, no. 2, pp. 186–195, February 2014.

[20] U. Gustavsson, C. Sanchéz-Perez, T. Eriksson, F. Athley, G. Durisi, P. Landin, K. Hausmair, C. Fager, and L. Svensson, "On the impact of hardware impairments on massive MIMO," in *2014 IEEE Globecom Workshops (GC Wkshps)*, Dec 2014, pp. 294–300.

[21] E. Björnson, J. Hoydis, M. Kountouris, and M. Debbah, "Massive mimo systems with non-ideal hardware: Energy efficiency, estimation, and capacity limits," *IEEE Transactions on Information Theory*, vol. 60, no. 11, pp. 7112–7139, Nov 2014.

[22] E. Y. Imana, T. Yang, and J. H. Reed, "Suppressing the effects of aliasing and IQ imbalance on multiband spectrum sensing," *IEEE Transactions on Vehicular Technology*, vol. 66, no. 2, pp. 1074–1086, Feb 2017.

[23] A. Gokceoglu, Y. Zou, M. Valkama, and P. C. Sofotasios, "Multi-channel energy detection under phase noise: analysis and mitigation," *Mobile Networks and Applications*, vol. 19, no. 4, pp. 473–486, May 2014.

[24] O. Semiari, B. Maham, and C. Yuen, "On the effect of I/Q imbalance on energy detection and a novel four-level hypothesis spectrum sensing," *IEEE Trans. Veh. Technol.*, vol. 63, no. 8, pp. 4136–4141, Oct 2014.

[25] A. Fahim, *Radio frequency integrated circuit design for cognitive radio systems*. Springer International, 2016.

[26] M. B. Mabrouk, G. Ferré, E. Grivel, and N. Deltimple, "Interacting multiple model based detector to compensate power amplifier distortions in cognitive radio," *IEEE Transactions on Communications*, vol. 63, no. 5, pp. 1580–1593, May 2015.

[27] E. Biglieri, *Advanced sensing techniques for cognitive radio*. Cambridge: Cambridge University Press, 2012.

[28] C. Desset and L. Van der Perre, "Validation of low-accuracy quantization in massive MIMO and constellation EVM analysis," in *2015 European Conference on Networks and Communications (EuCNC)*, June 2015, pp. 21–25.

[29] S. Hao, Tongning Hu, and Qun Jane Gu, "Phase noise improvement for array systems," in *2016 IEEE MTT-S International Microwave Symposium (IMS)*, May 2016, pp. 1–4.

[30] Y. Bao, H. Lin, Y. Li, J. Li, Z. Wu, and Z. Li, "Phase noise estimation based on direct detection using phase noise to intensity noise conversion," in *2013 12th International Conference on Optical Communications and Networks (ICOCN)*, July 2013, pp. 1–3.

[31] T. Imaike, "Full digital phase noise measurement by using two reference oscillators and multichannel adcs," in *2017 Joint Conference of the European Frequency and Time Forum and IEEE International Frequency Control Symposium (EFTF/IFCS)*, July 2017, pp. 583–586.

[32] C. Studer, M. Wenk, and A. Burg, "MIMO transmission with residual transmit-RF impairments," in *2010 Int. ITG Workshop on Smart Antennas (WSA)*, Feb 2010, pp. 189–196.

[33] D. Dardari, V. Tralli, and A. Vaccari, "A theoretical characterization of nonlinear distortion effects in OFDM systems," *IEEE Transactions on Communications*, vol. 48, no. 10, pp. 1755–1764, Oct 2000.

[34] P. Zetterberg, "Experimental investigation of TDD reciprocity-based zero-forcing transmit precoding," *EURASIP Journal on Advances in Signal Processing*, vol. 2011, no. 1, dec 2010. [Online]. Available: https://doi.org/10.1155%2F2011%2F137541

[35] B. E. Priyanto, T. B. Sorensen, O. K. Jensen, T. Larsen, T. Kolding, and P. Mogensen, "Assessing and modeling the effect of RF impairments on UTRA LTE uplink performance," in *2007 IEEE 66th Veh. Technol. Conf.*, Sept 2007, pp. 1213–1217.

[36] G. Santella and F. Mazzenga, "A hybrid analytical-simulation procedure for performance evaluation in M-QAM-OFDM schemes in presence of nonlinear distortions," *IEEE Transactions on Vehicular Technology*, vol. 47, no. 1, pp. 142–151, Feb 1998.

[37] Hui Ye, Bin Li, Mo Huang, Zhen Liang, and Yan Lu, "A digital IQ imbalance self-calibration in FDD transceiver," in *2017 International Symposium on VLSI Design, Automation and Test (VLSI-DAT)*, April 2017, pp. 1–4.

[38] A. K. Gupta and J. F. Buckwalter, "Linearity considerations for Low-EVM, millimeter-wave direct-conversion modulators," *IEEE Transactions on Microwave Theory and Techniques*, vol. 60, no. 10, pp. 3272–3285, Oct 2012.

[39] B. Jiang, R. Ye, Y. Huang, S. He, M. Su, and H. Wang, "Comparison of single carrier and OFDM on 45GHz millimeter-wave communication system with hardware impairments," in *2016 19th Int. Symp. on Wireless Pers. Multimedia Commun. (WPMC)*, Nov 2016, pp. 423–428.

[40] P. K. Sharma and P. K.Upadhyay, "Cognitive relaying with transceiver hardware impairments under interference constraints," *IEEE Commun. Lett.*, vol. 20, no. 1, pp. 820–823, April 2016.

[41] S. Solanki, P. K. Upadhyay, D. B. da Costa, P. S. Bithas, and A. G. Kanatas, "Performance analysis of cognitive relay networks with RF hardware impairments and CEEs in the presence of primary users' interference," *IEEE Trans. on Cognitive Commun. and Networking*, vol. 4, no. 2, pp. 406–421, June 2018.

[42] A. A. A. Boulogeorgos, N. D. Chatzidiamantis, and G. K. Karagiannidis, "Energy detection spectrum sensing under RF imperfections," *IEEE Trans. Commun.*, vol. 64, no. 7, pp. 2754–2766, July 2016.

[43] J. Zhang, Y. Wei, E. Björnson, Y. Han, and S. Jin, "Performance analysis and power control of cell-free massive MIMO systems with hardware impairments," *IEEE Access*, vol. 6, pp. 55 302–55 314, 2018.

[44] L. Tlebaldiyeva and T. Tsiftsis, "Underlay cognitive radio with imperfect transceiver electronics under nakagami-m fading," in *2018 International Conference on Computing and Network Communications (CoCoNet)*, Aug 2018, pp. 58–63.

[45] Hung-yu Wei and R. D. Gitlin, "WWAN/WLAN two-hop-relay architecture for capacity enhancement," in *2004 IEEE Wireless Communications and Networking Conference (IEEE Cat. No.04TH8733)*, vol. 1, March 2004, pp. 225–230 Vol.1.

[46] E. Bjornson, M. Matthaiou, and M. Debbah, "A new look at dual-hop relaying: Performance limits with hardware impairments," *IEEE Trans. Commun.*, vol. 61, no. 11, pp. 4512–4525, November 2013.

[47] D. K. Nguyen, T. T. Lam, and H. Ochi, "Performance analysis: DF cognitive network with transceiver imperfections," in *2014 48th Asilomar Conf. on Signals, Syst. and Comput.*, 2014, pp. 1604–1608.

[48] D. K. Nguyen and H. Ochi, "Transceiver impairments in DF/AF dual-hop cognitive relay networks: Outage performance and throughput analysis," in *2015 IEEE 81st Veh. Technol. Conf.*, Glasgow, UK, May 2015, pp. 1–5.

[49] A. K. Mishra, D. Mallick, and P. Singh, "Combined effect of RF impairment and CEE on the performance of dual-hop fixed-gain af relaying," *IEEE Commun. Lett.*, vol. 20, no. 9, pp. 1725–1728, Sept 2016.

[50] H. Huang, Z. Li, B. Ai, G. Wang, and M. S. Obaidat, "Impact of hardware impairment on spectrum underlay cognitive multiple relays network," in *2016 IEEE Int. Conf. Commun. (ICC)*, May 2016, pp. 1–6.

[51] C. Zhong, T. Ratnarajah, and K. K. Wong, "Outage analysis of decode-and-forward cognitive dual-hop systems with the interference constraint in Nakagami- m fading channels," *IEEE Trans. on Veh. Technol.*, vol. 60, no. 6, pp. 2875–2879, July 2011.

[52] A. Papoulis and U. Pillai, *Probability, Random Variables and Stochastic Processes*, 4th ed. McGraw-Hill Europe, 2002.

[53] National Instruments. Introduction to lte device testing from theory to transmitter and receiver measurements. Accessed April 1, 2017. [Online]. Available: http://download.ni.com/evaluation/rf/IntroductiontoLTEDeviceTesting.pdf

[54] L. Tlebaldiyeva, T. A. Tsiftsis, and B. Maham, "Performance analysis of improved energy detector with hardware impairments for accurate spectrum sensing," *IEEE Access*, vol. 7, pp. 13 927–13 938, 2019.

[55] F. F. Digham, M. S. Alouini, and M. K. Simon, "On the energy detection of unknown signals over fading channels," *IEEE Trans. Commun.*, vol. 55, no. 1, pp. 21–24, Jan 2007.

[56] Y. Chen, "Improved energy detector for random signals in gaussian noise," *IEEE Trans. Wireless Commun.*, vol. 9, no. 2, pp. 558–563, February 2010.

[57] A. Singh, M. R. Bhatnagar, and R. K. Mallik, "Performance of an improved energy detector in multihop cognitive radio networks," *IEEE Trans. Veh. Technol.*, vol. 65, no. 2, pp. 732–743, Feb 2016.

[58] L. Gahane, P. K. Sharma, N. Varshney, T. A. Tsiftsis, and P. Kumar, "An improved energy detector for mobile cognitive users over generalized fading channels," *IEEE Trans. Commun.*, vol. PP, no. 99, pp. 1–1, 2017.

[59] S. Nallagonda, S. D. Roy, S. Kundu, G. Ferrari, and R. Raheli, "Censoring-based cooperative spectrum sensing with improved energy detectors and multiple antennas in fading channels," *IEEE Trans. Aerosp. and Electron. Syst.*, vol. PP, no. 99, pp. 1–1, 2018.

[60] L. Gahane and P. K. Sharma, "Performance of improved energy detector with cognitive radio mobility and imperfect channel state information," *IET Commun.*, vol. 11, no. 12, pp. 1857–1863, 2017.

[61] M. Ranjeeth, S. Behera, S. Nallagonda, and S. Anuradha, "Optimization of cooperative spectrum sensing based on improved energy detector with selection diversity in awgn and rayleigh fading," in *2016 Int. Conf. on Elect., Electron., and Optimization Techn.(ICEEOT)*, March 2016, pp. 2402–2406.

[62] L. Safatly, A. El-Hajj, and K. Y. Kabalan, "Blind and robust spectrum sensing based on RF impairments mitigation for cognitive radio receivers," in *2014 Int. Conf. on High Performance Computing Simulation (HPCS)*, July 2014, pp. 820–824.

[63] A. Gokceoglu, S. Dikmese, M. Valkama, and M. Renfors, "Energy detection under IQ imbalance with single- and multi-channel direct-conversion receiver: Analysis and mitigation," *IEEE J. on Select. Areas in Commun.*, vol. 32, no. 3, pp. 411–424, March 2014.

[64] A. A. Boulogeorgos, H. A. B. Salameh, and G. K. Karagiannidis, "Spectrum sensing in full-duplex cognitive radio networks under hardware imperfections," *IEEE Trans. on Veh. Technol.*, vol. 66, no. 3, pp. 2072–2084, March 2017.

[65] H. Rinne, *The Weibull Distribution: A Handbook*, 1st ed. Chapman and Hall/CRC, 2008.

[66] J. C. S. S. Filho and M. D. Yacoub, "Simple precise approximations to weibull sums," *IEEE Commun. Lett.*, vol. 10, no. 8, pp. 614–616, Aug 2006.

[67] M. D. Yacoub, "The $\alpha - \mu$ distribution: A physical fading model for the stacy distribution," *IEEE Trans. Veh. Technol.*, vol. 56, no. 1, pp. 27–34, Jan 2007.

[68] I. S. Gradshteyn and I. M. Ryzhik, *Table of integrals, series, and products*, 7th ed. Elsevier/Academic Press, Amsterdam, 2007.

[69] S. Atapattu, C. Tellambura, and H. Jiang, "Analysis of area under the ROC curve of energy detection," *IEEE Trans. Wireless Commun.*, vol. 9, no. 3, pp. 1216–1225, March 2010.

[70] ——, *Energy Detection for Spectrum Sensing in Cognitive Radio*. Springer Publishing Company, Incorporated, 2014.

[71] S. Shanmugave and M. A. Bhagyaveni, *Cognitive Radio - An Enabler for Internet of Things*. River Publishers, 2017.

[72] L. Tlebaldiyeva, B. Maham, and T. A. Tsiftsis, "Device-to-device mmWave communication in the presence of interference and hardware distortion noises," *IEEE Communications Letters*, vol. 23, no. 9, pp. 1607–1610, Sep. 2019.

[73] ——, "Capacity analysis of device-to-device mmWave networks under transceiver distortion noise and imperfect CSI," *IEEE Transactions on Vehicular Technology*, pp. 1–1, 2020.

[74] C. Systems. (2019) Cisco visual networking index: Global mobile data traffic forecast update, 2017–2022 white paper. [Online]. Available: https://www.cisco.com/c/en/us/solutions/collateral/service-provider/visual-networking-index-vni/white-paper-c11-738429.html

[75] R. I. Ansari, C. Chrysostomou, S. A. Hassan, M. Guizani, S. Mumtaz, J. Rodriguez, and J. J. P. C. Rodrigues, "5G D2D networks: Techniques, challenges, and future prospects," *IEEE Systems J.*, vol. 12, no. 4, pp. 3970–3984, Dec 2018.

[76] E. A. Maher, W. Alexan, and A. El-Mahdy, "Interference management for D2D communications underlay macro-small cell networks with imperfect channel estimation," in *2017 Advances in Wireless and Optical Commun. (RTUWO)*, Nov 2017, pp. 256–261.

[77] G. Nauryzbayev, S. Arzykulov, E. Alsusa, and T. A. Tsiftsis, "An alignment-based interference cancellation scheme for network-MIMO systems," in *2016 10th International Conference on Signal Processing and Communication Systems (ICSPCS)*, 2016, pp. 1–5.

[78] ——, "A closed-form solution to implement interference alignment and cancellation scheme for the MIMO three-user x-channel model," in *2016 10th International Conference on Signal Processing and Communication Systems (ICSPCS)*, 2016, pp. 1–6.

[79] Y. Yang, Y. Zhang, L. Dai, J. Li, S. Mumtaz, and J. Rodriguez, "Transmission capacity analysis of relay-assisted device-to-device overlay/underlay communication," *IEEE Transactions on Industrial Informatics*, vol. 13, no. 1, pp. 380–389, Feb 2017.

[80] Y. Ni, Y. Wang, and H. Zhu, "Interference cancellation in device-to-device communications underlying MU-MIMO cellular networks," *China Communications*, vol. 16, no. 4, pp. 75–88, April 2019.

[81] T. Bai and R. W. Heath, "Coverage and rate analysis for millimeter-wave cellular networks," *IEEE Trans. on Wireless Commun.*, vol. 14, no. 2, pp. 1100–1114, Feb 2015.

[82] S. Kusaladharma, Z. Zhang, and C. Tellambura, "Interference and outage analysis of random D2D networks underlaying millimeter-wave cellular networks," *IEEE Trans. on Commun.*, vol. 67, no. 1, pp. 778–790, Jan 2019.

[83] Y. J. Chun, S. L. Cotton, H. S. Dhillon, A. Ghrayeb, and M. O. Hasna, "A stochastic geometric analysis of device-to-device communications operating over generalized fading channels," *IEEE Trans. on Wireless Commun.*, vol. 16, no. 7, pp. 4151–4165, July 2017.

[84] S. N. Islam, M. A. Mahmud, and A. M. T. Oo, "Achievable sum rate analysis of relay aided overlay device to device communication among multiple devices," *J. of Commun. and Netw.*, vol. 19, no. 4, pp. 309–318, August 2017.

[85] K. Venugopal, M. C. Valenti, and R. W. Heath, "Device-to-device millimeter wave communications: Interference, coverage, rate, and finite topologies," *IEEE Trans. on Wireless Commun.*, vol. 15, no. 9, pp. 6175–6188, Sept 2016.

[86] M. K. Simon and M. S. Alouini, *Digital Communications over Fading Channels*, 2nd ed. John Wiley I& Sons, 2005.

[87] A. Memmi, Z. Rezki, and M. Alouini, "Power control for D2D underlay cellular networks with channel uncertainty," *IEEE Trans. on Wireless Commun.*, vol. 16, no. 2, pp. 1330–1343, Feb 2017.

[88] P. G. Moschopoulos, "The distribution of the sum of independent gamma random variables," *Annals of the Institute of Statistical Mathematics*, vol. 37, no. 3, pp. 541–544, 1985.

[89] H. Murakami, "Approximations to the distribution of sum of independent non-identically gamma random variables," *Mathematical Sciences*, vol. 9, no. 4, pp. 205–213, Dec 2015. [Online]. Available: https://doi.org/10.1007/s40096-015-0169-2

[90] A. Laforgia and P. Natalini, "On the asymptotic expansion of a ratio of gamma functions," *Journal of Mathematical Analysis and Applications*, vol. 389, no. 2, pp. 833 – 837, 2012. [Online]. Available: http://www.sciencedirect.com/science/article/pii/S0022247X11011280

[91] L. Tlebaldiyeva, B. Maham, and O.Tirkkonen, "Maximum sub-array diversity for mmWave network under RF power leakage and transceiver distortion noises," in *2020 IEEE Wireless Communications and Networking Conference (WCNC)*, Accepted 2020.

[92] D. Kim and S. Park, "Digital beamforming technique with high resolution digital phase shifter and digital phase calibration using SDR," in *2017 International Symposium on Antennas and Propagation (ISAP)*, Oct 2017, pp. 1–2.

[93] B. Yang, Z. Yu, J. Lan, R. Zhang, J. Zhou, and W. Hong, "Digital beamforming-based massive MIMO transceiver for 5G millimeter-wave communications," *IEEE Transactions on Microwave Theory and Techniques*, vol. 66, no. 7, pp. 3403–3418, July 2018.

[94] I. Ahmed, H. Khammari, A. Shahid, A. Musa, K. S. Kim, E. De Poorter, and I. Moerman, "A survey on hybrid beamforming techniques in 5G: Architecture and system model perspectives," *IEEE Communications Surveys Tutorials*, vol. 20, no. 4, pp. 3060–3097, Fourthquarter 2018.

[95] S. Kutty and D. Sen, "Beamforming for millimeter wave communications: An inclusive survey," *IEEE Communications Surveys Tutorials*, vol. 18, no. 2, pp. 949–973, Secondquarter 2016.

[96] A. F. Molisch, V. V. Ratnam, S. Han, Z. Li, S. L. H. Nguyen, L. Li, and K. Haneda, "Hybrid beamforming for massive MIMO: A survey," *IEEE Communications Magazine*, vol. 55, no. 9, pp. 134–141, Sep. 2017.

[97] K. Satyanarayana, M. El-Hajjar, P. Kuo, A. Mourad, and L. Hanzo, "Dual-function hybrid beamforming and transmit diversity aided millimeter wave architecture," *IEEE Trans. on Veh. Technol.*, vol. 67, no. 3, pp. 2798–2803, March 2018.

[98] J. Zhang, X. Xue, E. Björnson, B. Ai, and S. Jin, "Spectral efficiency of multipair massive MIMO two-way relaying with hardware impairments," *IEEE Wireless Commun. Lett.*, vol. 7, no. 1, pp. 14–17, Feb 2018.

[99] X. Tian, Q. Liu, Z. Wang, and M. Li, "Secure hybrid beamformers design in mmwave MIMO wiretap systems," *IEEE Systems Journal*, vol. 14, no. 1, pp. 548–559, 2020.

[100] S. Jacobsson, U. Gustavsson, G. Durisi, and C. Studer, "Massive mu-mimo-ofdm uplink with hardware impairments: Modeling and analysis," in *2018 52nd Asilomar Conference on Signals, Systems, and Computers*, 2018, pp. 1829–1835.

[101] H. Chung, Y. M. Park, and S. Kim, "A sidelobe suppression technique for millimeter wave beamforming," in *2018 24th Asia-Pacific Conference on Communications (APCC)*, Nov 2018, pp. 592–597.

[102] M. Li, Z. Wang, H. Li, Q. Liu, and L. Zhou, "A hardware-efficient hybrid beamforming solution for mmwave MIMO systems," *IEEE Wireless Communications*, vol. 26, no. 1, pp. 137–143, 2019.

[103] R. Méndez-Rial, C. Rusu, N. González-Prelcic, A. Alkhateeb, and R. W. Heath, "Hybrid MIMO architectures for millimeter wave communications: Phase shifters or switches?" *IEEE Access*, vol. 4, pp. 247–267, 2016.

[104] A. P. Prudnikov, Y. A. Brychkov, and O. I. Marichev, *Integrals and series*. New York, NY, USA: CRC, 1986.